

An Experimental Approach on Beating in Vibration Due to Rotational Unbalance

Dragos-Florin Chitariu *, Florin Negoescu, Mihaita Horodincu, Catalin-Gabriel Dumitras, Gures Dogan and Mehmet Ilhan

“Gheorghe Asachi” Technical University of Iasi, 700050 Iasi, Romania;
florin.negoescu@academic.tuiasi.ro (F.N.); mihaita.horodincu@academic.tuiasi.ro (M.H.);
catalin-gabriel.dumitras@academic.tuiasi.ro (C.-G.D.); gures.dogan@student.tuiasi.ro (G.D.);
ilhan.mehmet@student.tuiasi.ro (M.I.)

* Correspondence: dragos.chitariu@tuiasi.ro; Tel.: +40-741-269-491

Received: 2 September 2020; Accepted: 28 September 2020; Published: 1 October 2020

Abstract: This paper proposes a study in theoretical and experimental terms focused on the vibration beating phenomenon produced in particular circumstances: the addition of vibrations generated by two rotating unbalanced shafts placed inside a lathe headstock, with a flat friction belt transmission between the shafts. The study was done on a simple computer-assisted experimental setup for absolute vibration velocity signal acquisition, signal processing and simulation. The input signal is generated by a horizontal geophone as the sensor, placed on a headstock. By numerical integration (using an original antiderivative calculus and signal correction method) a vibration velocity signal was converted into a vibration displacement signal. In this way, an absolute velocity vibration sensor was transformed into an absolute displacement vibration sensor. An important accomplishment in the evolution of the resultant vibration frequency (or combination frequency as well) of the beating vibration displacement signal was revealed by numerical simulation, which was fully confirmed by experiments. In opposition to some previously reported research results, it was discovered that the combination frequency is slightly variable (tens of millihertz variation over the full frequency range) and it has a periodic pattern. This pattern has negative or positive peaks (depending on the relationship of amplitudes and frequencies of vibrations involved in the beating) placed systematically in the nodes of the beating phenomena. Some other achievements on issues involved in the beating phenomenon description were also accomplished. A study on a simulated signal proves the high theoretical accuracy of the method used for combination frequency measurement, with less than 3 microhertz full frequency range error. Furthermore, a study on the experimental determination of the dynamic amplification factor of the combination vibration (5.824) due to the resonant behaviour of the headstock and lathe on its foundation was performed, based on computer-aided analysis (curve fitting) of the free damped response. These achievements ensure a better approach on vibration beating phenomenon and dynamic balancing conditions and requirements.

Keywords: lathe headstock; rotational unbalance; vibration; beating; signal processing

1. Introduction

Rotating unbalance is a topic frequently mentioned in the analysis of the dynamics of rotary bodies (rotordynamics [1]). The rotating unbalance occurs due to an asymmetry of mass distribution (in some different regions of the rotary body, the center of mass is not placed on the axis of rotation). Centrifugal forces occur in these unbalanced regions of the rotary body. The resultant of these centrifugal forces is transmitted through the bearings to the structure where the rotary body is placed.

In each bearing the resultant of centrifugal forces has two components at orthogonal directions. Each component acts as a harmonic excitation force against the structure, thus generating vibrations.

For some specific appliances these vibrations are desirable (e.g. in vibration shakers used also as mechanical vibration exciters [2,3], vibration alert systems in mobile phones, electronic vibrating bracelets [4], and haptic feedback devices with vibrations [5]). Generally, the vibrations due to the rotating body unbalances have highly undesirable effects (e.g., bad surface quality in the grinding process [6,7], premature bearing destruction [8,9]), and human body discomfort [10]). In order to measure [11] and to eliminate the unbalance of rotary bodies [12–14] (using additional balancing masses and additional inertia [15]), several special requirements must be met and specialized equipment must be used [16,17]. Actually, one of the best ways to balance rotary unbalanced bodies is through the use of self-balancing systems [18,19].

Sometimes two rotary unbalanced bodies having almost the same angular speed (or rotational frequency) which rotate in the same structure (e.g., in centerless grinding machines, [20]) produce a vibration beating phenomenon [10,21,22].

Each rotary unbalanced body generates a vibration. The addition of two vibrations, having slightly different frequencies, produces the aforementioned beating phenomenon. This is a resultant vibration with periodical variation of amplitude, with nodes (where the amplitude has a minimum value, the addition of the two vibrations produces destructive interference, 180 degrees out of phase between the constituents of the resultant vibration) and anti-nodes (a maximum amplitude, where the addition of the two vibrations produces constructive interference, with zero degrees shift of phase between constituents) [23]. Obviously the beating phenomenon in mechanics is not solely related to the vibrations produced by rotary unbalanced bodies, it also occurs when two vibration modes with almost the same modal frequency are excited [24,25], and it occurs as well when a system vibrates simultaneously due to forced sinusoidal excitation close to a resonant frequency and due to a free response [26–29].

Some specific appliances use the vibration beating phenomenon to monitor the condition of mechanical systems, e.g., monitoring the adhesion integrity of single lap joints [30], monitoring the structural integrity of helicopter rotor blades [31], and for seismic vibration testing [32]. A vibration beating mechanism in piezoelectric energy harvesting systems is proposed in [33].

In machine tools, in addition to a critical source of vibrations (self-excited vibrations in turning [34], milling [35] or grinding [36] processes), the vibrations produced by rotary unbalance (generated by tools [37], shafts [38] or work pieces [36]) and particularly the beating phenomenon [6] created by rotary unbalanced bodies, are important items. This paper proposes some approaches, in theoretical and experimental terms, to address the vibration beating phenomenon produced inside a Romanian lathe headstock SNA 360, by two inner unbalanced rotary shafts, rotating with very close angular speeds. The main achievements of this paper are producing results in the areas of: vibration beating monitoring, conversion of a velocity vibration signal into a displacement signal (by antiderivative calculus), and the evolution of beating vibration signal frequency (pattern, simulation, measurement and accuracy measurement), as well as producing a study of the influence of headstock and lathe foundation dynamics on vibration amplitudes.

2. A Theoretical Approach

Assume that the rotary unbalance of each shaft (each of which rotates at angular speeds of ω_1 and ω_2 , respectively) is reducible at the asymmetry of mass distribution with unbalance masses m_1 and m_2 , respectively, placed in a single plane at distances r_1 and r_2 , respectively, to the rotation axis. The horizontal projection of the centrifugal forces of each rotary unbalance ($F_1 = m_1\omega_1^2r_1$ and $F_2 = m_2\omega_2^2r_2$) generates vibration displacements $y_1 = kD_{af1}F_1\cos(\theta_1)$ and $y_2 = kD_{af2}F_2\cos(\theta_2)$, where k is the stiffness of the headstock and the lathe foundation, D_{af1} and D_{af2} are the dynamic amplification factors and $\theta_1 = \omega_1t + \varphi_1$ and $\theta_2 = \omega_2t + \varphi_2$ are the instantaneous values of the angle of the centrifugal forces with respect to the horizontal direction (φ_1 and φ_2 being the instantaneous values of these angles at $t = 0$). With these considerations, a complete description of y_1 and y_2 of the vibrations is given below:

$$y_1 = kD_{af1}m_1\omega_1^2r_1\cos(\omega_1t + \varphi_1) = A_1\cos(\omega_1t + \varphi_1) \quad (1)$$

$$y_2 = kD_{af2}m_2\omega_2^2r_2\cos(\omega_2t + \varphi_2) = A_2\cos(\omega_2t + \varphi_2) \quad (2)$$

Here $A_1 = kD_{af1}m_1\omega_1^2r_1$ and $A_2 = kD_{af2}m_2\omega_2^2r_2$ are the vibration amplitudes of the two shafts, respectively. The headstock and the lathe vibrate as a single body on its foundation (as a mass–spring–damper system) with a vibratory motion which is the result of the addition $y_1 + y_2$ of these two vibrations, a periodical non-harmonic motion that presents itself as a beating phenomenon [23], with nodes and anti-nodes (as the simulation from Figure 1 proves). According to Figure 1, if the period of vibration y_1 is $T_1 = 2\pi/\omega_1$ and $T_2 = 2\pi/\omega_2$ is the period of vibration y_2 , then the period T_b of the beating phenomenon (the beat period being the time between two anti-nodes or between two nodes, as well) and the periods T_1, T_2 (with $T_2 < T_1$) should fulfill this obvious condition:

$$T_b = nT_1 = (n + 1)T_2 \quad (3)$$

with n being a natural number, defined from Equation (3) as:

$$n = T_2/(T_1 - T_2) \quad (4)$$

In Figure 1 $n = 7$. If in Equations (3) and (4) the periods are replaced by frequencies ($T_b = 1/f_b$, $T_1 = 1/f_1$, $T_2 = 1/f_2$), then the resulting frequency f_b of the beating phenomenon (beat frequency or the number of nodes per second, as well) is:

$$f_b = f_2 - f_1 \quad (5)$$

In Figure 1 $f_2 = 8$ Hz and $f_1 = 7$ Hz; these generate $f_b = 1$ Hz with $T_b = 1$ s ($A_1 = 10$, $A_2 = 8$, $\varphi_1 = 0$, $\varphi_2 = -\pi/2$).

According to [39], the resultant waveform of the vibration addition $y_1 + y_2$ has the frequency $f_c = 1/T_c$ (as a combination frequency or modulation frequency, with the period T_c highlighted on Figure 1) defined as:

$$f_c = (f_1 + f_2)/2 \quad (6)$$

This paper will prove by simulations and experiments that this definition is not accurate, especially when $A_1 \neq A_2$.

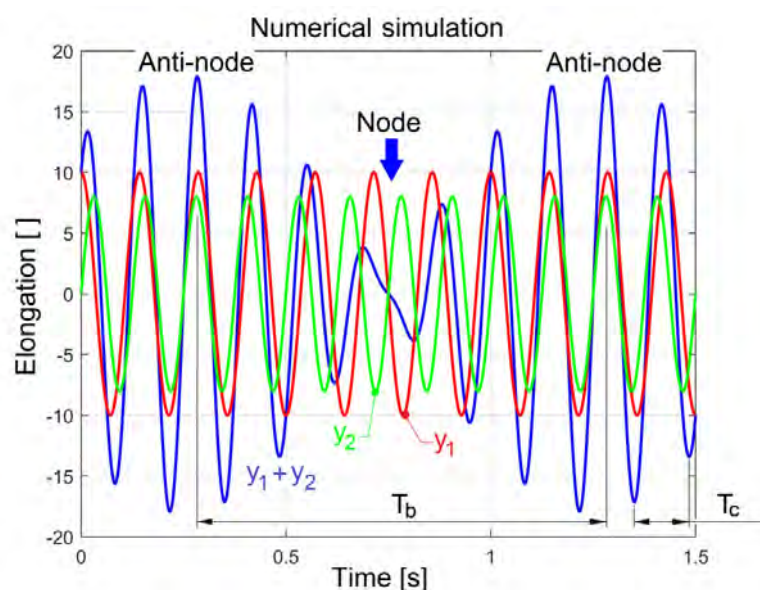


Figure 1. A simulation of the beating phenomenon, where: y_1 is the vibration of shaft 1; y_2 is the vibration of shaft 2, T_b is the beat period; and T_c is the period of the resultant vibration $y_1 + y_2$.

These theoretical considerations and some other supplementary issues and procedures will be confirmed by experimental approach in this paper.

3. Experimental Setup

Figure 2a presents a lateral view of both shafts (1 and 2, placed in the headstock) involved in the beating phenomenon due to rotary unbalance.

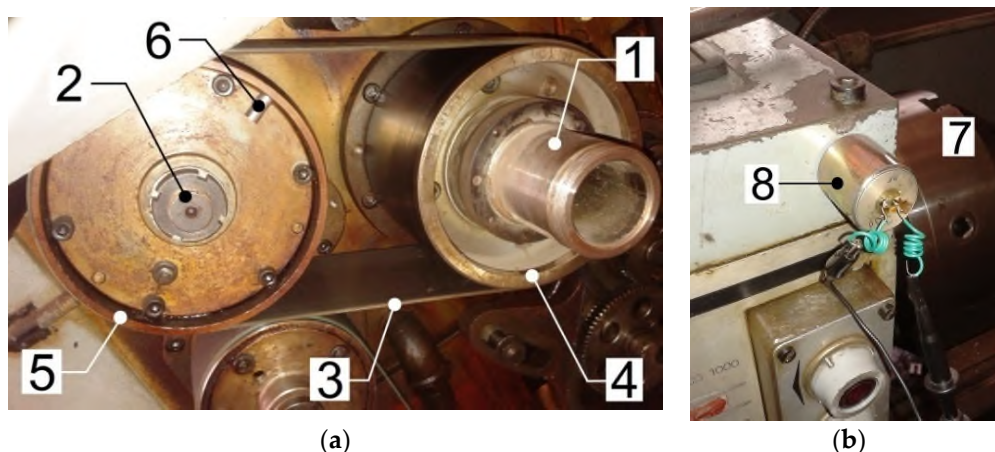


Figure 2. (a) A lateral view of the shafts involved in the beating phenomenon (with a flat belt transmission between the shafts); (b) A front view of the lathe headstock with the vibration sensor.

A friction belt transmission with a flat drive belt 3, a pulley 4 (on shaft 1) and a pulley 5 (on shaft 2) synchronously rotates both shafts (the theoretical value of transmission speed ratio is 1:1). Here 6 depicts an additional mass (10.8 g, a permanent magnet) placed in different angular positions on pulley 5 and used to change the internal unbalancing of the shaft 2.

The shaft 1 is also the lathe main spindle (with the jaw chuck labelled with 7 on Figure 2b placed on the opposite side of Figure 2a). Figure 2b shows an absolute velocity vibration sensor 8 (an electrodynamic seismic geophone Geo Space GS 11D, now HGS Products HG4 as described in [40]), placed on the headstock. The geophone corner frequency (8 Hz) is smaller than the minimum frequency of the headstock vibration (17 Hz). No significant resonant amplification at the corner

frequency can be identified (the open circuit damping being 34% of critical damping). The geophone sensitivity is 31.89 V/m/s.

The signal delivered by the vibration sensor (a voltage proportional to the vibration velocity of the headstock) is numerically acquired by a personal computer via a computer-assisted numerical oscilloscope PicoScope 4424 from Pico Technology, Saint Neots, UK (USB powered, four channels, 12 bits resolution, 80 MS/s maximum sampling, 32 MS memory) [41]. Due to the high sensitivity of the geophone and oscilloscope features (e.g., a numerically controlled internal amplifier) the supplementary amplification of the signal delivered by vibration sensor is not necessary.

The computer-aided processing of this signal was done in Matlab. Firstly, the signal delivered by sensor must be mathematically divided by the sensitivity of the sensor in order to obtain the vibration velocity evolution. Secondly, the velocity of vibration must be numerically integrated (by antiderivative calculus) in order to obtain the vibration displacement evolution. The description and analysis of the evolution of some of the other vibration features (e.g., the combination frequency f_c , the beat vibration amplitude and the free vibrations of the lathe on foundation) were also performed.

In order to measure the average value of the instantaneous angular speed (IAS) ω_1 of the main spindle (shaft 1) rigorously, the technique described in our previous work [42] was used (with a two phase multi-pole AC generator placed in the jaw chuck, as an IAS sensor). The same technique (which refers only to signal processing, briefly described later on) was used for an accurate measurement of the combination frequency f_c .

4. Experimental Results and Discussion

4.1. A Beating Phenomenon Described in Vibration Velocity

Figure 3 presents the evolution of the headstock vibration velocity during a time interval of 200 s, described with 1 MS (or 1,000,000 samples as well) so a sampling interval of $\Delta t = 200 \mu\text{s}$, when the main spindle (shaft 1) rotates (and shaft 2, as well) in the steady-state regime, with constant IAS, with an average value of $\omega_1 = 109.2369 \text{ rad/s}$ (for $f_1 = 17.3856 \text{ Hz}$ average rotation frequency, or 1,043.1 revolutions per minute on average).

It is obvious that Figure 3 depicts a vibration beating phenomenon with nodes and anti-nodes, with a very high value of the period T_b (96.6 s) and consequently with a very small value of beat frequency $f_b = 1/T_b = 1/96.6 \text{ Hz}$. The beating phenomenon proves that the IASs ω_1 and ω_2 and also rotation frequencies f_1 and f_2 as well, are slightly different because the diameters of pulleys 4 and 5 involved in belt transmission are not strictly the same. With $T_1 = 1/f_1$ and the relationship between T_1 and T_b from Equation (3) there are $n \approx T_b \cdot f_1 \approx 1679$ periods T_1 between nodes (and between anti-nodes as well). This is an approximated value of n because the frequency f_1 is not rigorously constant (as is proved, later in this paper). According to Equation (3), at each n complete rotations of shaft 1, the shaft 2 makes $n + 1$ or $n - 1$ rotations (one rotation difference), which means that the experimentally revealed value of the belt transmission speed ratio is $\omega_2/\omega_1 = T_1/T_2 = n/(n \pm 1) \approx 1679/(1679 \pm 1)$. This is also the ratio between pulleys diameters: the diameter of pulley 4 divided by the diameter of pulley 5 (assuming that there is no slipping between the belt and the pulleys).

The additional mass 6 (Figure 2a) was placed in a certain angular position on pulley 5, in order to obtain a maximum value of the amplitude A_2 , and a maximum difference between amplitudes in anti-nodes and nodes as well. It is obvious that the main spindle (shaft 1) is also unbalanced; otherwise the beating phenomenon does not occur.

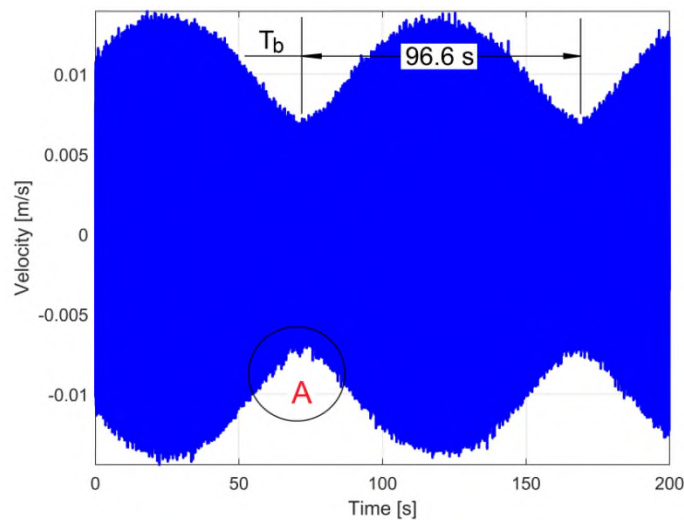


Figure 3. The evolution of the velocity of headstock vibrations with a beating phenomenon due to rotary unbalanced shafts; here T_b is the beat period, A is a label for a future comment on signal evolution.

Figure 4 presents a zoomed-in detail in the area labelled A in Figure 3. Here the dominant component (≈ 6 mm/s amplitude) is the sum of two vibrations created by rotary unbalances; the other low amplitude (and high frequency) components are related by vibrations generated by some other headstock rotary components.

With the values for f_1 and f_b revealed before, the frequency f_2 is a result of Equation (5), with two possible values ($f_2 = f_1 - f_b = 17.3752$ Hz or $f_2 = f_1 + f_b = 17.3959$ Hz). Because in Equation (5) the notations f_1 and f_2 are arbitrary, this equation should be reconsidered as $f_b = |f_2 - f_1|$.

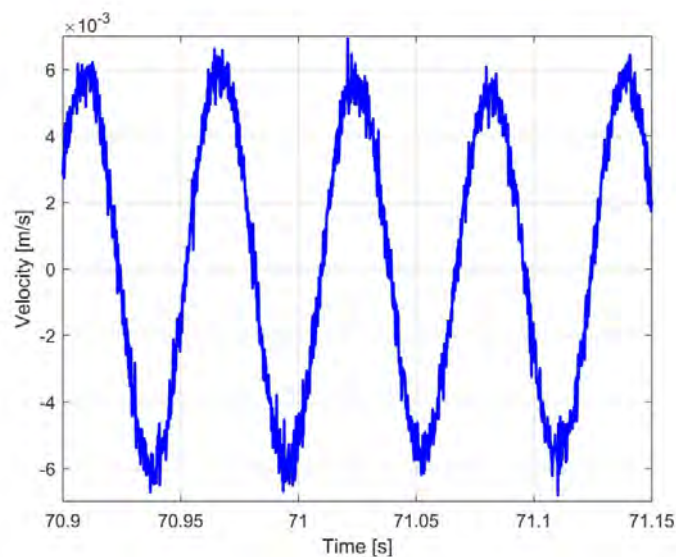


Figure 4. A zoomed-in detail of Figure 3 in the area labelled as A.

As a consequence, the angular speed $\omega_2 = 2\pi f_2$ has two possible values ($\omega_2 = 109.1716$ rad/s or $\omega_2 = 109.3016$ rad/s), as does the speed ratio (ω_2/ω_1) of the driving belt (with $\omega_1 = 109.2369$ rad/s). To find the right value of f_2 (and ω_2 as well) the technique described in [42] should be used (with an IAS sensor placed on shaft 2).

The evolution from Figure 3 is an addition of vibrations velocities ($v = dy_1/dt + dy_2/dt$) generated by both of the unbalanced shafts (1 and 2). It is expected that the beating phenomenon keeps the main characteristics (e.g., T_b , T_c values or f_b , f_c values, as well) if it is described using the addition of vibration

displacements ($s = y_1 + y_2$), except for the amplitudes in nodes and anti-nodes which significantly decreases.

4.2. The Description of the Beating Phenomenon in Vibration Displacement by Numerical Integration

The vibration displacement evolution can be obtained from vibration velocity evolution by numerical integration (antiderivative calculus). Based on the approximate definition of velocity (derivative of displacement) $v = ds/dt \approx \Delta s/\Delta t$, a current sample of velocity v_i is defined using two successive samples of displacement s_i, s_{i-1} (in the displacement interval $\Delta s = s_i - s_{i-1}$) and the values of time t_i, t_{i-1} for these samples, in the sampling interval $\Delta t = t_i - t_{i-1}$ (usually this is a constant value) as:

$$v_i = \frac{s_i - s_{i-1}}{\Delta t} \quad (7)$$

This is an approximation of the first derivative of displacement as backward finite difference, with $i > 1$ [43]. The current sample of displacement s_i can be simply mathematically extracted from Equation (7) as:

$$s_i = v_i \Delta t + s_{i-1} \quad (8)$$

Equation (8) describes a sample s_i of displacement related to velocity, this also being our proposal for a description of numerical integration of velocity (antiderivative calculus). According to Equation (8) the sample s_i depends on sampling interval Δt (here Δt is the time $t_i - t_{i-1}$ between two consecutive samples of velocity v_i and v_{i-1} or two consecutive samples of displacement s_i and s_{i-1} as well), the velocity sample v_i and the previous sample of displacement s_{i-1} , as the result of a previous step of numerical integration. The numerical integration from Equation (8) is available for $i > 1$. Of course, it is mandatory to know the value of the first sample of displacement s_1 , this being an indefinite value because $i > 1$. This is exactly the constant C of integration (usually an arbitrary value). Pure harmonic signals are numerically integrated, in that case, evidently $C = 0$.

Figure 5a describes the graphical result of numerical integration of vibration elongation evolution from Figure 3 using Equation (8), with $C = s_1 = 0$. Certainly this evolution is not strictly related to the vibration displacement from the beating phenomenon.

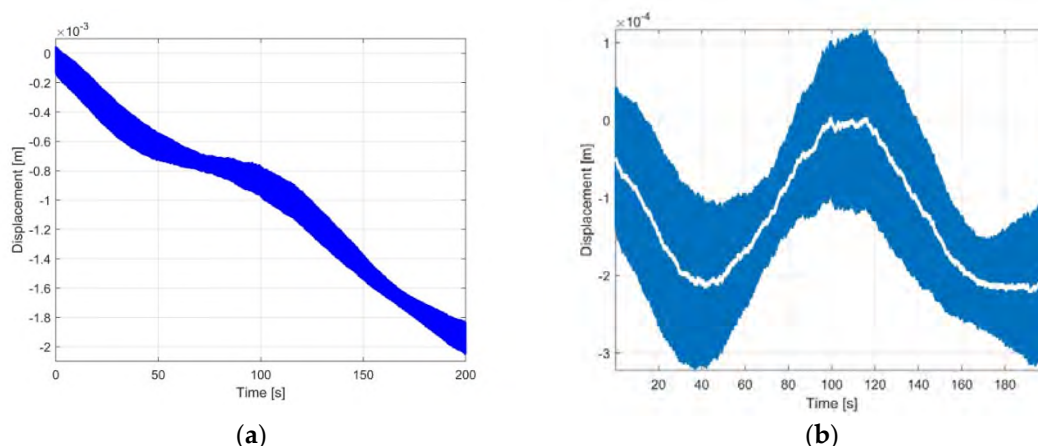


Figure 5. (a) The result of numerical integration of velocity evolution from Figure 3; and (b) the result of removing the zero-offset influence on numerical integration of velocity from Figure 5a.

We found that the oscilloscope generates a very small negative constant zero offset. As the theory of integration establishes, the numerical integration of this constant zero offset produces a component with linear evolution, experimentally confirmed in Figure 5a by the evolution with negative slope. The removal of this linear component produces the result from Figure 5b (the evolution emphasized in blue).

It is evident that Figure 5b is not the expected evolution of the vibration displacement in beating phenomenon. Surely, there is not a mistake in the numerical integration proposal in Equation (8) because the numerical derivative of the evolution from Figure 5b using Equation (7) produces exactly the evolution of velocity, as Figure 6 indicates (by comparison with Figure 3).

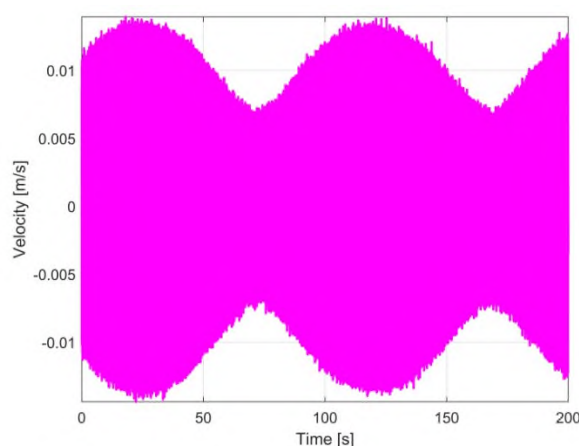


Figure 6. The result of the numerical derivative of the evolution from Figure 5b (vibration velocity, practically similar with Figure 3).

Our first attempt to explain this deficiency in this result of numerical integration is related by the constant of integration C .

Intuitively it is supposed that somehow the hypothesis that $C = 0$ is wrong. Perhaps the effect of this wrong hypothesis is mirrored in the evolution from Figure 5b and its effect should be removed (as the influence of negative zero offset was removed before).

It was discovered by numerical simulation that the numerical integration of a computer-generated beating vibration velocity signal (similarly to those depicted in Figure 3) using Equation (8), with $C = 0$, produces a vertically shifted evolution with a constant nonzero value, which should be mathematically removed.

This approach assumed that in the result of numerical integration of vibration velocity depicted in Figure 5b, a supplementary low frequency component was generated and should be removed. For the time being we unfortunately do not have a consistent explanation for the appearance of this low frequency component. This low frequency component (depicted in Figure 5b in white) was detected by low-pass numerical filtering of the vibration displacement signal (the evolution emphasised in blue).

A computer-generated moving average filter [43] was used, with the first notch frequency equal to the combination frequency $f_c = (f_1 + f_2)/2$ (assuming that this definition from Equation (6) is accurate), in order to completely remove the variable component from Figure 5b having the resultant vibration frequency, and in order to obtain the low frequency component. The number of points in the average of the filter is defined as integer of the ratio $1/(f_c \Delta t)$. The removal of this low frequency component from the result of numerical integration (the vibration displacement signal) depicted in Figure 5b is shown in Figure 7. It is obvious that this evolution properly describes the resultant vibration displacement during the beating phenomenon, previously described in Figure 3, by the velocity of the resultant vibration.

There is a supplementary confirmation of this result: the numerical differentiation of the vibration displacement signal from Figure 7 (using Equation (7)) fits very well with the vibration velocity signal from Figure 3, as a very short detail (15 ms duration) of both evolutions (given in Figure 8a) from the area labelled as A (Figures 3 and 7) indicates. Thus, the absolute velocity vibration sensor together with the proposed numerical signal integration method acts as an absolute displacement vibration sensor.

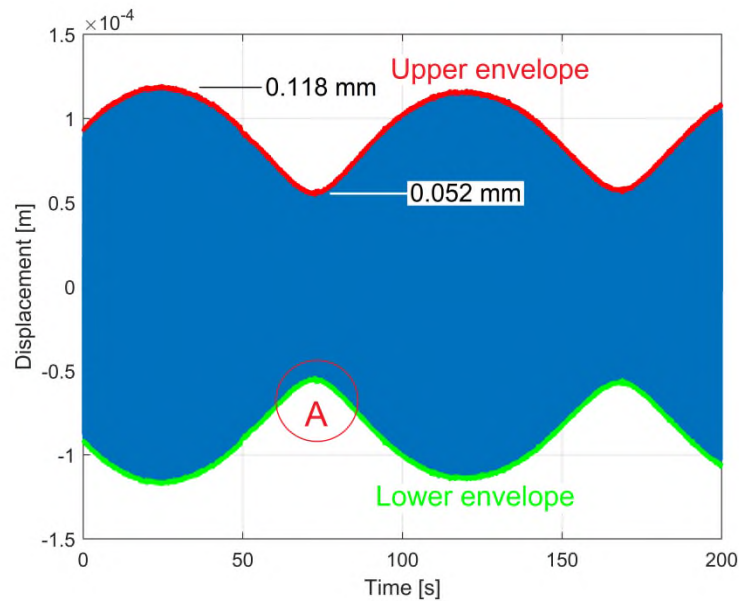


Figure 7. The headstock vibration displacement evolution during the beating phenomenon, deduced by numerical integration and correction of the signal depicted in Figure 3.

Figure 8b presents a short detail of the vibration displacement evolution in the area labelled with A in Figure 7. This figure has the same size on the abscissa as Figure 4. By comparison with Figure 4, the evolution is much smoother here, as a consequence of numerical integration, which drastically reduces the amplitudes of high frequency components. The integration acts as a low-pass filter.

In Figure 7 two relationships between the vibrations amplitudes A_1 and A_2 are available (from Equations (1) and (2)) due to the constructive interference in anti-nodes ($A_1 + A_2 = 118 \mu m$) and destructive interference in nodes ($A_1 - A_2 = 52 \mu m$), so $A_1 = 85 \mu m$ and $A_2 = 33 \mu m$. For the time being A_1 does not necessarily refer to vibration amplitude generated by the main spindle or shaft 1.

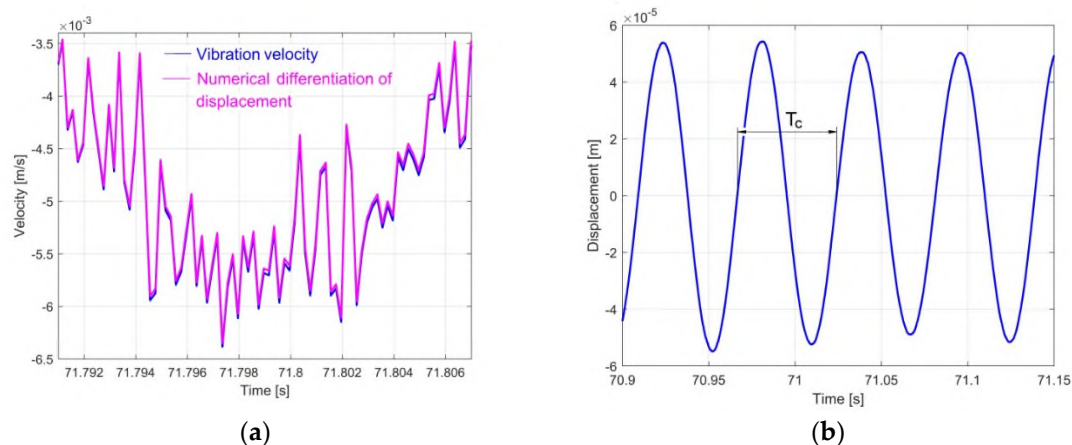


Figure 8. (a) A detail concerning the evolution of velocity (Figure 3) overlaid on the numerical differentiation of the displacement depicted in Figure 7; and (b) a detail of area A of Figure 7 with T_c , the period of the resultant vibration.

4.3. The Evolution of Frequency for Resultant Vibration in Beating Phenomenon

An interesting item in the beating phenomenon is the evolution of frequency of the resultant vibration f_c (also known as combination frequency or modulation frequency, $f_c = 1/T_c$, with T_c highlighted in Figure 8b). In [39] this frequency is defined as the average of both frequencies (f_1, f_2) involved in the beating (Equation (6)).

A beating phenomenon was simulated using the sum of two harmonic vibrations displacements $y_{1s}(A_1, f_1)$ and $y_{2s}(A_2, f_2)$ —already described in Equations (1) and (2) with different values of amplitudes ($A_2 > A_1$) and frequencies f_1 and f_2 , close to those from the experiment described in Figures 3 and 7 (with $f_1 = 17.3856$ Hz and $f_2 = 17.3959$ Hz), for a duration equal to T_b (placed between two anti-nodes).

For six different values of amplitudes (A_1 increases and A_2 decreases), the evolution of the combination frequency f_c and its average value was determined on the vibration beating simulated signal, as Figure 9 indicates, using a high accuracy measurement technique from a previous work [42]. Here each peak describes the value of frequency f_c in vibration beating node. It is obvious that f_c is not constant and, in contradiction with Equation (6) and [39], $f_c \neq (f_1 + f_2)/2$. Here, with $A_1 > A_2$ the average f_c is very close to f_2 , with $f_c > f_2$.

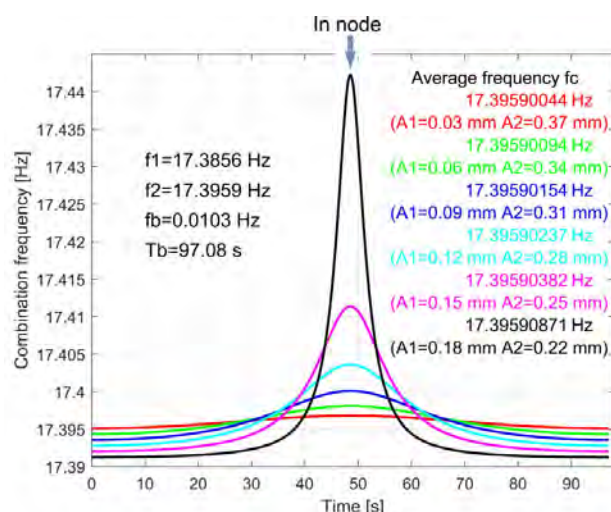


Figure 9. The evolution of the instantaneous combination frequency f_c on the simulated vibration beating during a beat period T_b (with $A_2 > A_1$ and $f_2 > f_1$).

A similar simulation was done in the same conditions, now with $A_1 > A_2$, as Figure 10 indicates (here A_1 decreases and A_2 increases). Similar to the simulation given in Figure 9, it is obvious that f_c is not constant and again, in contradiction with Equation (6) and [39], $f_c \neq (f_1 + f_2)/2$. The average frequency f_c is very close to f_1 , with $f_c < f_1$.

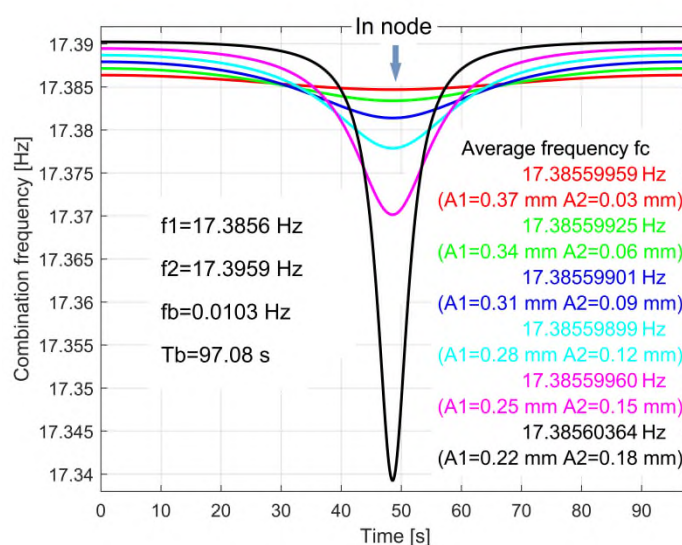


Figure 10. The evolution of the instantaneous combination frequency on simulated vibration beating during a beat period (the same condition as in Figure 9, except for the amplitudes relationship: $A_1 > A_2$).

There are two conclusions here, in contradiction with the literature [39]:

- The combination frequency f_c is not constant over a period T_b (even if its variation is not significant);
- The average value of the combination frequency f_c over a period T_b is practically the same as the frequency of the input vibration in the beating phenomenon ($y_{1s}(A_1, f_1)$ or $y_{2s}(A_2, f_2)$), whose amplitudes are higher (e.g., if $A_2 > A_1$ then the average $f_c \approx f_2$).

Some supplementary simulations for many other values of frequencies f_1 and f_2 (and consequently T_b) completely confirm these conclusions.

Figure 11 presents the evolution of the instantaneous combination frequency f_c during the vibration beating phenomenon (displacement of headstock) experimentally described in Figure 7.

Apparently, this is a very noisy evolution. The dominant component of the signal from Figure 7 is the displacement of resultant vibration $y_1 + y_2$. The frequency measurement method [42] is based on detection of zero-crossing moments of this signal (a topic discussed later on). It is obvious that many other additional vibrations of the lathe headstock (some of them with high frequency) disturb the accuracy of the zero-crossing detections, as a main reason for the noisy evolution from Figure 11.

The best information available in Figure 11 is the average value of the combination frequency f_c ($\bar{f}_c = 17.3830$ Hz, very close to the rotational frequency of the main spindle, $f_1 = 17.3856$ Hz). Based on the previous conclusions from Figures 9 and 10 it is evident that the amplitude A_1 of unbalanced vibration generated by the main spindle (shaft 1) is higher than the amplitude A_2 of shaft 2 (so $A_1 = 85 \mu m$ and $A_2 = 33 \mu m$, an item analysed before). As previously mentioned, the rotational frequency of shaft 2 is $f_2 = f_1 - f_b = 17.3752$ Hz or $f_2 = f_1 + f_b = 17.3959$ Hz.

Figure 12 presents a low-pass filtered evolution of the instantaneous combination frequency from Figure 11, (using a multiple moving average filter [43], as a well-known method to attenuate the signal noise).

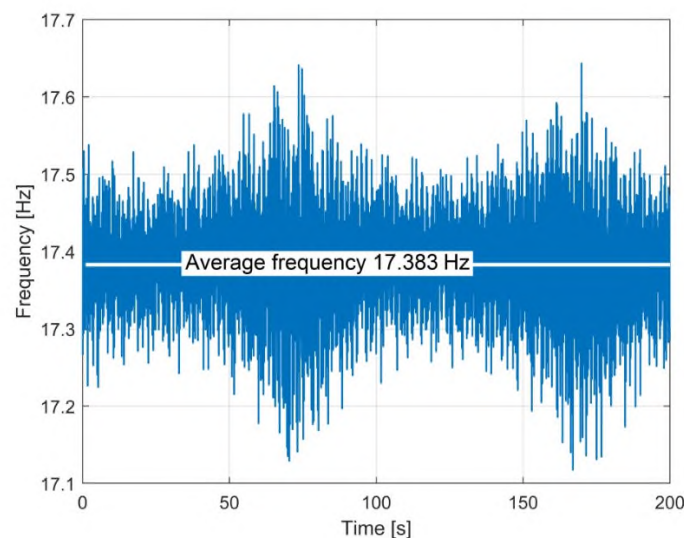


Figure 11. The evolution of the instantaneous combination frequency f_c during the vibration beating phenomenon (displacement of headstock) described in Figure 7.

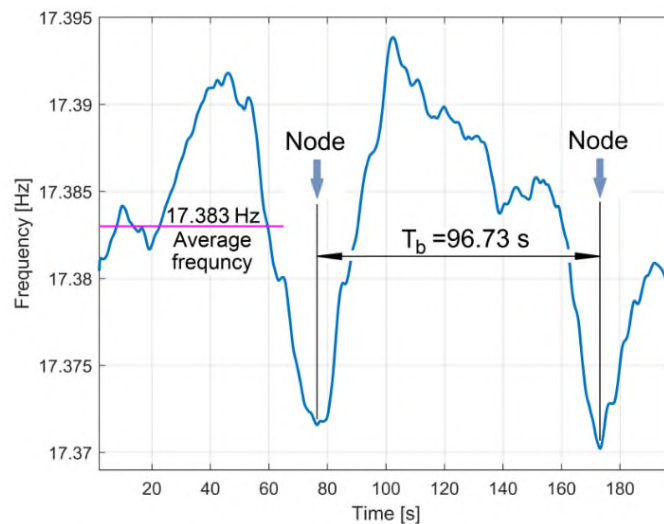


Figure 12. The evolution of the low pass filtered instantaneous combination frequency f_c during the vibration beating phenomenon described in Figure 7 (a low pass filtering of Figure 11).

Despite a relatively strong irregular variation of the combination frequency f_c (due to the variation of experimental conditions: e.g., the small variation of rotational speeds of shafts 1 and 2, caused mainly by the variation of frequency of the supplying voltages applied to the asynchronous driving motor, around a theoretical value of 50 Hz, as Figure 13 clearly indicates), the previous simulations and conclusions are fully experimentally confirmed. Three supplementary identical experiments confirm the evolution presented in Figure 12.

Firstly, in Figure 12 there are two negative peaks (for the two nodes in Figures 3 or 7; each node produces a negative peak on f_c evolution, an item already discussed in the simulation from Figure 10) at a time interval very close to the beat period value T_b , already defined in Figure 3 (96.73 s here, compared with 96.6 s in Figure 3).

Secondly, as shown in Figure 14, a superposition of filtered frequency f_c evolution from Figure 12 (here in a conventional blue coloured description) over the experimental envelopes of vibration displacement in beating (the same as those depicted in Figure 7) indicates that the negative peaks of f_c are placed, as expected, in nodes.

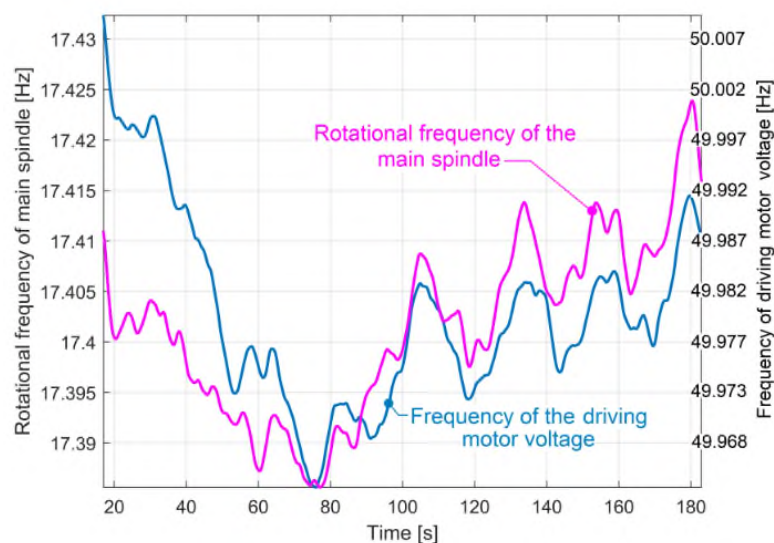


Figure 13. Low-pass filtered rotational frequency evolution of the main spindle and supplying voltage frequency evolution of the driving motor.

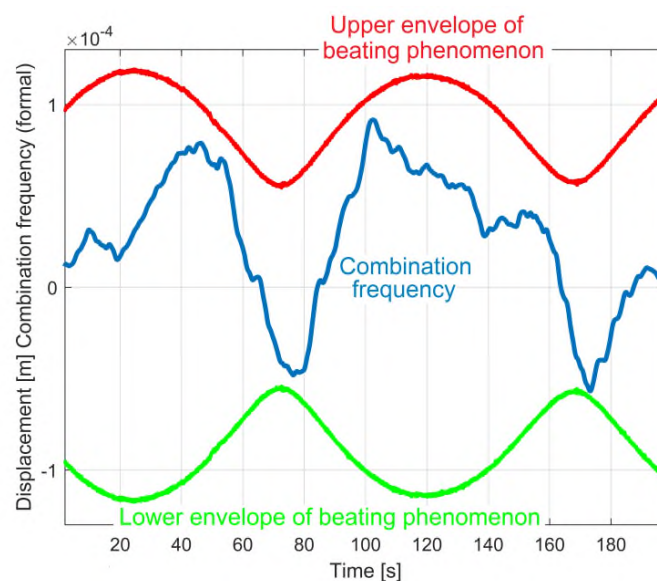


Figure 14. The position of negative peaks on the combination frequency (formally represented) relative to the position of nodes on the vibration beating phenomenon.

The small displacement to the right of the negative peaks of the filtered combination frequency evolution (as against the nodes on Figure 14) is not related to the numerical filtering. This is proved by the result of the simulation of Figure 14, as given in Figure 15 (with addition of pure harmonic signals y_{1s} and y_{2s} in vibration beating simulation).

This periodic pattern of filtered combination frequency f_c evolution experimentally revealed in Figures 12 and 14 (according to the simulations from Figures 10 and 15) is strongly attenuated if the amplitude A_2 becomes significantly lower than A_1 (and vice versa).

An important question is in order here due to a very small variation of filtered frequencies revealed before (less than 50 mHz full scale evolution in Figures 9, 10, 12, 13 and 15): how accurate is this frequency measurement method [42]?

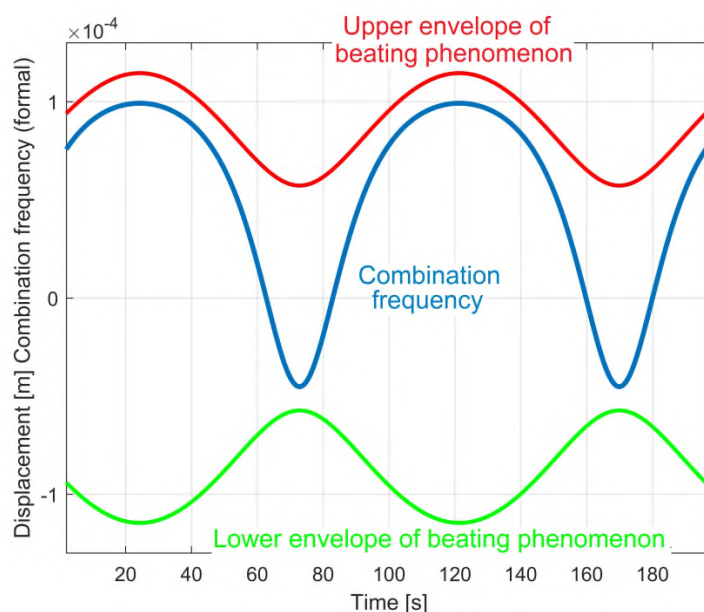


Figure 15. The result of a numerical simulation for the evolutions described in Figure 14.

In this measurement method (e.g., the measurement of the combination frequency f_c of vibration displacement signal from Figure 7), the computer-aided detection of the time interval between each

two consecutive zero-crossing moments (t_{zcj} and t_{zcj+1}) of a periodical signal is used. This time interval defines a semi-period $T_c/2 = t_{zcj+1} - t_{zcj}$ as $T_c/2 = 1/2f_c$, or a value $f_c = 1/T_c$. When the result of multiplication of two successive displacements samples s_i and s_{i-1} (having the sampling times t_i and t_{i-1} , with $i > 1$) is negative or zero ($s_i \cdot s_{i-1} < 0$ or $s_i \cdot s_{i-1} = 0$) a zero-crossing moment is detected (e.g., t_{zcj}) and calculable as the abscissa of the intersection of a line segment defined by the points of coordinates (t_i, s_i) and (t_{i-1}, s_{i-1}) on the t -axis (as x -axis in Figure 8b). The main reason for frequency measurement error $\varepsilon_f \neq 0$ is a consequence of calculation errors for two successive zero-crossing moments $\varepsilon_j \neq 0$ (for t_{zcj}) and $\varepsilon_{j+1} \neq 0$ (for t_{zcj+1}). These ε_j and ε_{j+1} errors are caused by the replacement of a harmonic evolution with a linear evolution between those two successive displacement samples involved in each zero-crossing moment definition. With $t_{i-1} - t_i = \Delta t$ (Δt being the sampling interval) the error $\varepsilon_j = 0$ only in three situations: (1) if $s_i = 0$ (the end of the line segment is placed on the t -axis, with $t_j = t_i$), (2) if $s_{i-1} = 0$ (the start of line segment is placed on t -axis, with $t_j = t_{i-1}$) and (3) if $-s_i = s_{i-1}$ (the middle of the line segment is placed on t -axis, with $t_j = t_{i-1} + \Delta t/2$). A similar approach is available for the next two successive samples (s_{i+h} and s_{i+h-1}) involved in the definition of t_{zcj+1} moment and ε_{j+1} error (with h as the integer part of the ratio $T_c/\Delta t$). If simultaneously ε_j and $\varepsilon_{j+1} = 0$ then $\varepsilon_f = 0$. Any other definition of sampling times generates frequency measurement errors $\varepsilon_f \neq 0$.

A computer-aided calculus was performed for frequency measurement error ε_f of a harmonic simulated signal with frequency 17.383 Hz (the average value of the combination frequency f_c) during a semi-period. Here 10,000 different values of sampling time t_1 (between 0 and Δt , with $\Delta t = 200 \mu s$, the same sampling interval as in Figures 3 and 7) and $t_2 = \Delta t - t_1$ (between Δt and 0) for the first two successive displacement samples involved in the calculus of the first zero-crossing moment t_{zc1} was used. Figure 16 describes the evolution of the frequency measurement error $\varepsilon_f(t_1)$.

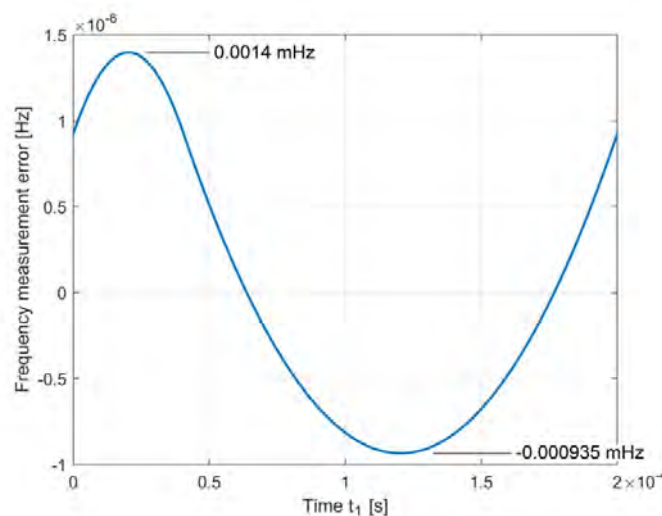


Figure 16. The evolution of the frequency measurement error ε_f (for a simulated harmonic signal with combination frequency $f_c = 17.383$ Hz) versus the evolution of the first sampling time ($t_1 = 0 \div \Delta t$, or $t_1 = 0 \div 200 \mu s$) involved in the first zero-crossing time (t_{zc1}) calculus.

As Figure 16 clearly indicates, the frequency measurement error ε_f of the combination frequency f_c is variable and placed between -0.000935 and $+0.0014$ mHz. The result of the measured frequency of the simulated signal is $17.383^{+1.4}_{-0.935} \mu Hz$ as a description of the accuracy measurement. Very similar limits for the ε_f error are calculated for a harmonic signal with frequency f_1 . If the value of the frequency $f_c = 1/T_c$ used in simulation accomplishes the condition $T_c = h\Delta t$ (with h being an integer), then $\varepsilon_f = 0$ for any value $t_1 = 0 \div \Delta t$.

4.4. The Influence of the Lathe Suspension Dynamics on Beating Vibrations Amplitude

The relative high vibration displacement amplitude of the headstock during the beating phenomenon (as shown in Figure 7) has an evident explanation: the vibration frequencies f_1 , f_2 and f_c

as well, are close to the first resonant frequency (vibration mode) of the headstock and lathe on its foundation (as a single body mass–spring–damper vibratory system). This means that the dynamic amplification factors D_{af1} and D_{af2} , (involved in Equations (1) and (2)) are significantly higher than 1 (because of resonant amplification). In order to prove that, the resources of a very simple experiment performed with the same experimental setup are available: the evolution of headstock vibration velocity after an impulse excitation produced with a rubber mallet (hammer) in the same direction with y_1 and y_2 vibrations (as Figure 17 describes).

Here the blue curve partially depicts the free damped vibration velocity v_{fd} (acquired with the geophone sensor); the red coloured one depicts the best fitting curve of a part of the free response (with 25,000 samples and 500 ns sampling time). The curve fitting [44] was done in Matlab, with an adequate computer program specially designed for this paper, based on a known theoretical model of free viscous damped vibration velocity response [45]:

$$v_{fd}(t) = a \cdot e^{-bt} \sin(p_1 t + \alpha) \quad (9)$$

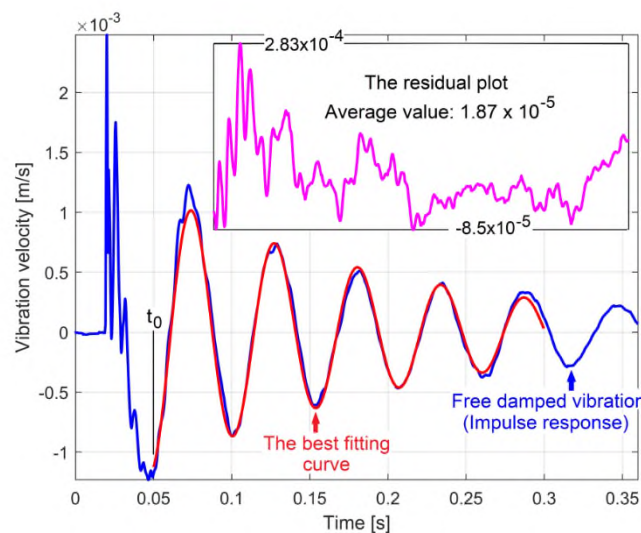


Figure 17. Some experimental results on signal processing related to free damped vibration of headstock after an impulse excitation (with a rubber mallet).

The best fitting curve (in red in Figure 17) is described with $a = 1.170 \cdot 10^{-3} \text{ m/s}$, $b = 5.899 \text{ s}^{-1}$ (as damping constant), $p_1 = 117.952 \text{ rad/s}$ (as angular frequency of damped harmonic vibration) and $\alpha = 4.986 \text{ rad}$ (as phase angle at the origin of time t_0 on Figure 17). The angular natural frequency ($p = \sqrt{p_1^2 + n^2} = 118.099 \text{ rad/s}$) and the damping constant b are useful in the definition [45] of dimensionless dynamic amplification factor D_{af} from forced vibrations of harmonic excitation (as happens during the beating phenomenon, assuming that the combination frequency is approximately constant):

$$D_{af} = \frac{1}{\sqrt{[1 - (\frac{\omega}{p})^2]^2 + (2 \frac{\omega}{p} \cdot \frac{b}{p})^2}} \quad (10)$$

Here $\omega = 2\pi f$ is the angular frequency of harmonic excitation on frequency f . Based on previous experimental results of curve fitting (with b and p values in Equation (10)) Figure 18 presents the simulated evolution of D_{af} related to the frequency of excitation (1 ÷ 35 Hz range). Because of a low damping constant b , the system presents resonant amplification, with a maximum value $D_{af} = 10.01$ on $f = 18.749 \text{ Hz}$ frequency.

Based on the previous experimentally determined frequencies f_1 and f_2 , with $f = f_1 = 17.3856 \text{ Hz}$ gives the result $D_{af1} = 5.831$ and with $f = f_2 = 17.3752 \text{ Hz}$ (or $f = f_2 = 17.3959 \text{ Hz}$) the result is $D_{af2} = 5.803$

(or $D_{af2} = 5.859$). For $f = \bar{f}_c = 17.383$ Hz (Figure 12) the result is $D_{afc} = 5.824$ (the coordinates of point A on Figure 18). This means that, because of mechanical resonance, the vibration amplitude generated by the beating phenomenon of the headstock and the lathe on its foundation (already revealed in Figure 7) is amplified on average by 5.824 times.

Besides the amplification of the vibration, the resonant behaviour also introduces a significant shift of phase γ between the excitation (unbalancing) force and the vibration displacement, theoretically described [45] as depending on ω (and excitation frequency f as well) with the equation:

$$\gamma = \arctan \left[\frac{2 \frac{b}{p} \frac{\omega}{p}}{1 - \left(\frac{\omega}{p} \right)^2} \right] \quad (11)$$

With the b and p values previously determined, the values of shift of phase calculated for each frequency are: $\gamma_1 = 0.5691$ rad for $f = f_1 = 17.3856$ Hz and $\gamma_2 = 0.5656$ rad (or $\gamma_2 = 0.5725$ rad) for $f = f_2 = 17.3752$ Hz (or $f_2 = 17.3959$ Hz). For $f = \bar{f}_c = 17.383$ Hz the result is $\gamma_c = 0.5682$ rad.

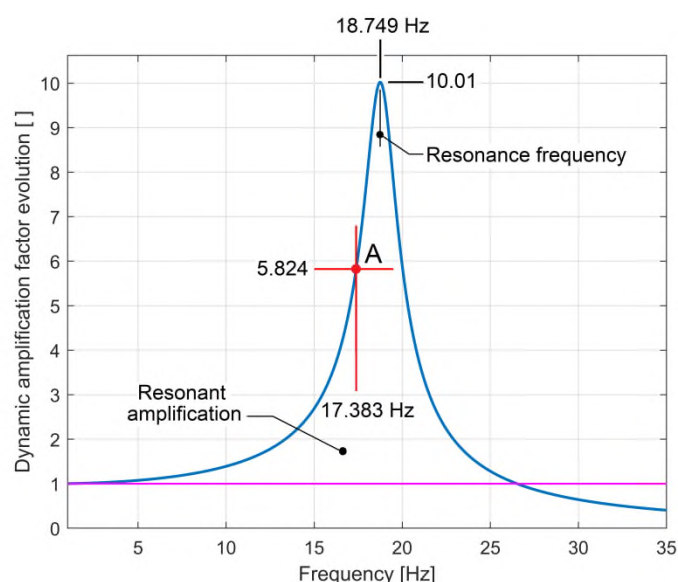


Figure 18. The evolution of the dynamic amplification factor D_{af} generated by the headstock foundation in the resonance area, based on Equation (10) and experimental free damped response analysis.

The knowledge of both of these resonant characteristics (the value of the dynamic amplification factor D_{af} and especially the phase shift γ) is important for a next approach of the dynamic balancing of these two shafts placed inside the headstock.

As a general comment, we should mention that the resonance behaviour of this low damped vibratory system—as previously mentioned—is a consequence of the disponibility of this system to absorb modal mechanical energy. The system works as a narrow-band modal energy absorber [46].

5. Conclusions and Future Work

Some specific features of the beating vibration phenomenon discovered on a headstock lathe have been revealed in this paper.

An experimental description (with theoretical approaches based on simulations) of this beating vibration phenomenon with very low beat frequency (1/96.6 Hz) was performed. The beating phenomenon occurs due to the addition of vibrations produced by two unbalanced shafts, rotating with very close instantaneous angular speeds (rotating frequencies), with constructive interference in anti-nodes and destructive interference in nodes.

The absolute velocity signal of vibration beating (delivered by a vibration electro-dynamic sensor placed on the headstock) was converted into a displacement signal. For this purpose, a fully confirmed method of numerical integration (antiderivative calculus), with theoretical and experimental approaches was applied. This method is deduced from the approximation of the formula for the first derivative of displacement, as a backward finite difference [43]). An appropriate technique of correction of this numerical antiderivative calculus method was also introduced (mainly by removing the low frequency displacement signal component generated by numerical integration). Thus, an absolute velocity vibration sensor together with a numerical integration procedure plays the role of an absolute vibration displacement sensor.

A consistent part of the research was focused on the resultant vibration displacement signal, mainly on the evolution of frequency (or the combination frequency f_c) related to the nodes and anti-nodes position. It was theoretically discovered (by simulation) and was experimentally proved that, in opposition to the literature reports, the combination frequency is not constant, and the definition of its average value is wrong. The evolution of the combination frequency has a specific periodic pattern (having the same frequency as the beat frequency) with small variation (tens of millihertz) and negative or positive peaks placed in beating nodes. The appearance of these peaks (negative or positive) depends on the relationship between amplitudes and frequencies of vibrations involved in the beating phenomenon. The small variation of frequency inside the pattern and the correlation between the frequencies of different experimental signals (the combination frequency f_c , the rotation frequency f_1 of the main spindle, and the supply voltage frequency of the driving motor) have been correctly described as a result of a high accuracy procedure of frequency measurement, developed in a previous work [42] and successfully applied here. It was proved on a simulated signal (having a frequency of 17.383 Hz, equal to the average value of the combination frequency in vibration beating phenomenon) that this procedure has less than $\pm 1.5 \mu\text{Hz}$ measurement error.

The influence of the behaviour of the headstock and lathe foundation dynamics (as a rigid body placed on a spring–damper system) on the vibration induced by unbalanced rotors and the beating phenomenon was also investigated. Based on computer-aided analysis of free damped viscous response (by curve fitting), the characteristics of foundation dynamics were experimentally revealed (mainly the values of natural angular frequency and the damping constant). Considering these values, the dynamic amplification factors of vibrations (mainly of the resultant vibration) and phase shift between centrifugal forces (as excitation forces produced by unbalanced rotary shafts) and the vibrations generated by these forces were calculated.

For each experiment, numerical simulation and signal processing procedures, several computer programs written in Matlab were successfully used.

In the future, the theoretical and experimental approaches will be focused on the influence of dynamic unbalancing and vibration beating on the active and instantaneous electrical power absorbed by the driving motor of the headstock. There is a logical reasoning for these approaches: the headstock vibration motion (especially during the resonant amplification behaviour revealed in Figure 18) should be mechanically powered. Of course, the instantaneous and active mechanical power (difficult to measure) is delivered by the driving motor as an equivalent of instantaneous and active electric power absorbed from the electrical supply network (easier to measure).

Several theoretical and experimental studies on computer-aided balancing of each rotary shaft inside the lathe headstock will be performed (using two absolute velocity sensors and an appropriate method of computer-assisted experimental balancing). A study on the vibration beating phenomenon produced by more than two unbalanced rotary bodies will be done.

Author Contributions: Conceptualization, D.-F.C. and M.H.; methodology, D.-F.C. and M.H.; software, F.N. and C.-G.D.; validation, M.H. and C.G.D.; formal analysis, D.-F.C. and M.H.; investigation, D.-F.C., C.-G.D. and M.H.; resources, M.H.; data curation, M.H.; numerical integration method, M.H.; writing—original draft preparation D.-F.C. and M.H.; writing—review and editing, G.D., M.I.; visualization, M.H. and F.N.; supervision, M.H. and C.-G.D.; project administration, M.H. and C.-G.D.; funding acquisition, D.-F.C., G.D. and M.I. All authors have read and agreed to the published version of the manuscript.

Funding: This work was accomplished with the support of the COMPETE project nr. 9PFE/2018, funded by the Romanian Government.

Acknowledgments: This work was accomplished with the support of COMPETE project nr. 9PFE/2018, funded by the Romanian Government.

Conflicts of Interest: “The authors declare no conflict of interest.”

Nomenclature

A_1, A_2	The amplitudes of vibrations y_1, y_2 [m]
ae^{-bt}	The envelope of free viscous damped vibration velocity response [m/s]
b	The damping constant [s^{-1}]
C	The constant of velocity signal integration [m]
D_{af}	Theoretical dynamic amplification factors of vibrations []
D_{af1}, D_{af2}	Dynamic amplification factors of vibrations y_1, y_2 produced by shafts 1, 2 []
D_{afc}	Dynamic amplification factor of resultant vibration $y_1 + y_2$ at average frequency f_c []
$dy_1/dt, dy_2/dt$	The derivative of vibration displacements y_1, y_2 (vibration velocities) [m/s]
f	The frequency of harmonic excitation of the lathe headstock [Hz]
F_1, F_2	The horizontal projection of the rotary unbalance forces generated by shafts 1 and 2 [N]
f_1, f_2	The frequency of vibrations y_1, y_2 [Hz]
f_b	The beat frequency [Hz]
f_c	The frequency of the resultant vibration $y_1 + y_2$, or combination frequency [Hz]
IAS	Instantaneous angular speed [rad/s]
k	The stiffness of headstock and lathe foundation [N/m]
m_1, m_2	Unbalance mass on rotary shafts 1, 2 [Kg]
n	A natural number involved in the definition of the beat period T_b
p	The natural angular frequency [rad/s]
p_1	The angular frequency of damped harmonic vibration [rad/s]
r_1, r_2	The distance between the center of the unbalance mass and the rotation axis on shafts 1, 2 [m]
s	The addition of vibration displacements $s = y_1 + y_2$ [m]
S_i, S_{i+1}	Two successive displacement samples of vibration [m]
S_{i+h}, S_{i+h-1}	Two successive displacement samples of vibration [m]
t	Time [s]
t_0	The origin of time for the theoretical model of free damped vibration velocity [s]
t_{zci}, t_{zci+1}	Two successive zero-crossing moments of the displacement vibration signal involved in frequency measurement [s]
Δt	Sampling interval for a numerically described signal [s]
T_1, T_2	The periods of vibrations y_1, y_2 [s]
T_b	The beat period, with $T_b = 1/f_b$ [s]
T_c	The period of the resultant vibration $y_1 + y_2$, with $T_c = 1/f_c$ [s]
v	The velocity of the resultant vibration in beating [m/s]
v_{fd}	The vibration velocity of the headstock during a free damped response [m/s]
v_i	A sample of the vibration velocity [m/s]
y_1, y_2	The vibration displacement generated by shafts 1, 2 [m]
y_{1s}, y_{2s}	Simulated vibration displacement signals [m]
α	The phase angle at the origin of time t_0 for a theoretical model of free damped vibration velocity [rad/s]
ε_f	The error in the frequency measurement [Hz]
$\varepsilon_i, \varepsilon_{i+1}$	The calculus errors for two successive zero-crossing moments [s]
γ	The shift of phase between the excitation force and the vibration displacement in the free damped response [rad]
θ_1, θ_2	The instantaneous value of the angle of centrifugal forces to the horizontal direction [rad]
φ_1, φ_2	The values of θ_1 and θ_2 at the origin of time, $t = 0$ [rad]
ω	The angular frequency of harmonic excitation of the lathe headstock [rad/s]
ω_1, ω_2	The instantaneous angular speed of the rotary shafts 1, 2 [rad/s]

References

- Muszyńska, A. *Rotordynamics*; CRC Press: Boca Raton, FL, USA, 2005; ISBN 978-0-8247-2399-6.
- Wang, Y.; Yuan, X.; Sun, R. Critical techniques of design for large scale centrifugal shakers. *World Inf. Earthq. Eng.* **2011**, *27*, 113–123.
- Anekar, N. Design and testing of unbalanced mass mechanical vibration exciter. *IJRET* **2014**, *3*, 107–112.
- Conley, K.; Foyer, A.; Hara, P.; Janik, T.; Reichard, J.; D'Souza, J.; Tamma, C.; Ababei, C. Vibration alert bracelet for notification of the visually and hearing impaired. *J. Open Hardw.* **2019**, *3*, 4, doi:10.5334/joh.17.
- Fontana, F.; Papetti, S.; Jarvelainen, H.; Avanzini, F. Detection of keyboard vibrations and effects on perceived piano quality. *J. Acoust. Soc. Am.* **2017**, *142*, 2953–2967.
- Ippolito, R.; Settineri, L.; Sciamanda, M. Vibration monitoring and classification in centerless grinding. In *International Centre for Mechanical Sciences (Courses and Lectures)*; Kuljanic, E., Eds.; Springer: Vienna, Austria, 1999; p. 406, doi:10.1007/978-3-7091-2508-3_18.
- Merino, R.; Barrenetxea, D.; Munoa, J.; Dombovari, Z. Analysis of the beating frequencies in dressing and its effect in surface waviness. *CIRP Annal. Manuf. Technol.* **2019**, *68*, 353–356.
- Mayoof, F.N. Beating phenomenon of multi-harmonics defect frequencies in a rolling element bearing: Case study from water pumping station. *World Acad. Sci. Eng. Technol.* **2009**, *57*, 327–331.
- Pham, M.T.; Kim, J.-M.; Kim, C.H. Accurate bearing fault diagnosis under variable shaft speed using convolutional neural networks and vibration spectrogram. *Appl. Sci.* **2020**, *10*, 6385.
- Park, J.; Lee, J.; Ahn, S.; Jeong, W. Reduced ride comfort caused by beating idle vibrations in passenger vehicles. *Int. J. Ind. Ergon.* **2017**, *57*, 74–79.
- Huang, P.; Lee, W.B.; Chan, C.Y. Investigation of the effects of spindle unbalance induced error motion on machining accuracy in ultra-precision diamond turning. *IJMTM* **2015**, *94*, 48–56, doi:10.1016/j.ijmachtools.2015.04.007.
- Norfield, D. *Practical Balancing of Rotating Machinery*; Elsevier Science: Amsterdam, The Netherlands, 2005.
- Thearle, E.L.; Schenectady, N.Y. Dynamic balancing of rotating machinery in the field. *ASME Trans.* **1934**, *56*, 10, 745–775.
- Kelm, R.; Kelm, W.; Pavelek, D. Rotor Balancing Tutorial. In Proceedings of the 45th Turbomachinery and 32th Pump Symposia, Houston, TX, USA, 12–16 September, 2016.
- Wijk, V.; Herder, J.L.; Demeulenaere, B. Comparison of various dynamic balancing principles regarding additional mass and additional inertia. *J. Mech. Robot.* **2009**, *1*, 4, doi:10.1115/1.3211022.
- Isavand, J.; Kasaei, A.; Peplow, A.; Afzali, B.; Shirzadi, E. Comparison of vibration and acoustic responses in a rotary machine balancing process. *Appl. Acoust.* **2020**, *164*, 107258.
- Bertoneri, M.; Forte, P. Turbomachinery high speed modal balancing: Modelling and testing of scale rotors. In *Proceedings of the 9th IFToMM International Conference on Rotor Dynamics. Mechanisms and Machine Science, Proceedings of the 9th IFToMM International Conference on Rotor Dynamics. Mechanisms and Machine Science, Milan, Italy, 22–25 September 2017*; Pennacchi, P., Ed; Springer: Cham, Switzerland, 2017, doi:10.1007/978-3-319-06590-8_2.
- Caoa, H.; Dörgelohb, T.; Riemer, O.; Brinksmeier, E. Adaptive separation of unbalance vibration in air bearing spindles. *Proc. CIRP* **2017**, *62*, 357–362.
- Majewski, T.; Szwedowicz, D.; Melo, M.A.M. Self-balancing system of the disk on an elastic shaft. *J. Sound Vib.* **2015**, *359*, 2–20.
- Hashimoto, F.; Gallego, I.; Oliveira, J.F.G.; Barrenetxea, D.; Takahashi, M.; Sakakibara, K.; Stalfelt, H.O.; Staadt, G.; Ogawa, K. Advances in centerless grinding technology. *CIRP Annal.* **2012**, *61*, 747–770.
- Zhang, Z.X.; Wang, L.Z.; Jin, Z.J.; Zhang, Q.; Li, X.L. Non-whole beat correlation method for the identification of an unbalance response of a dual-rotor system with a slight rotating speed difference. *MSSP* **2013**, *39*, 452–460.
- Zhang, Z.X.; Zhang, Q.; Li, X.L.; Qian, T.L. The whole-beat correlation method for the identification of an unbalance response of a dual-rotor system with a slight rotating speed difference. *MSSP* **2011**, *25*, 1667–1673.
- Lee, Y.J. 8.03SC Physics III: Vibrations and Waves. Fall 2016. Massachusetts Institute of Technology: MIT Open CourseWare, 2016. Available online: <https://ocw.mit.edu> (accessed on 17 September 2020).
- Kim, S.H.; Lee, C.W.; Lee, J.M. Beat characteristics and beat maps of the King Seong-deok Divine Bell. *JSV* **2005**, *281*, 21–44.

25. Yuan, L.; Järvenpää, V.M. On paper machine roll contact with beating vibrations. *Appl. Math. Mech.* **2006**, *6*, 343–344, doi:10.1002/pamm.200610153.
26. Gao, H.; Meng, X.; Qian, K. The Impact analysis of Beating vibration for active magnetic bearing. *IEEE Access* **2019**, *7*, 134104–134112.
27. Preumont, A. *Twelve lectures on Structural Dynamics*; Université Libre de Bruxelles: Brussels, Belgium, 2012.
28. Horodincă, M.; Seghedin, N.; Carata, E.; Boca, M.; Filipoiu, C.; Chitariu, D. Dynamic characterization of a piezoelectric actuated cantilever beam using energetic parameters. *Mech. Adv. Mater. Struct.* **2014**, *21*, 154–164.
29. Endo, H.; Suzuki, H. Beating vibration phenomenon of a very large floating structure. *J. Mar. Sci. Technol.* **2018**, *23*, 662–677.
30. Carrino, S.; Nicassio, F.; Scarselli, G. Subharmonics and beating: A new approach to local defect resonance for bonded single lap joints. *J. Sound Vib.* **2019**, *456*, 289–305.
31. Cattarius, J.; Inman, D.J. Experimental verification of intelligent fault detection in rotor blades. *Int. J. Syst. Sci.* **2000**, *31*, 1375–1379.
32. Morrone, A. Seismic vibration testing with sine beats. *Nucl. Eng. Des.* **1973**, *24*, 344–356.
33. Huang, H.H.; Chen, K.S. Design, analysis, and experimental studies of a novel PVDF-based piezoelectric energy harvester with beating mechanisms. *Sens. Actuators A Phys.* **2016**, *238*, 317–328.
34. Basovich, S.; Arogeti, S. Identification and robust control for regenerative chatter in internal turning with simultaneous compensation of machining error. *Mech. Syst. Sign. Process.* **2021**, *149*, 107208.
35. Li, D.; Cao, H.; Liu, J.; Zhang, X.; Chen, X. Milling chatter control based on asymmetric stiffness. *Int. J. Mach. Tools Manuf.* **2019**, *147*, 103458.
36. Yana, Y.; Xub, J.; Wiercigroch, M. Influence of work piece imbalance on regenerative and frictional grinding chatters. *Proc. IUTAM* **2017**, *22*, 146–153.
37. Kimmelman, M.; Stehle, T. Measuring unbalance-induced vibrations in rotating tools. *MATEC Web Conf.* **2017**, *121*, 03012.
38. Gohari, M.; Eydi, A.M. Modelling of shaft unbalance: Modelling a multi discs rotor using K-nearest neighbor and decision tree algorithms. *Measurement* **2020**, *151*, 107253.
39. Hui, S.; Xiaoqiang, H.; Zhiqiang, D.; Lichang, X.; Haishui, J. Research on Low Frequency Noise Caused by Beat Vibration of Rotary Compressor. In *Compressor Engineering Conference, Proceedings of the 24th International Compressor Engineering Conference, Purdue, Italy, 9–12 July 2018*; Purdue University: Purdue, Italy, 2018; paper 2528.
40. Available online: <http://hgsindia.com/www.hgsproducts.nl/Pdf/196216HG-4%20V%201.1.pdf> (accessed on 17 September 2020).
41. Available online: <https://www.picotech.com/oscilloscope/4224-4424/picoscope-4224-4424-overview> (accessed on 17 September 2020).
42. Horodincă, M.; Ciurdea, I.; Chitariu, D.F.; Munteanu, A.; Boca, M. Some approaches on instantaneous angular speed measurement using a two-phase n poles AC generator as sensor. *Measurement* **2020**, *157*, 107636, doi:10.1016/j.measurement.2020.107636.
43. Chapra, S.C.; Canale, R.P. *Numerical Methods for Engineers*, 7th ed.; McGraw Hill Education: New York, NY, USA, 2015.
44. Arlinghaus, S. *Practical Handbook of Curve Fitting*, 1st ed.; CRC Press: Boca Raton, FL, USA, 2020.
45. Shabanna, A.A. *Theory of Vibrations. An introduction*; Springer: New York, NY, USA, 1991.
46. Schmitz, T. Modal interactions for spindle, holders, and tools. *Proc. Manuf.* **2020**, *48*, 457–465.



Experimental Research on Behaviour of 3D Printed Gripper Soft Jaws

DRAGOS-FLORIN CHITARIU¹, EMILIAN PADURARU¹, GURES DOGAN¹,
MEHMET ILHAN¹, FLORIN NEGOESCU¹, CATALIN-GABRIEL DUMITRAS¹,
ADRIAN BEZNEA^{2*}, VICTORITA STEFANESCU^{2*}, IULIAN CONSTANTIN²,
SORIN BERBECE², MIHAITA HORODINCA¹

¹ Gheorghe Asachi Technical University of Iasi, Department of Machine Machine-Tool and Tools, 59A Prof.dr.doc. D. Mangeron Str., 700050, Iasi, Romania

² Dunarea de Jos University of Galati, Medicine and Pharmacy Faculty, 47 Domneasta Str., 800008, Galati, Romania

Abstract: *In this paper, the problem of the behaviour of soft jaws that can be used to replace the steel jaws of grippers is studied. One of the advantages of additive manufacturing is the printing of fully functional parts. Choice of material is often related to the part strength. The mechanical properties of 3D printed parts should meet the service loading and, also, must be comparable with parts produced by traditional manufacturing techniques - machined parts or injection moulding. From the specialized literature information regarding the test results for effect of various printing parameters on part strength are available made in laboratory conditions and for standard test sample. For ABS materials various values for Young module are presented varying from 1.5 GPa to 2.15 GPa, for 100% infill rate and various modified parameters such as raster orientation. In order to study the behaviour of soft gripper jaws several part were printing and the resistance to bending was tested, by simulating the way a gripper works. An experimental stand was built using a force transducer and a displacement transducer to measure the deformation of the jaw, obtained by 3D printing, under load. The mechanical elastic hysteresis loop during an experimental loading/unloading was plotted and the amount of mechanical energy lost during a cycle, dissipated because the internal friction, was determined. Finite element analysis method was applied to make a comparison with the experimental results. In the finite element analysis, several simulations were considered, varying Young's modulus for the tested material*

Keywords: gripper jaws, 3D printing, Experimental tests

1. Introduction

Grippers are used for orientation-positioning and tightening of the object / part during handling, processing, control and assembly. To ensure the fulfilment of the functions presented, the materials used in the construction of devices and grippers are usually alloy steel. The requirements of grippers are similar to those of clamping fixtures, namely: precise orientation and positioning according to machining requirements, rigidity depending on the size of the workpiece and machining forces, reliability, low maintenance, standardized components, high productivity, costs low [1]. To ensure the performance of the functions presented, the materials used in the construction of devices and grippers are usually alloy steel with an HRC hardness of up to 55-60 HRC for the clamping components.

There are also cases where "flexible" jaws / soft jaws are needed to reduce the deformation of workpieces, especially for thin-walled thin parts when clamping. Soft jaws are one of the simplest methods of customized workholding and can be machined to the negative shape of the workpiece.

Soft jaws can be manufactured by Additive Manufacturing (AM) methods by benefiting from the maximization of the flexibility offered by this method of manufacturing parts [2]. Additive Manufacturing (AM) is defined by the American Society for Testing and Materials as "the process of joining materials to make objects from 3D model data, usually layer by layer" [3, 4].

*email: adrianbeznea@hotmail.com, victorita_stefanescu@yahoo.com

One of the advantages of AM is the printing of fully functional parts. Choice of material is often related to the part strength. The mechanical properties of 3D printed parts should meet the service loading and, also, must be comparable with parts produced by traditional manufacturing techniques - machined parts, for metal 3D printing or injection moulding thermoplastic [5, 6]. Most metal AM processes create parts with poor surface finish, usually no more than 15 μm Rz and very often considerably reduced. Machine finishing is necessary as a post-process [5]. Thermoplastic 3D printing can achieve good quality surfaces [7].

From the specialized literature information regarding the test results for effect of various printing parameters such as: layer thickness, raster angle, build orientations, fill pattern, printing directions, infill rates and infill patterns air gap and model build temperature, made in laboratory conditions, for standard test sample on part strength are available [5, 6, 8-11].

Dudescu tested the influence of the raster orientation and of the infill pattern and the results indicate a Young's modulus corresponding to the parts with infill percentage from 982 MPa at 20% to 1503 MPa at 100%, for ABS. The influence of the raster orientation for test parts with 100% infill rate have a constant value around 1500 MPa [6].

From experimental research Ahmed determined the flexural strength for ABS test sample and obtained 31.50 MPa Ultimate Flexural Stress at a loading of 58 daN and a Deflection at Ultimate Load of 5.96 mm [11].

Wu determine experimentally that the value for the elastic limit for ABS obtained was 22.9 MPa and the tensile strength for ABS was 27.1 MPa. The tensile properties of 3D-printed ABS test samples were lower than test samples obtained by injection-moulding by 26.2% for the elastic limit and by 26.8% for the tensile strength. The bending strength of ABS determined was 48.6 MPa. The 3D-printed ABS test samples had bending strength and bending modulus reduced by up to 8.2% and 20.8%, respectively, compared with those obtained by injection-moulding [8].

2. Materials and methods

In order to analyze the behaviour of the 3D printed gripper jaws, based on the presented previous research, jaw from a De-sta-co gripper model De-sta-co 84A3-3300AAAA was 3D printed, Figure 1.

Based on the versatility of the printing process the jaw was designed to clamp a can of soft drink.

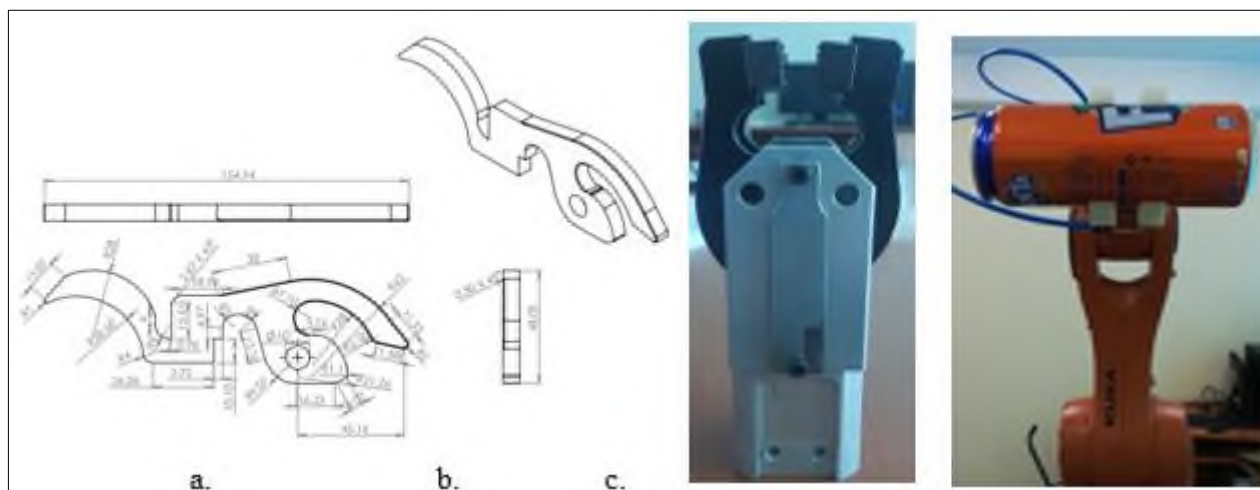


Figure 1. a. View of the 3D printed gripper jaw, b. De-sta-co gripper, c. view of the clamped soda can

In the experiments ABS plus P-430-Acrylonitrile-Butadiene-Styrene production-grade thermoplastic was used to 3D print the gripper soft jaws. The mechanical properties of the ABS plus P-430 thermoplastic are presented in Table 1, [12].

Table 1. Main Mechanical Properties for ABS plus P-430 thermoplastic [12]

Mechanical Properties	Value
Tensile Strength, Yield	26 MPa
Tensile Modulus	2,180 MPa
Tensile Elongation at Break	2%
Flexural Strength	48 MPa
Flexural Modulus	1,760 MPa
Rockwell Hardness	109.5 HRC

The pre-processing of the STL model was realized in the 3D printer Insight command software for selecting the appropriate printing parameters. A view of the tool paths used for 3D printing is presented in Figure 2.

The printer used is Stratasys Fortus 250 mc, that uses Fused Deposition Modelling (FDM) technology to build parts from the bottom up with precisely deposited layers of modelling and support material, with the following features: ABS plus P-430 – production-grade thermoplastic and soluble support material, build envelope - 254 x 254 x 305 mm, three layer thicknesses 0.178, 0.254 and 0.330 mm.



Figure 2. View of the tool paths used for 3D printing

Printing parameters were selected according to the recommendation from specialty literature and considering the machine maximum possibilities: 1. parts slicing (on z axis): 0.254mm; 2. visible surface raster: 0.3556 mm; 3. internal raster: 0.3556 mm; 4. raster angle: 0; 5. part raster width: 0.3556, 6 part interior style solid.

After printing the jaws in accordance with the printing parameters mentioned above, the jaws were mounted in a test stand that simulated the loading of one in the gripper.

The acting force is measured with the force transducer and simulates the effect of the clamped part. The elastic deformation was measured by using and displacement transducer.

The measuring equipment presented in Figure 3 consists of: force transducer S9 5kN produced by Hottinger Baldwin Messtechnik; inductive displacement transducer type W1/10mm -10 mm stroke, produced by Hottinger Baldwin Messtechnik; Spider 8 multi-channel electronic PC measurement unit produced by Hottinger Baldwin Messtechnik; computer.

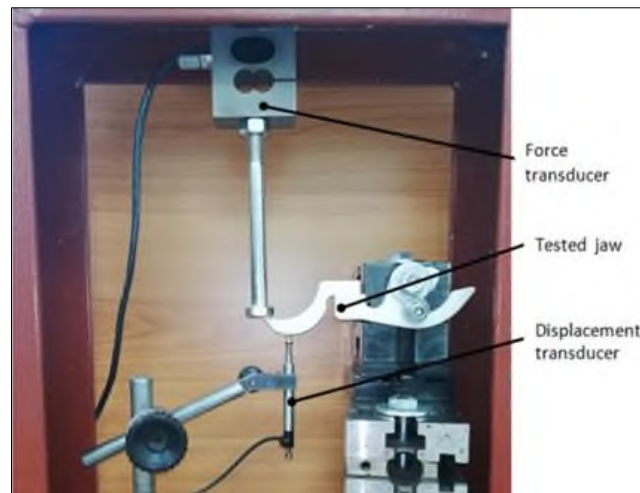


Figure 3. Test stand

3. Results and discussions

Figure 4 shows the hysteresis behaviour (force F versus deformation d evolution) during three successive cycles of gripper jaw loading/unloading, with three consecutive elastic mechanical hysteresis loops characterized by relative high deformations.

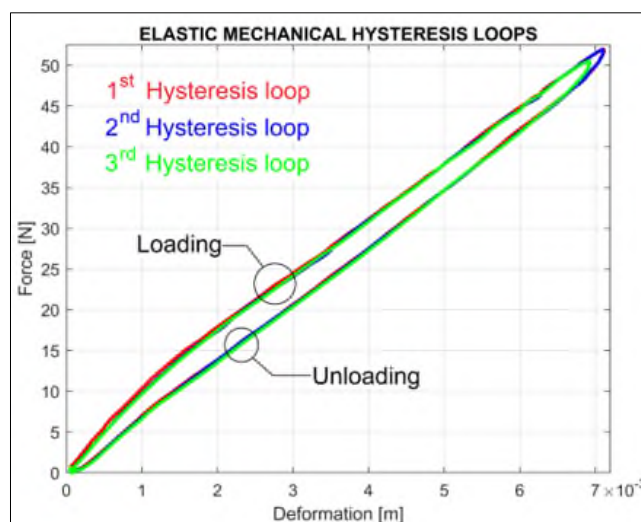


Figure 4. The description of mechanical hysteresis loops for the 3D printed gripper jaw

It is obvious that there are big similarities between these loops (shape and size). The analysis of each hysteresis loop produces some interesting results.

Figure 5 shows the first mechanical elastic hysteresis loop during an experimental loading/unloading cycle with a force range: $0 \div 52$ N and a deformation range: $0 \div 7.12$ mm.

First important experimental information available here is the area of hysteresis loop ($0.02285 \text{ N}\cdot\text{m}$). This area is exactly the amount of mechanical energy - E_l lost during a cycle, dissipated because the internal friction ($E_l = 0.02285 \text{ N}\cdot\text{m}$). The input mechanical energy - E_i during the loading process used for deformation (calculated as the area between the red curve and horizontal line - hl on Figure 5, $E_i = 0.197795 \text{ N}\cdot\text{m}$) is bigger than the output mechanical energy - E_o delivered by the gripper jaw during unloading process (calculated as the area between the blue curve and horizontal line hl on Figure 5, $E_o = 0.174941 \text{ N}\cdot\text{m}$). The difference between these two energies is evidently the lost mechanical energy E_l as $E_l = E_i - E_o$. Both areas (energies) were calculated here by numerical integration.

The energy E_l can be a cumulative characterization of the behaviour of material and the gripper jaw shape during a loading/unloading cycle. We propose two more appropriate characterizations:

-The ratio between the energy E_l and the variation of force (the amount of mechanical energy lost per unit of force, $E_{lf}=4.455 \cdot 10^{-4} \text{ Nm/N}$), with meter as measurement unit.

The ratio between the energy E_l and the variation of deformation (the amount of mechanical energy lost per unit of deformation, $E_{ld}=3.2207 \text{ Nm/m}$), with Newton as measurement unit.

Thus E_{lf} does not depend by applied force and E_{ld} does not depend by deformation.

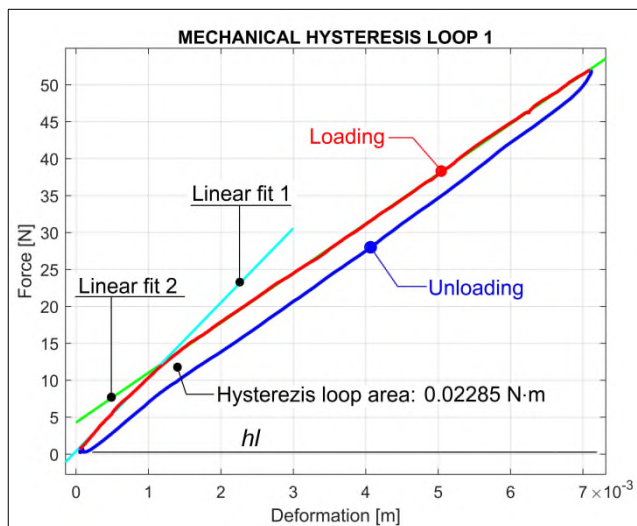


Figure 5. The description of first mechanical hysteresis loop ($E_{lf}=4.455 \cdot 10^{-4} \text{ Nm/N}$, $E_{ld}=3.2207 \text{ Nm/m}$, $k_1=10032.7 \text{ N/m}$, $k_2=6734.5 \text{ N/m}$)

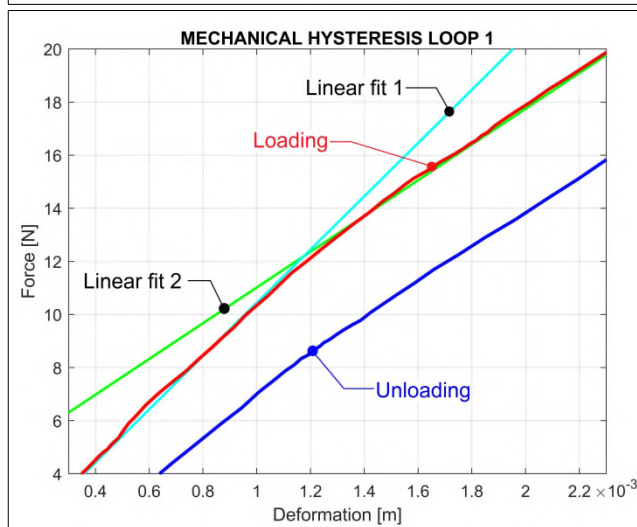


Figure 6. A zoom-in detail on Figure 2 (in the area of fitting line intersection)

Second important experimental information on Figure 5 is the average bending stiffness of the gripper jaw (depending by material type, material structure, shape and loading) as the slope of the line which produces the best approximation (by computer assisted linear curve fitting, or by least square regression as well) of the evolution of force versus deformation, during loading process.

It is interesting that the loading cycle can be easily approximated with two lines by curve fitting (as Figures 5 and 6 indicate). First line, from linear fit 1 (for a loading range $0 \div 12 \text{ N}$) is defined (with the slope-intercept formula $F=k_1d+F_{01}$ of fitting line) by:

$$F=10032.7 \cdot d+0.406 \quad (1)$$

Second line, from linear fit 2 (for loading bigger than 12 N) is defined (with the slope-intercept formula $F=k_2d+F_{02}$) by:

$$F=6734.5 \cdot d+4.281 \quad (2)$$

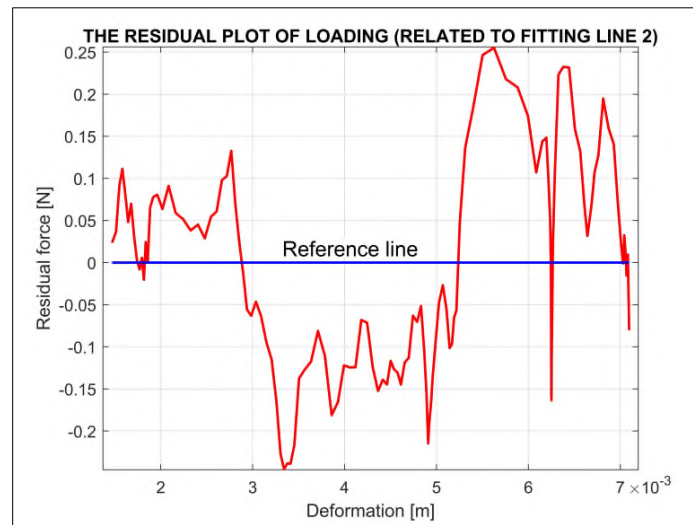


Figure 7. The residual plot of loading curve from Figure 2 related to fitting line 2 (± 0.25 N)

This means that -with a good approximation- the gripper jaw has two value of stiffness: $k_1=10032.7$ N/m (for a loading smaller than 12 N) and $k_2=6734.5$ N/m for a loading bigger than 12 N. The intercept of first linear fit (the intersection of first fitting line with y-axis) is the remnant force $F_{01}=0.406$ N. The intercept of second linear fit (the intersection of second fitting line with y-axis) is the remnant force $F_{02}=4.281$ N.

It is also interesting to underline the value of the ratio $E_{ld}/E_{ld}=7229.56$ N/m: it has the same measurement unit as the stiffness and is relative close by k_2 value.

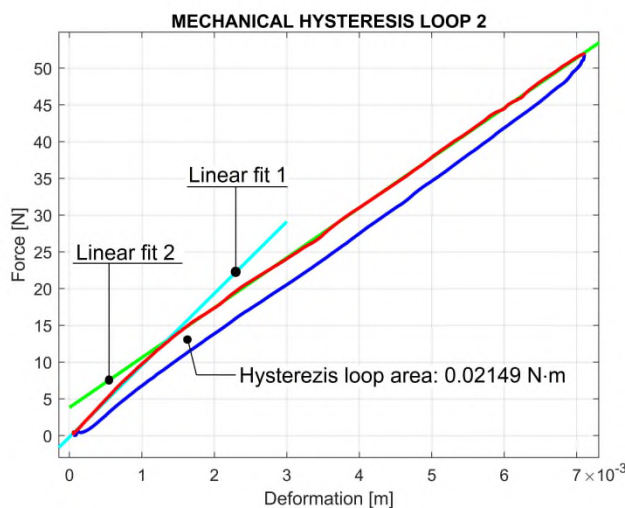


Figure 8. The description of second mechanical hysteresis loop ($E_{lf}=4.161 \cdot 10^{-4}$ Nm/N, $E_{ld}=3.0250$ Nm/m, $k_1=9771.3$ N/m, $k_2=6793.0$ N/m)

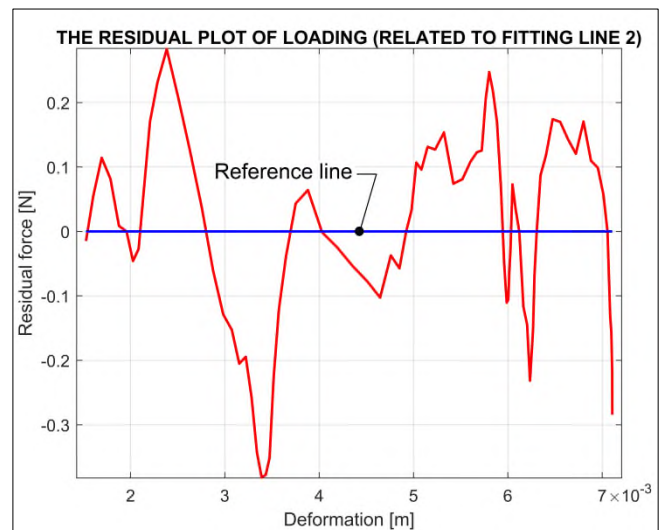


Figure 9. The residual plot of loading curve from Figure 5 related to fitting line 2

It is obvious that the evolution of loading related to linear fit 2 on Figure 5, and the residual plot of loading curve from Figure 7 too (here the reference line depicts the line from linear fit 2) proves a good linearity (with the variation of residual force of ± 0.25 N).

An analysis of the other two hysteresis loops from Figure 4 produces similar results. Figure 8 describes the second hysteresis loop and fitting lines, Figure 9 describes the residual plot of Figure 8.

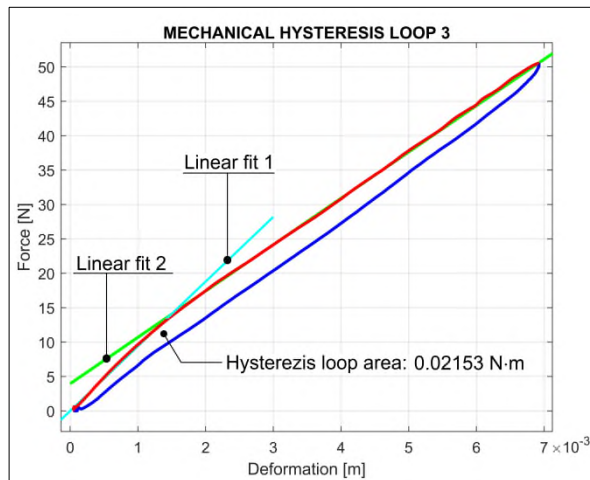


Figure 10. The description of third mechanical hysteresis loop ($E_{lf}=4.277 \cdot 10^{-4} \text{ Nm/N}$, $E_{ld}=3.1105 \text{ Nm/m}$, $k_1=9398.8 \text{ N/m}$, $k_2=6774.9 \text{ N/m}$)

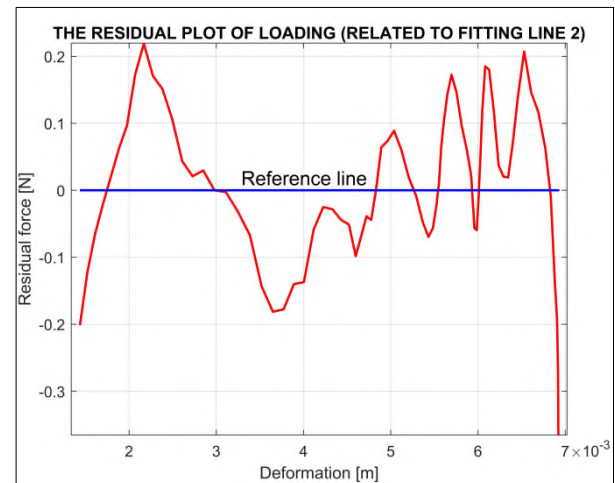


Figure 11. The residual plot of loading curve from Figure 7 related to fitting line 2

Figure 10 describes the second hysteresis loop and fitting lines, Figure 11 describes the residual plot of Figure 10.

The main experimental results for each mechanical hysteresis loop are described in Table 2.

Table 2. Main experimental results for each mechanical hysteresis loop

Loop #	k_1 [N/m]	k_2 [N/m]	E_l [N·m]	E_{lf} [m]	E_{ld} [N]	E_{ld}/E_{lf} [N/m]	$r=(E_{ld}/E_{lf})/k_2$ []
#1	10032.7	6734.5	0.02285	$4.455 \cdot 10^{-4}$	3.2207	7229.56	1.0735
#2	9771.3	6793.0	0.02149	$4.161 \cdot 10^{-4}$	3.0250	7269.01	1.0700
#3	9398.8	6774.9	0.02153	$4.277 \cdot 10^{-4}$	3.1105	7297.41	1.0732
Average	9734.2	6767.4		$4.297 \cdot 10^{-4}$	3.1187	7265.32	1.0722

There are two important observations in Table 2:

-There are relative small variations of the stiffness k_2 . The average value of bending stiffness $k_2(6767.4 \text{ N/m})$ should be considered as the best option in gripper jaw behaviour characterization.

-There are also relative small variations of the ratio E_{ld}/E_{lf} . As it proved in the last column from Table 2, this ratio seems to be strictly related by the bending stiffness k_2 (here with average value of the dimensionless ratio $r=(E_{ld}/E_{lf})/k_2=1.0722$). The value of the ratio E_{ld}/E_{lf} (having the same unit of measurement as bending stiffness k_2) seems to be a type of stiffness involved in gripper jaw characterization(or any other mechanical part tested in the same way). A future approach will be focused on this topic. Also the signification of the ratio r will be privileged in a future research.

In order to characterize the behaviour of the 3D printed gripper jaws a finite element analysis was performed, considering the experimental input force values of 52N and the experimental used measuring scheme.

The definition of ABSplus-P430 material, used by the Stratsys 250 mc printer, in the ANSYS software, a generic acrylonitrile butadiene styrene (ABS) material, from the information database, was selected and the values for ABSplus-P430 were introduced, the main difference was the values of Young module 2200 MPa [12], and flexural modulus is 1.6 GPa.

The loading scheme is presented in Figure 12. The areas represented in blue represent Fixed Support

(or recess), and the force of 52 N. was applied at the top of the part in the direction given by the blue arrow (according to the experiment).

Figure 13 presents the Equivalent Stress (Von Mises) distribution for a modulus of 1.5 GPa.

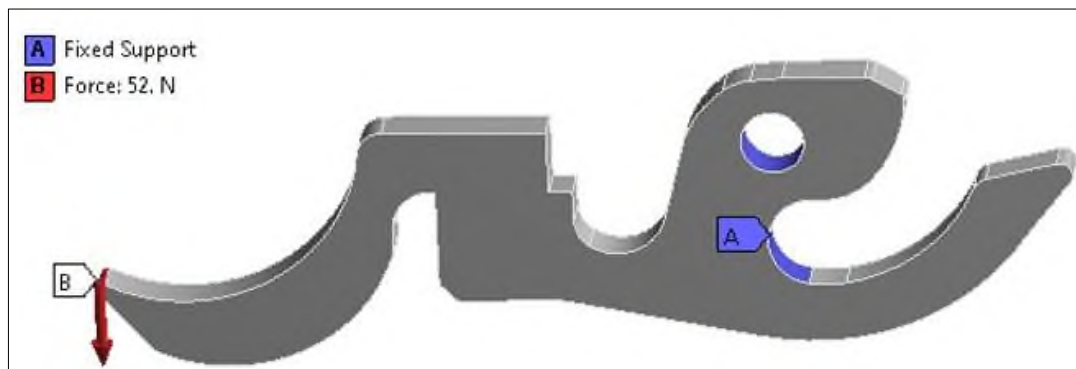


Figure 12. FEA loading and support

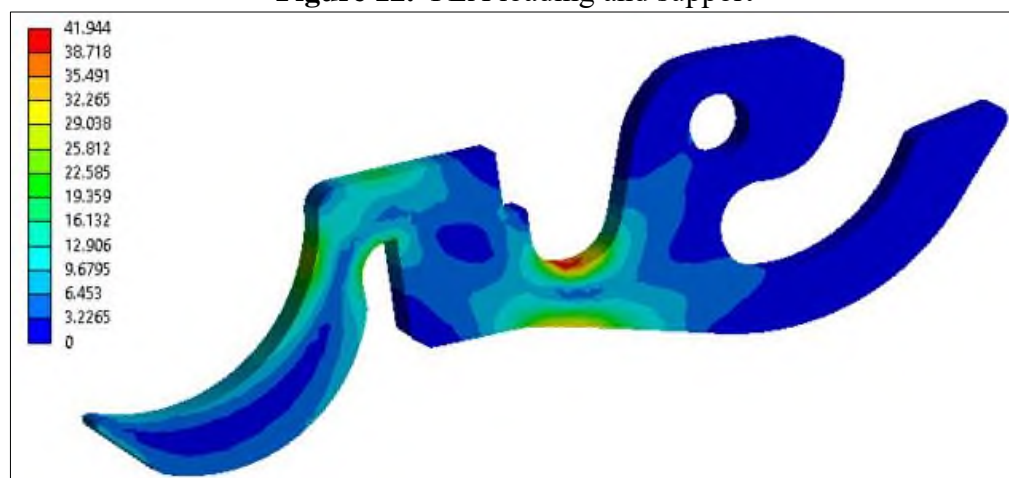


Figure 13. Equivalent Stress (Von Mises) distribution

From the current research the printing parameters have a large impact on the mechanical properties of the 3D printed parts. From the current research the mechanical properties of the 3D printed parts are usually lower by 15-26% from the manufacturer datasheet specification of the material [6, 9, 10, 11]. According to Stratasys the 3D printed prototype has up to 80% of the strength of injection moulded ABS material [12].

Considering the current research on the mechanical properties of the materials FDM, several finite element analysis were done by varying Young modulus in accordance with the experimental results presented in the literature - 1.5 GPa, 1.57 GPa, 1.6 GPa, 1.7 GPa, 1.8 GPa, 2 GPa, 2.15 GPa.

Figure 14 presents FEA displacement results in the measuring area.



Figure 14. FEA displacement results in the measuring area for a modulus of 1.8 GPa

The FEA results for 52N load and variation of Young module are presented in Figure 15. The FEA value that is the closest to the experimental values is corresponding to a Young modulus of 1.8 GPa, resulting a deformation of 7.11 mm.

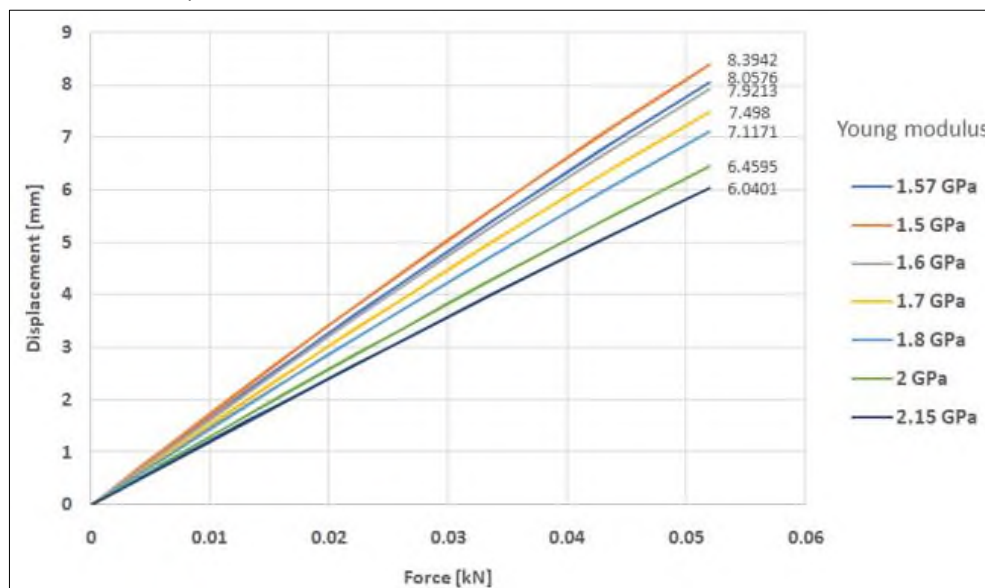


Figure 15. Evolution of deformations (stiffness) for the gripper jaw, considering different Young module, for 0.052 kN load

4. Conclusions

The paper presents the measured values for displacement of 3D printed gripper jaws – soft jaws, considering normal working conditions of type of parts. In the performed experiment a modified jaw, in order to clamp a soda can, was 3D printed with 100% infill, from a De-sta-co gripper model De-sta-co 84A3-3300AAAA.

Several loading – unloading cycles were made and the stiffness value was determined. An analysis of the hysteresis loops indicate that loading cycle can be easily approximated with two lines by curve fitting and two values of the stiffness can be calculated, thus proving a nonlinear behaviour of the 3D printed jaws. The area of the hysteresis cycle between the loading curve and the unloading curve represents the mechanical work not recovered from the system.

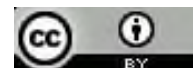
A finite element analysis was performed considering the experimental loading and support conditions and the Young modulus was varies considering the values proposed in the literature between 1.5 GPa to 2.15 GPa. The values for displacement that are closer to the experimental values are corresponding to a value of 1.8 GPa for Young modulus, value that is 18 % lower that Young modulus for a part obtained by injection moulding.

Printing parameters can be selected in order to maximize the mechanical properties of the parts, but when working with complex parts the distribution of loads and stress varies during the work process. For complex parts FEA is a fast and reliable method for determining the strain and stress but in order to safely design and simulate the behaviour of 3D printed parts, lower values for Young modulus must be considered. From the specialized literature and perform experiments, Young modulus for 3D printed parts when designing a complex parts with complex working conditions, should be 20 - 25% lower that the injection moulding.

Acknowledgments: This work was accomplished with the support of COMPETE project nr. 9PFE/2018, funded by the Romanian Government

References

1. BOYES, W., (ed.), *Handbook of Jig and Fixture Design*, Dearborn, Michigan, SME, 1989.



2. POPESCU, A., ENCIU, G., DOBRESCU, T., PASCU, N.E., Experimental Research Using the 3D Printing Technology with Plastic Materials for Prehension Systems Jaws, *Mater. Plast.*, **55**(1), 2018, 20-23., DOI: [10.37358/MP.18.1.4955](https://doi.org/10.37358/MP.18.1.4955).
3. LIM, S., BUSWELL, R.A., LE, T.T., AUSTIN, S.A., GIBB, A.G.F., THORPE, T., Developments in construction-scale additive manufacturing processes, *Automation in Construction*, 21 (1), 2012, pp. 262-268.
4. HUANG, Y., MING, M., JYOTI, D., Additive Manufacturing: Current State, Future Potential, Gaps and Needs, and Recommendations. *Journal of Manufacturing Science and Engineering*, 137, 2015, <https://doi.org/10.1115/1.4028725>.
5. VANEKER, T., BERNARD, A., MORONI, G., GIBSON, I., ZHANG, Y., Design for additive manufacturing: Framework and methodology, *CIRP Annals*, 2020, ISSN 0007-8506, <https://doi.org/10.1016/j.cirp.2020.05.006>
6. DUDESCU, C., RACZ, L., Effects of Raster Orientation, Infill Rate and Infill Pattern on the Mechanical Properties of 3D Printed Materials. *ACTA Universitatis Cibiniensis*, 69, 2017, <https://doi.org/10.1515/aucts-2017-0004>.
7. CHITARIU, D., F., MUNTEANU, A., Research on 3D printed fixture components, MATEC Web of Conferences 178, 02008, 2018 <https://doi.org/10.1051/mateconf/201817802008>,
8. WU, W.; GENG, P.; LI, G.; ZHAO, D.; ZHANG, H.; ZHAO, J. Influence of Layer Thickness and Raster Angle on the Mechanical Properties of 3D-Printed PEEK and a Comparative Mechanical Study between PEEK and ABS, *Materials*, 2015, 8, 5834-5846, <https://doi.org/10.3390/ma8095271>.
9. ZIEMIAN, C., SHARMA, M., ZIEMIAN, S., Anisotropic Mechanical Properties of ABS Parts Fabricated by Fused Deposition Modelling, *Mechanical Engineering*, Murat Gokcek, IntechOpen, DOI: 10.5772/34233. Available from: <https://www.intechopen.com/books/mechanical-engineering/anisotropic-mechanical-properties-of-abs-parts-fabricated-by-fused-deposition-modeling>.
10. ABEYKOON, C. et al. Optimization of fused deposition modelling parameters for improved PLA and ABS 3D printed structures, *International Journal of Lightweight Materials and Manufacture*, 3, 2020, pp. 284-297, <https://doi.org/10.1016/j.ijlmm.2020.03.003>.
11. AHMED, M., I., VANHOOSE M., HEWAVITHARANA, J., STANICH L., HOSSAIN, A., (2016). Comparisons of Bending Stiffness of 3D Printed Samples of Different Materials. <https://doi.org/10.1115/IMECE2016-65119>.
12. ***ABS plus p-430 Datasheet Available online <https://support.stratasys.com/en/materials/fdm-materials/absplus-p430>, (accessed on 11.06.2020)

Manuscript received: 22.11.2020

Article

Research on Additive Technique Parameter Optimization for Robotic Gripper Construction

Emilian Paduraru, Catalin-Gabriel Dumitras , Dragos-Florin Chitariu * , Mihaita Horodincea and Florin Chifan

Faculty of Machines Manufacturing and Industrial Management, Gheorghe Asachi Technical University of Iasi, 700050 Iasi, Romania; emilian.paduraru@academic.tuiasi.ro (E.P.); catalin-gabriel.dumitras@academic.tuiasi.ro (C.-G.D.)

* Correspondence: dragos-florin.chitariu@academic.tuiasi.ro

Abstract: Designing an industrial robot gripper suitable for today's industry is a challenging task due to the rapid evolution of products. Industrial robots are involved in machining, the transfer of parts, control and assembly, and the number of tasks performed by robots are increasing. Robots need to have the capability to adapt to new jobs consisting of new parts and new trajectories, and in most cases the preferred end effectors are grippers. In turn, grippers need to be flexible enough in order to cope with these changes. For this research, the authors propose a new gripper design which is capable of handling a large variety of parts with different sizes and shapes. In this research, an electrically actuated four-jaw gripper, with the capability of parallel movement of its jaws, is presented that also has the capability to fold the clamping jaws two by two and become a two-jaw gripper. Since the design is most suitable for additive manufacturing techniques, different additive techniques are analyzed for the manufacturing of the gripper. In the second part of the paper, different setups of the 3D printers are considered, such as infill percentage, raster angle and layer height. The main material on focus is a PET with grinded carbon-fiber reinforcement, but different materials are used for a better comparison of the rigidity of the system. This comparison is also presented in this article. The analysis of the material and 3D printing parameters are tested with Standard D638-14 probes used in a traction testing machine. After performing the traction test, the results are compared with FEA analysis. An optimal solution based on the experimental tests is proposed for the manufacture of the proposed gripper design.

Keywords: gripper; additive techniques; carbon-fiber material; industrial robot gripper; finite element analysis; traction testing



Citation: Paduraru, E.; Dumitras, C.-G.; Chitariu, D.-F.; Horodincea, M.; Chifan, F. Research on Additive Technique Parameter Optimization for Robotic Gripper Construction. *Machines* **2023**, *11*, 621. <https://doi.org/10.3390/machines11060621>

Academic Editor: Raul D. S.

G. Campilho

Received: 28 April 2023

Revised: 18 May 2023

Accepted: 29 May 2023

Published: 4 June 2023



Copyright: © 2023 by the authors. Licensee MDPI, Basel, Switzerland. This article is an open access article distributed under the terms and conditions of the Creative Commons Attribution (CC BY) license (<https://creativecommons.org/licenses/by/4.0/>).

1. Introduction

Due to fast progress in technology, the manufacturing process in all domains is becoming more and more automated. With the increased requirements for productivity and recent developments in cobots' ease of programming, industrial robots and cobots are becoming a reality in many manufacturing fields. Regardless of the job they have to perform, all robots require an end effector in order to accomplish their purpose. These end effectors are used in various applications, such as welding, cutting, spray-painting, pick-and-place operation, inspection, assembly, 3D printing, and so on. This paper only covers the grasping/ clamping systems, also known as grippers. All of these grippers need to handle a huge variety of objects with different shapes, dimensions and weights.

Prehension mechanisms are complex mechatronic structures used by industrial robots to perform clamping operations of parts in order to handle, transfer or assemble parts within a robotic technological process [1], and are situated at the end of the robotic arm, as shown in Figure 1.

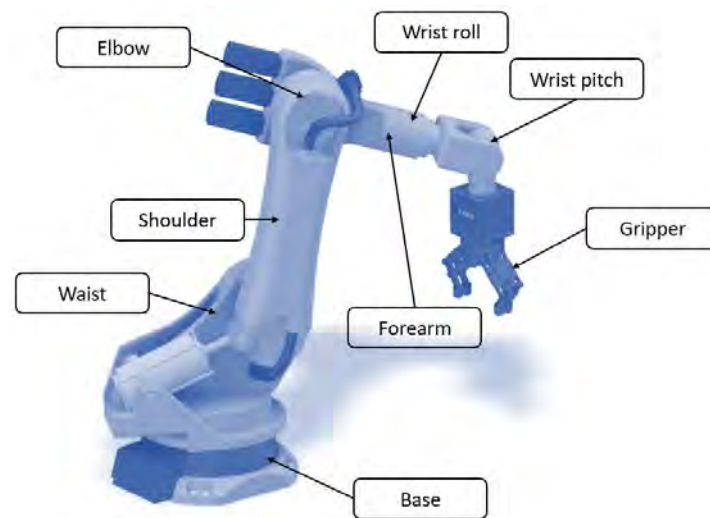


Figure 1. Main parts of an industrial robot.

The ability to grip and manipulate a variety of objects has been the main point in the advancement of robots [2–5].

Considering the large number of requirements, diverse workpieces, and the desire for a well-adapted and reliable gripping mechanism, various grippers have been developed and applied in many automatic applications. Prehension mechanisms can be divided into different categories according to different classification criteria. These criteria refer to the type of actuation, grip modes, number of jaws/fingers, etc. [6,7].

Another challenge in gripping designs is the inertia forces due to the high-speed movement of the robot arm [8–10]. These inertial forces affect power consumption and make the system harder to stop on precise points. To decrease these effects, the gripper system needs to be compact or to use different materials to lower the weight [11,12].

One of the most easily available methods to reduce weight is to change the material used for gripper construction. For this purpose, in this research a composite material was used and tested for the construction of the newly developed gripper. To ease the manufacturing process, additive technology was used.

There are different 3D-printing technologies, such as Stereolithography (SLA), Selective Laser Sintering (SLS), PolyJet, Digital Light Process (DLP), Multi Jet Fusion (MJF), Fused Deposition Modeling (FDM), Direct Metal Laser Sintering (DMLS), Electron Beam Melting (EBM), and so on, that can print with a large variety of materials [13].

The base principle of the 3D printing/additive technologies remains the same in all printing methods, namely, construction of the part layer by layer. This technology is more and more widely used for the manufacturing of unique parts and even the series production of parts in many production fields such as agriculture, automotive, aerospace, medicine, etc. [14–16].

2. Materials and Methods

2.1. New Robot Gripper Solution

In this paper, a new gripper design is proposed by the authors, the design being based on a proprietary patent application. The main advantage of the new proposed design is the high level of configurability, with the gripper being able to grab/clamp, hold and manipulate a large variety of parts with different sizes and shapes, from the interior or from the exterior. The 3D model of this design is shown in Figure 2. There is a very large number of constructive solutions. This is due to the complex shapes of the parts to be handled. Starting from finding a technical solution, we tried to capture several solutions in one. This was the basis for finding this solution. The gripping system was electrically

actuated and was based on a four-jaw /finger parallel open-close action, which ensures a larger area of contact between the parts and system.



Figure 2. Proposed gripper design by authors.

What is different about this gripper is its ability to transform from a four-finger mechanism into a two-finger one by introducing a secondary electric motor for the folding operation of the jaws, as shown in Figure 3.

The operating principle of the mechanism is presented in Figure 4, which shows the two electric motors that are inside the system. The main motor (labelled with 1 in Figure 4) is used for opening/unclamping and closing/clamping of the jaw fingers, ensuring the grasping of the parts. A detailed view of the principle is presented in Figure 5, which is a section view of the system. The movement of the fingers is ensured by a pinion-rack mechanism.

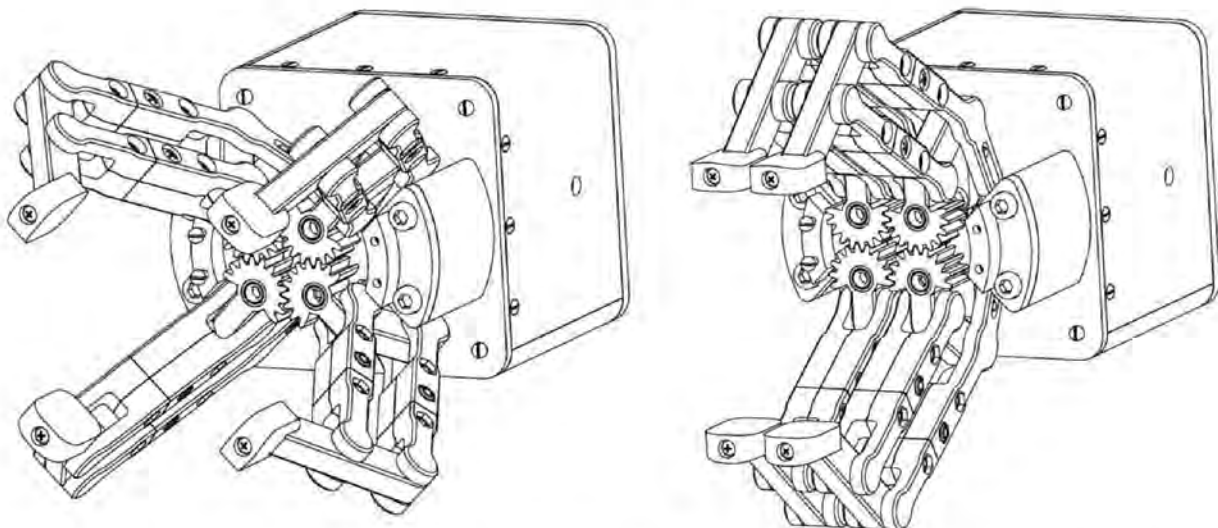


Figure 3. The folding mode of the fingers (four jaw fingers—left, and two-jaw finger configuration—right).



Figure 4. The electrical drive part of the gripper (1—main electric motor, 2—second electric motor).

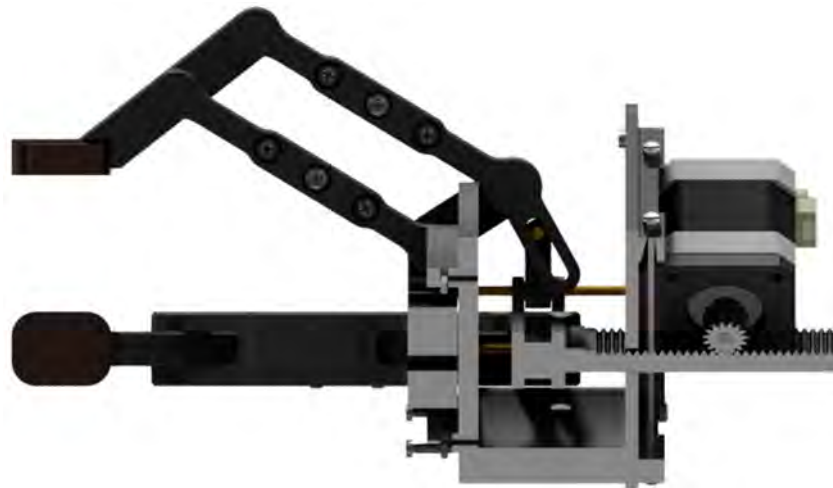


Figure 5. Section view of the mechanism.

The second electric motor (labelled with 2 in Figure 4) allows the conversion from a four-finger to a two-finger grip, and vice versa. This motor displaces a rod that contains a gear segment, which engages with a gear segment mounted on the lower part of the jaw and can directly actuate the jaw.

The maximum dimension of a part that can be handled is 150 mm for the current gripper design. Overall dimensions of the gripper are 250 mm width by 250 mm length when open and in a 4-finger configuration (or 110×250 in a 2-finger configuration); and 300 mm height when the fingers are closed or 255 mm when open.

2.2. The 3D-Printing Methods

To obtain the physical model additive manufacturing was used, or 3D printing more specifically. The one used for this research was FDM. An FDM 3D printer works by depositing molten filament material over a build platform layer by layer until the parts are completed. FDM uses digital design files that are loaded onto the machine and translates them into physical dimensions. Materials for FDM include polymers such as ABS, PLA, PETG and PEI, which the machine feeds as wires through a heated nozzle [16]. The principle of the printing head of this type of 3D printing is presented in Figure 6.

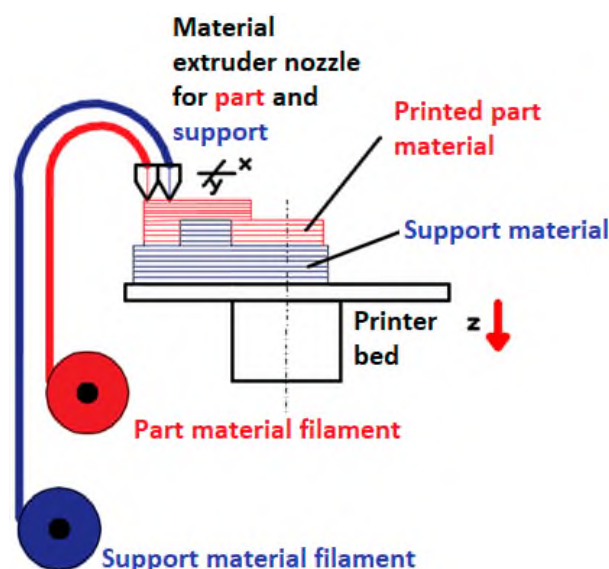


Figure 6. The working principle of the print head using the FDM method.

2.3. Carbon Fiber Materials

In addition to the materials listed above, the 3D printers can use special materials such as composite materials. The material used for testing is a PET CF15, a polyethylene terephthalate reinforced with 15% carbon fiber [17].

There are studies for the printability of the composite materials using additive manufacturing [18–21].

The main categories of fiber-reinforced composites are:

- Composites with a polymer matrix: Usually thermoset (epoxy, polyester or polyimide) or thermoplastic resins reinforced with carbon, glass, boron or aramid fibers (Kevlar), with ceramic monocrystals (or more recently with metal fibers). They are used especially in applications where the working temperatures are relatively low (for thermoplastics manufactured by injection, they can reach a maximum temperature of 400 °C) [22].
- Composites with a metal matrix: Most frequently based on aluminum, magnesium, titanium or copper alloys, in which carbon (graphite), boron or ceramic (alumina or silicon carbide) fibers are introduced. The working temperature (often at most 800 °C) is limited by the melting or softening point level that characterizes the matrix material. The disadvantage is the high specific weight, leading to an increase in the massiveness of the final assembly [22].
- Composites with a ceramic matrix: Developed for applications with very high working temperatures (over 1000 °C); the most used basic materials are silicon carbide (SiC), alumina (Al₂O₃) and glass, and the most used reinforcing fibers are also of a ceramic nature (usually in the form of discontinuous, very short fibers) [22].
- “Carbon-carbon” composites: They are composed of carbon or graphite matrices and reinforced with fibers or fabrics of graphite fibers; they are very expensive, but also superior to other materials due to their resistance to high temperatures (up to 3000 °C), along with their low density and low coefficient of thermal expansion. The most common fiber-reinforced composites are carbon fiber, glass fiber and Kevlar [22].

Another more general classification of composite materials is based on the simultaneous use of two criteria: the geometrical particularities of the complementary material and its orientation in the matrix [23].

Analyzing Figure 7, the material used in this paper is Composite material → Reinforcement type → Fiber-reinforcement → Short → Random.

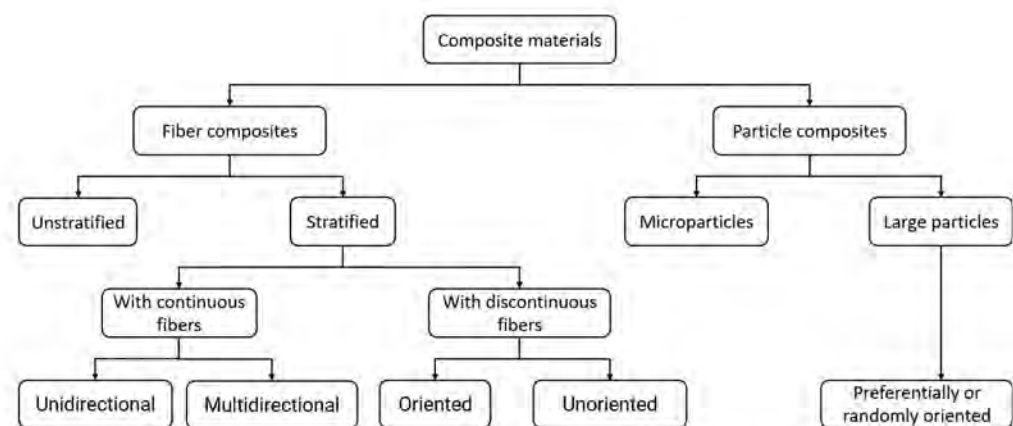


Figure 7. Classification of composite materials based on reinforcement and matrix types.

2.4. Testing Probes

For testing, 3D-printed tensile test specimens were made from different materials (Figure 8).

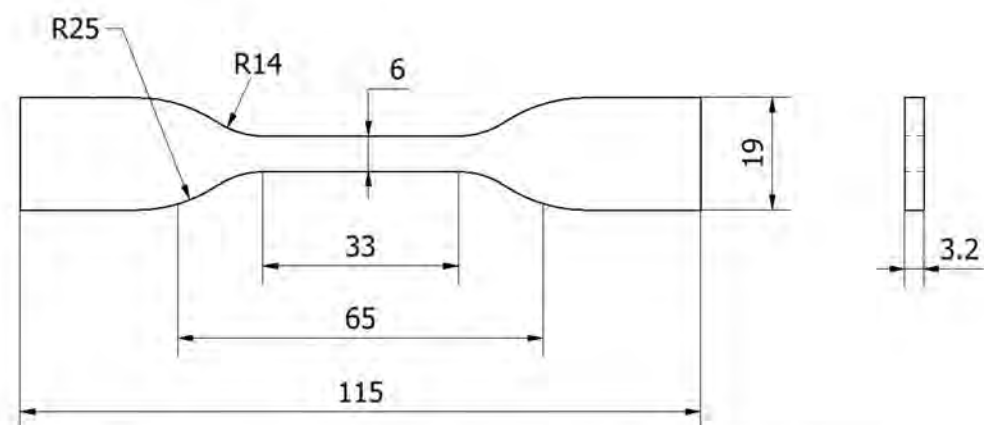


Figure 8. Types of specimens and their dimensions used in own experiments according to standard.

The tensile specimens/tests were made using standard D638-14 [24]. Several types and sizes of specimens are shown in Figure 8. It should be noted that type IV samples were used for this work. The dimensions indicated on the drawing are indicated by letters because the dimensions may vary from one type of specimen to another depending on the thickness of the specimen. The dimensions corresponding to the letters in the figure can be found in standard [24] and the thicknesses of the samples are indicated in the first row of the table.

Knowing the specimen dimensions, the next step is to provide the 3D printer with some parameters. Three types of parameters were considered, each with 2 values:

- Infill percentage:
 - 60% (Figure 9);
 - 100% (Figure 10);
- Layer thickness:
 - 0.17 mm (Figure 11);
 - 0.33 mm (Figure 12);
- Raster angle:
 - 45° (Figure 13);
 - 90° (Figure 14).

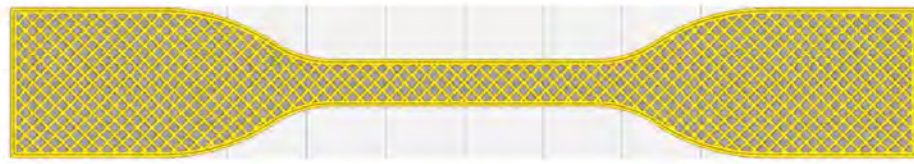


Figure 9. A 60% infill percentage 3D-printed specimen.



Figure 10. A 100% infill percentage 3D-printed specimen.



Figure 11. A 45° raster angle 3D-printed specimen.

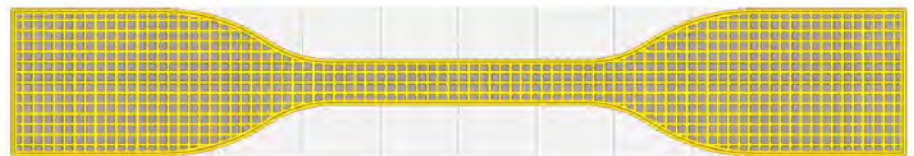


Figure 12. A 90° raster angle 3D-printed specimen.



Figure 13. A 0.17 mm layer thickness 3D-printed specimen.



Figure 14. A 0.33 mm layer thickness 3D-printed specimen.

Using these parameters, a factorial experiment was performed which had 2 levels and 3 factors, more specifically 2^3 , totaling 8 possible combinations as shown in Table 1.

Table 1. Combinations of printing parameters.

Run	Infill Percentage (%)	Layer Thickness (mm)	Raster Angle (°)
1	60	0.33	90
2	60	0.17	45
3	100	0.33	45
4	60	0.33	45
5	100	0.17	90
6	100	0.17	45
7	100	0.33	90
8	60	0.17	90

For a more conclusive result, three copies were made for each of these eight types of specimens. Therefore, a total of 24 specimens were printed with carbon fiber reinforcement PETG.

Furthermore, for a comparison with classic 3D printing material, PLA and ABS P430 materials with exactly the same printing properties were used, resulting a total of 72 specimens to test.

These are the parameters that we tested, but there are numerous articles that combine different printing parameters or technologies with various types of materials to optimize the strength of the parts [25–29].

For testing the specimen, a traction testing machine (Lloyd Instruments LRX Plus) was used to determine the force-displacement curve. In order for the test to meet the test standard, the distance between the two grippers of the traction device was set to 65 mm and the test speed was 5 mm/min at room temperature.

The machine was connected to a computer which used Nexigen Plus software v 3.0 to collect and process the results.

The setup for the specimen-traction machine-computer is presented in Figure 15: the 3D-printed test specimen (1) is clamped between the testing machine jaws (2) (the lower one is fixed and the upper one pulls up at a constant speed); also indicated are the machine (3) and the monitor (4) where the results are shown in the form of graphs. Figure 16 shows a print screen image from one of the specimen test.

**Figure 15.** Experimental testing setup for specimens.

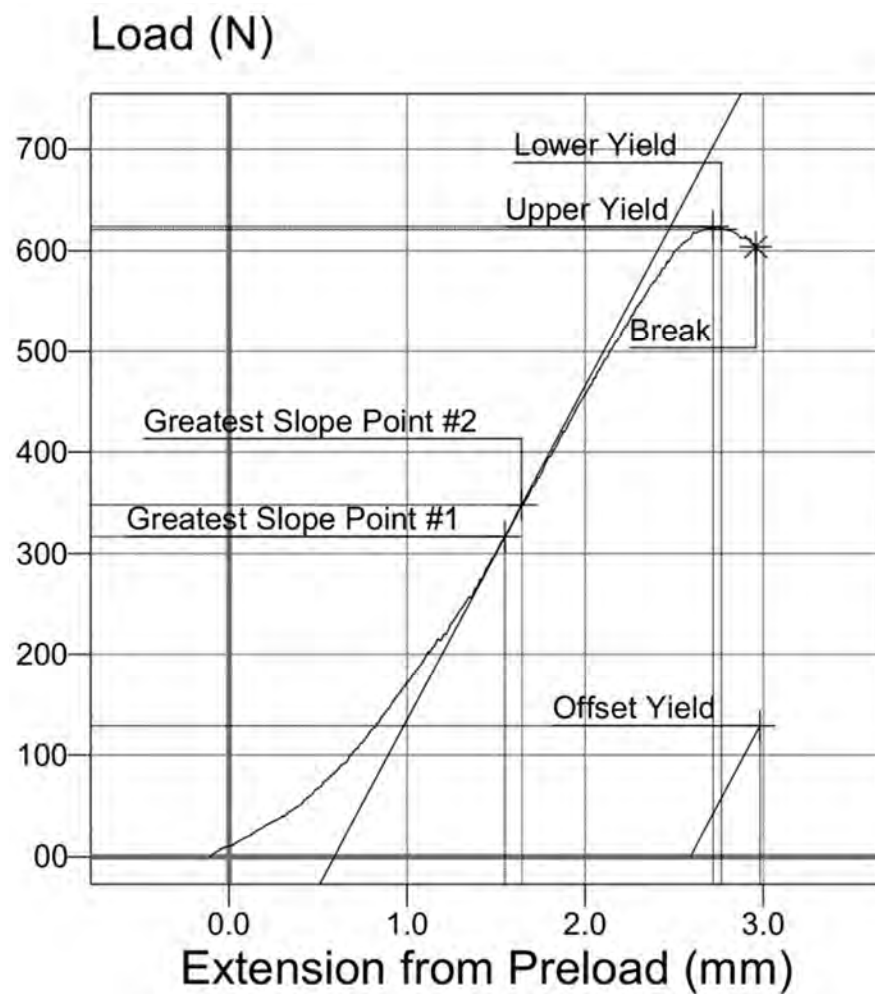


Figure 16. Print screen of a force-displacement graph for a specimen.

3. Results

3.1. Results of the Specimen Testing

All 72 specimens were tested and the force-displacement curves were extracted. Knowing the force acting on the samples and their dimensions, with the help of Relation 1, stress (σ), expressed in MPa, can be determined. Additionally, with the help of Relation 2 and the displacements made by the traction machine, strain (ϵ) can be determined for each specimen, expressed in mm/mm.

$$\sigma = F/A \quad (1)$$

$$\epsilon = \Delta L/L \quad (2)$$

Figure 17 shows the average results after specimen tests from the PET CF material. For example: 1PET CF is an average stress–strain curve of all three copies of specimens with the same print parameters (60% infill, 0.33 mm layer thickness and 90° raster angle). The numbers (from 1 to 8) represent the type of printing parameters which correspond with the column “Run” from Table 1.

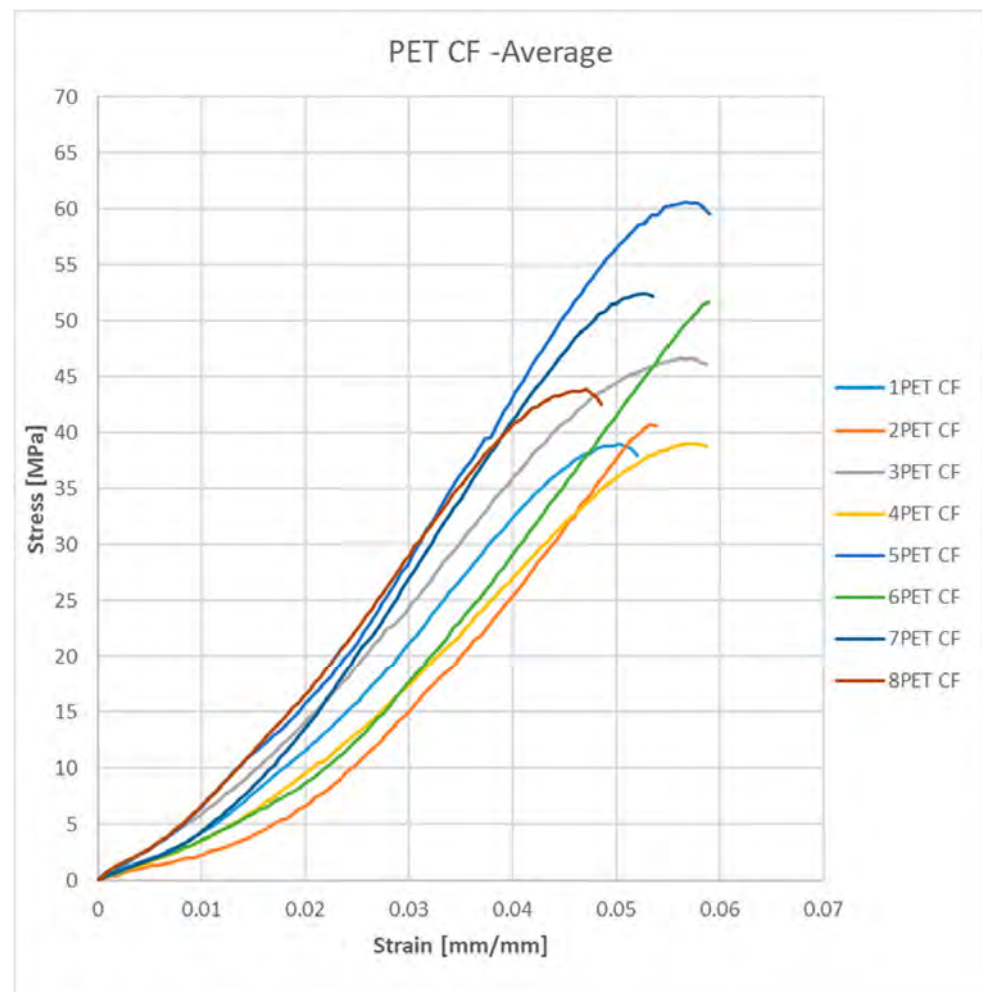


Figure 17. The averages of the 8 types of parameters for the PET CF material.

Table 2 presents the printing parameters for the PET CF test probe and the experimental results regarding Yield points (elastic limits).

Table 2. Yield points for PET CF materials.

Run	Infill Percentage (%)	Layer Thickness (mm)	Raster Angle (°)	Yield (MPa)
1	60	0.33	90	36.99
2	60	0.17	45	39.40
3	100	0.33	45	43.04
4	60	0.33	45	37.09
5	100	0.17	90	59.45
6	100	0.17	45	50.75
7	100	0.33	90	49.41
8	60	0.17	90	42.18

Figure 18 shows the average stress–strain curves of the average results for the PLA material. The numbering is the same as the material above.

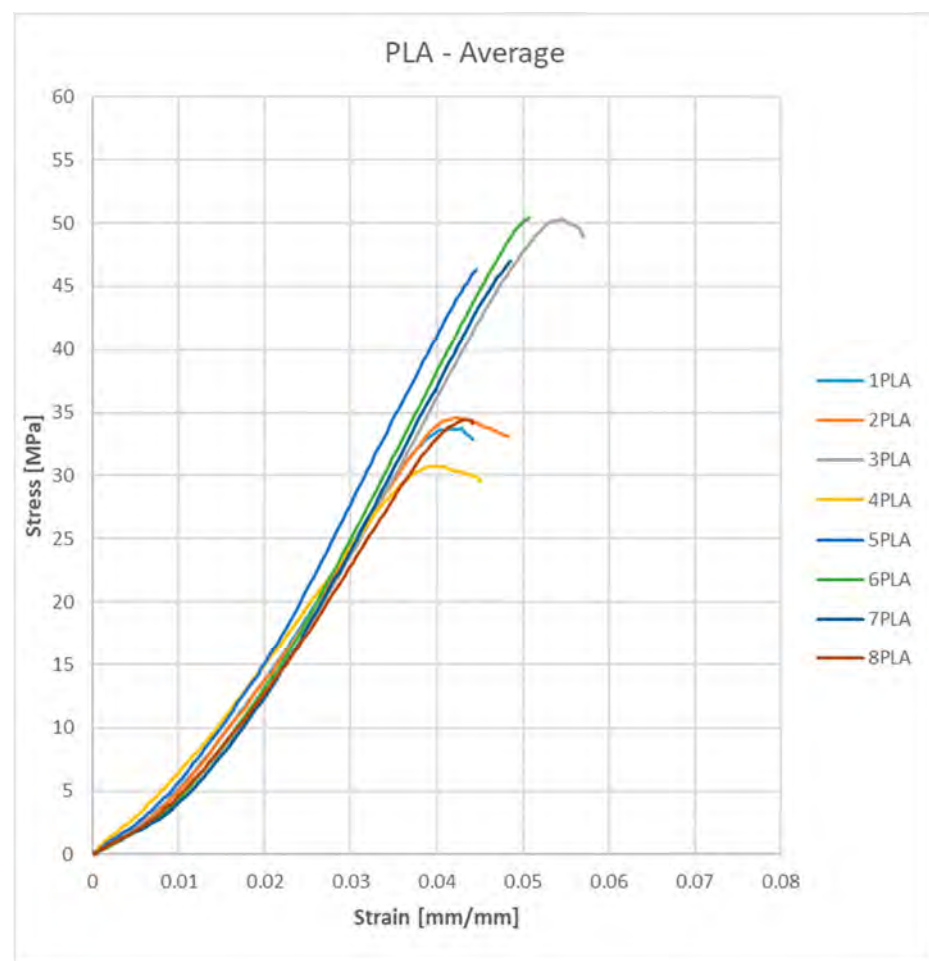


Figure 18. The averages of the 8 types of parameters for the PLA material.

Table 3 presents the printing parameters for the PLA test probe and the experimental results regarding Yield points (elastic limits).

Table 3. Yield points for PLA materials.

Run	Infill Percentage (%)	Layer Thickness (mm)	Raster Angle (°)	Yield (MPa)
1	60	0.33	90	32.46
2	60	0.17	45	33.41
3	100	0.33	45	49.48
4	60	0.33	45	29.72
5	100	0.17	90	46.33
6	100	0.17	45	49.99
7	100	0.33	90	46.65
8	60	0.17	90	33.32

Figure 19 shows the average stress–strain curves of the average results for the ABS material. The numbering is also the same as the material above.

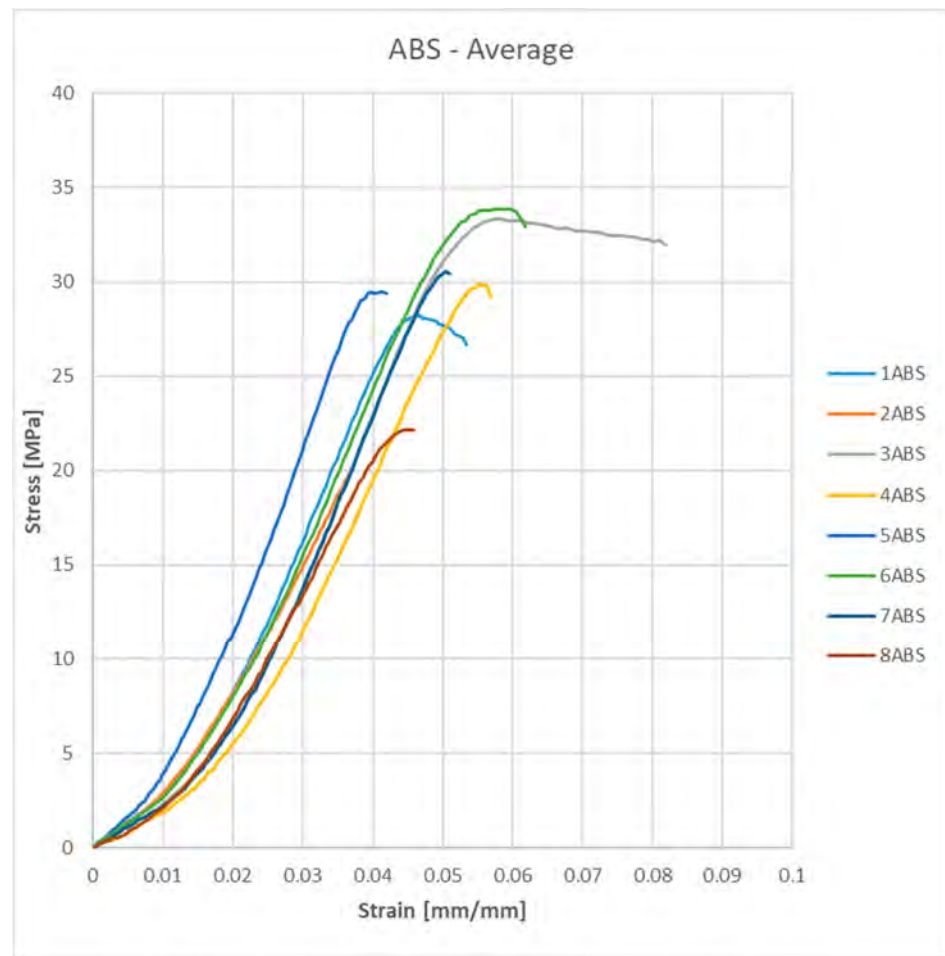


Figure 19. The averages of the 8 types of parameters for the ABS material.

Table 4 presents the printing parameters for the ABS test probe and the experimental results regarding Yield points (elastic limits).

Table 4. Yield points for ABS material.

Run	Infill Percentage (%)	Layer Thickness (mm)	Raster Angle (°)	Yield (MPa)
1	60	0.33	90	32.46
2	60	0.17	45	33.41
3	100	0.33	45	49.48
4	60	0.33	45	29.72
5	100	0.17	90	46.33
6	100	0.17	45	49.99
7	100	0.33	90	46.65
8	60	0.17	90	33.32

In Figure 20 the differences between “the best” stress–strain curves for each material (PET CF, PLA, ABS) are presented.

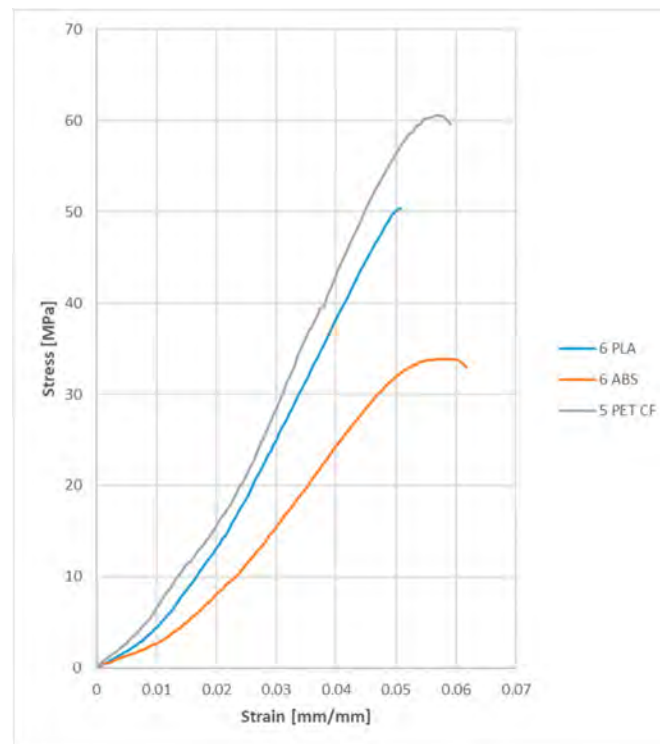


Figure 20. The difference between the main curves of the 3 materials.

It can be observed that the material with carbon fiber reinforcement is slightly more rigid, with a higher yield point and also a higher breaking point than the other two.

The regression equations to determine the yield point of materials are shown below (Equation (3) for PET, Equation (4) for PLA and Equation (5) for ABS):

$$\text{Yield CF} = 24.50 + 0.2937 \times \text{Infill percentage} - 39.5 \times \text{Layers thickness} + 0.0986 \times \text{Raster angle} \quad (3)$$

$$\text{Yield PLA} = 11.69 + 0.3971 \times \text{Infill percentage} - 7.41 \times \text{Layers thickness} - 0.0213 \times \text{Raster angle} \quad (4)$$

$$\text{Yield ABS} = 9.61 + 0.1584 \times \text{Infill percentage} + 20.7 \times \text{Layers thickness} - 0.0186 \times \text{Raster angle} \quad (5)$$

Regression equations are used to describe the relationship between the response and the terms in the model. The regression equation is an algebraic representation of the regression line [30].

Table 5 points out how well the model fits our data.

Table 5. Results on model accuracy for the experimental data.

Material	S	R-sq	R-sq (adj)	R-sq (pred)
PET	2.98968	91.70%	85.48%	66.81%
PLA	1.93605	97.14%	95.00%	88.56%
ABS	3.24945	71.04%	49.32%	0.00%

S is used to assess how well the model describes the response. S is measured in the units of the response variable and represents how far the data values fall from the fitted values. The lower the value of S, the better the model describes the response [30].

R-sq is the percentage of variation in the response that is explained by the model. The higher the R² value, the better the model fits the data. R² is always between 0% and 100% [30].

R-sq (pred) is used to determine how well the model predicts the response for new observations [30].

Figure 21 shows a Pareto diagram for the PET with carbon-fiber reinforcement, where the influence of each 3D printing parameter used (infill percentage, layers thickness and raster angle) can be observed. From this diagram, it can be concluded that the infill percentage has the greatest influence on probe test.

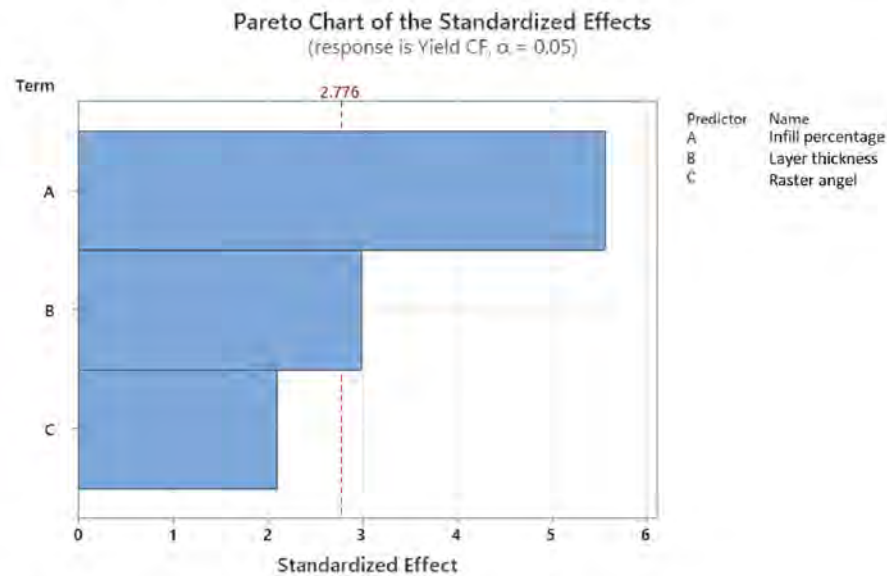


Figure 21. Pareto diagram for PET CF material yield.

Figure 22 shows the main effects for the PET CF material, where the same 3D printing parameters were also introduced. The line connecting the means is interpreted as follows:

- When the line is horizontal (parallel to the x -axis), there is no main effect present. The mean response is the same across all factor levels.
- When the line is not horizontal, there is a main effect present. The mean response is not the same across all factor levels. The steeper the slope of the line, the larger the magnitude of the average effect.

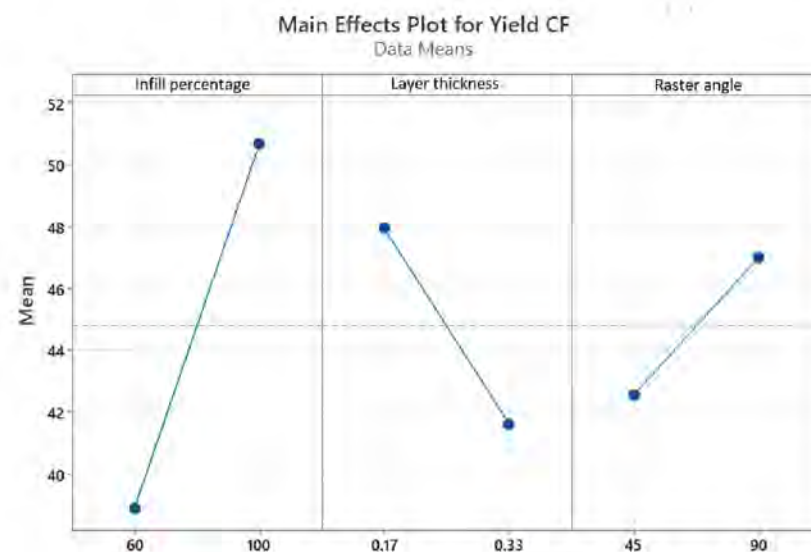


Figure 22. Main effect plot for PET CF material yield.

Figure 23 shows the interaction diagram. This diagram is used to show how the relationship between a categorical factor and a continuous response depends on the value of the second categorical factor. This graph shows the means for the levels of one factor on the x -axis and a separate line for each level of another factor. To understand how the interactions affect the relationship between the factors and the response, the lines should be evaluated as follows:

- Parallel lines—no interaction takes place;
- Non-parallel lines—an interaction occurs. The more non-parallel the lines, the stronger the interaction.

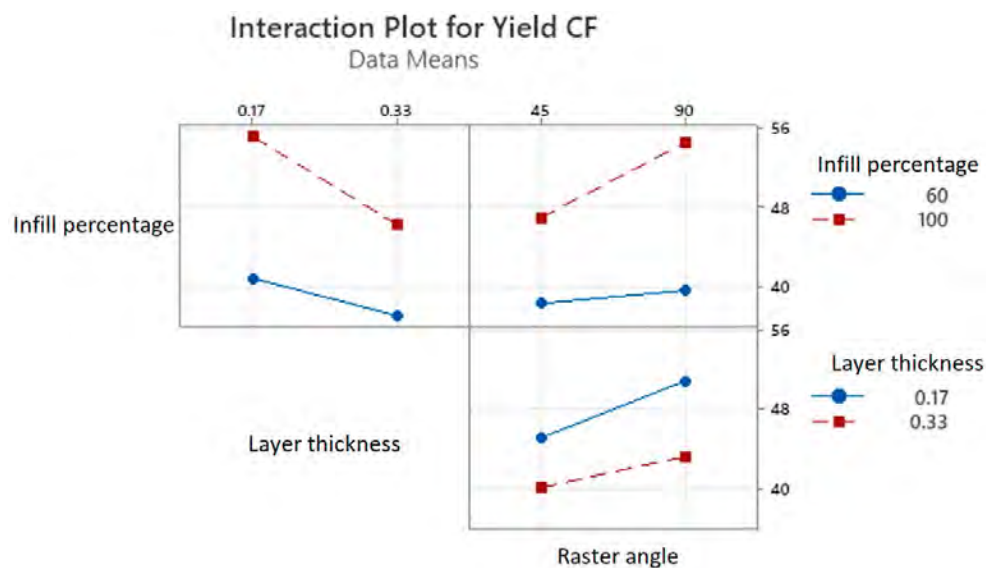


Figure 23. Interaction plot for PET CF material yield.

3.2. Finite Element Analysis Calibration of the Specimens

For material curve definition for finite element analysis programs, such as Ansys, the obtained curves were processed to be able to define the material as correctly as possible. Thus, the three material curves, the most resistant from a mechanical point of view, were defined, one for each individual material, as specified in Figure 20.

A random material with random properties from all 24 was chosen to be studied and analyzed using finite element analysis. Furthermore, the ABS material with a 100% infill percentage, 0.17 mm layers thickness and 90° raster angle was considered (5ABS). The stress–strain curve was processed to obtain a curve that is suitable for the finite element analysis software, initially for the 5ABS material and then for all three types of materials. The stress–strain curve for 5ABS is shown in Figure 24.

To verify the mechanical properties of the defined materials, finite element analysis simulations were performed on the specimens.

The first step was to define the geometry of the specimen. This used the same standardized geometry used to 3D-print them (presented in Figure 9). Figure 25 shows a screenshot of the geometry.

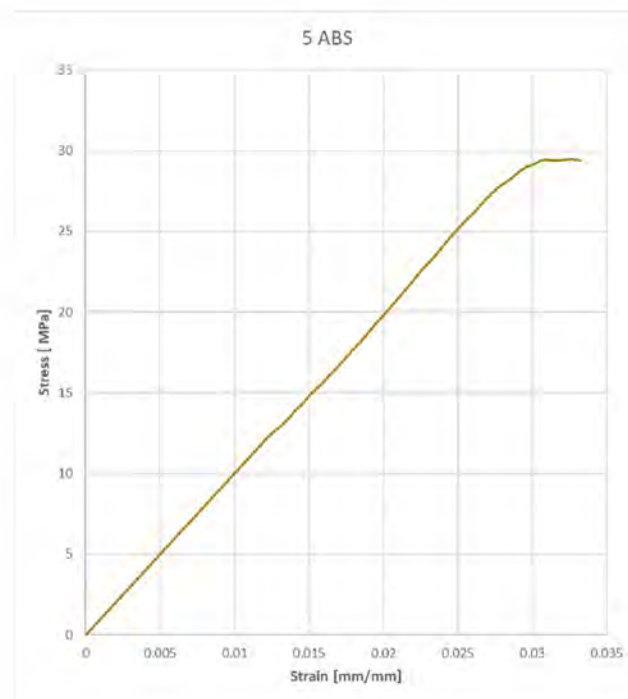


Figure 24. The material curve to be used in the finite element analysis.



Figure 25. Screenshot of the geometry used in finite element analysis.

The model is meshed in small elements, with a total of around 9200 nodes and around 42,000 elements as is shown in Figure 26.

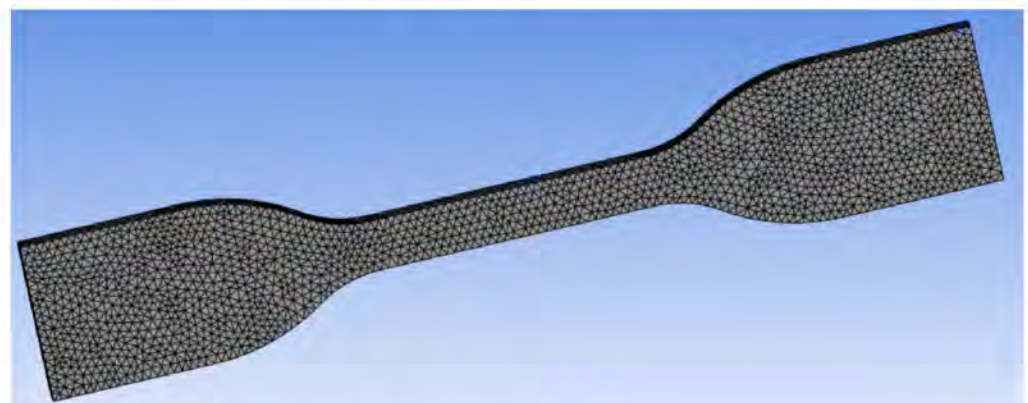


Figure 26. Meshed geometry in finite analysis software.

After meshing the geometry, the mechanical conditions were defined, such as embedding the model in a part (the blue part in Figure 27) that mimics the clamping between the fixed jaws of the testing machine and establishing an x -axis displacement in the opposite end of the model (the yellow part in Figure 27), which imitates the movement of the upper gripper of the test machine.

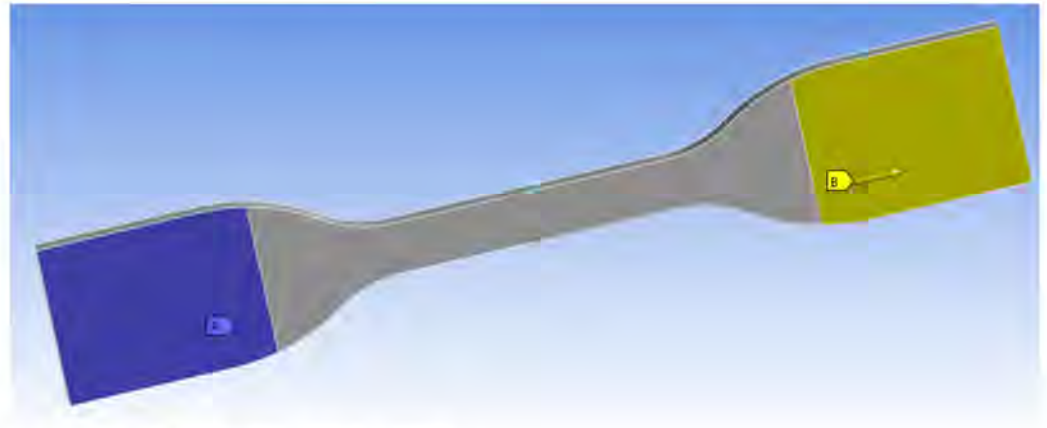


Figure 27. Mechanical condition definition.

It should be noted that the distance between the two conditions (or the distance between the blue-colored part and the yellow-colored part) was 65 mm, according to the standard.

Figure 28 shows the result of the simulation (stress–strain curve) compared to the previously defined material curve (Figure 24).

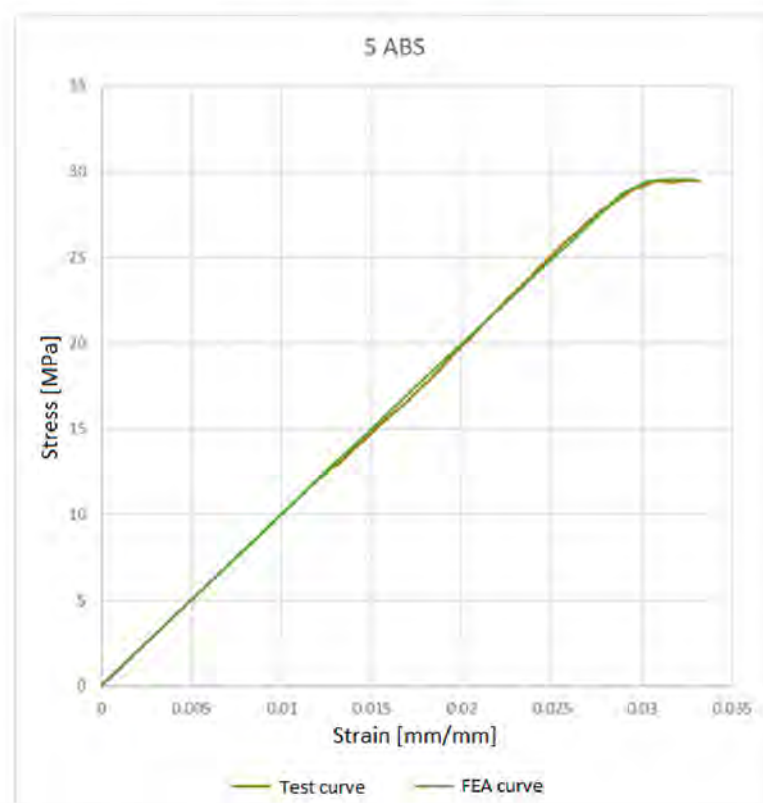


Figure 28. Comparison between the test and simulation curves (stress–strain).

It can be seen that the two overlap, which means that the simulation conforms to the actual specimen test.

The material 5ABS (with a 100% infill percentage, 0.17 mm layers thickness and 90° raster angle were considered) was randomly chosen. For further investigations, this material with the same printing parameters was used to 3D-print one finger of the proposed gripper solution and a finite element analysis was performed with the data obtained in the testing probe (the finger was subjected to mechanical tests).

In Figure 29 (left) is the 5ABS 3D-printed finger, and on the right is the finite element analysis with NON-validated results for the moment (only generic material was used).

If the results from the finite element analysis on the entire finger with the same material definition as the probe above were similar to the real test on the 3D-printed finger, further investigations with other types of material and 3D-printing parameters were made.

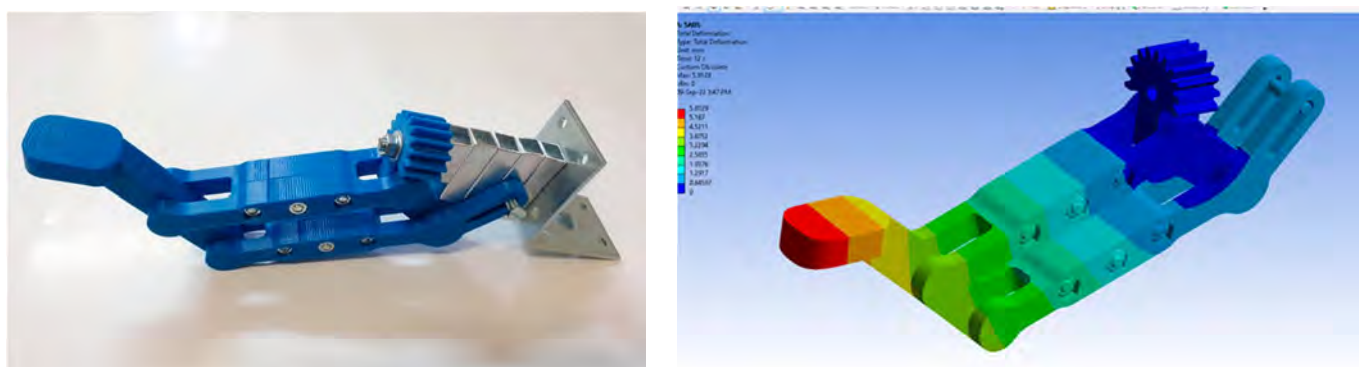


Figure 29. A 3D-printed proposed gripper finger (left) and NON-validated FEA results (right).

4. Discussion

For this research work, a new four-jaw gripper constructive solution was designed, which fulfils the current requirements of the market of flexible manufacturing systems, using a 3D-printing process and composite plastic materials, from the most common ones (such as PLA and ABS), to a more special material with carbon-fiber inserts.

The fact that the current trend of gripper mechanisms is aimed towards finding a constructive solution that can perform multiple tasks, such as grabbing/manipulating parts of different shapes and sizes either for sorting or assembling the components of an assembly, has led to our attempt to find a constructive solution of our own in this research.

3D printing is becoming an increasingly widespread manufacturing process, and the research directions are aimed toward increasing precision and productivity. The types or processes of 3D printing are constantly evolving. Even if some are similar, each printing process has advantages and disadvantages and specific application fields, covering the printing of simple plastic parts on inexpensive 3D printers to the complex metal printing of parts in extremely complex and expensive machines. Obviously, depending on the complexity of the 3D printer and the precision when materializing the parts, the cost of purchasing such a printer or producing the parts is directly proportional to this.

In order to test and accurately rank the 3D-printing materials for intended applications, test parts were printed on different printers according to the D638-14 test standard for geometry of the specimens. The test machine used in own experiments was setup to the standard requirements.

Using physical tests of a tensile-compression testing machine, it was possible to determine material stress–strain curves, which, through transformation calculations, extracted the data needed to define the materials in the finite element analysis software. After defining them, it was possible to perform FEA simulations where the forces, respectively, the internal stresses, were validated in relation to the deformation of the samples.

From a cost perspective, the price ratio is the most favorable for the PLA material; however, this material, unlike PET-CF with carbon fiber inserts, is very susceptible to

moisture and ultraviolet light, thus losing its original properties over time. Even if the cost is much higher for the material with carbon-fiber inserts, it does not pose moisture problems or other disadvantages that PLA presents, and maintains its mechanical properties for a long time. Overall, the most mechanically resistant material is PET with carbon-fiber reinforcement.

5. Conclusions

3Dprinting is a powerful manufacturing process that has the maximum flexibility in terms of the printed parts; almost every geometry designed can be obtained, with good mechanical properties, or good enough for the intended purpose. Considering that grippers are low-volume parts, 3D printing is a very good alternative to the conventional manufactured grippers that are usually CNC-machined and assembled. By using an FEA simulation, small enhancements can be made to the gripper prototype in order to achieve stronger parts or cheaper parts with the same rigidity. In this case, testing of the new parts can be performed in a matter of hours. Additionally, replacement parts for grippers can be printed in a short time, shorter than when completing an order for a conventional parts supplier.

Following the tests carried out, the elastic limit (yield) for carbon-fiber-reinforced PET material was around 19% higher than for the PLA material and 84% higher than for the ABS. Overall, raster angle had a low impact on strength with only 2% (90 degrees was better than a 45-degree angle), and the layer thickness had a slightly bigger impact with 7.2% (0.17 was better than 0.33 mm). The most important factor for the strength of the testing specimens was the infill percentage, which was 42.1% (100% was better than 60% infill).

FEA simulations allow the testing of complex parts in various situations, but without proper knowledge of the material properties, the results have only indicative values. By using physical tests with the tensile-compression testing machine, the real material stress-strain curves were determined for different test samples made from PLA, ABS P430, and PET-CF. Considering the ability of 3D printing to create parts with different properties derived from the printing parameters, the most relevant parameters were selected and used in our own experiments. For each selected parameter, namely infill percentage (%), layer thickness (mm), and raster angle ($^{\circ}$), three relevant values were selected that could also be materialized on the available printers. Test parts were printed respecting D638-14 standard geometry. All 72 specimens were tested and the force-displacement curves were extracted in order to obtain base information for the FEA simulation. FEA can be a powerful instrument in the simulation and validation of various constructive solutions for grippers, in this case. FEA and 3D printing can lead to a shorter time to make a prototype; moreover, 3D printing can be a standalone manufacturing process, albeit in low batches, where grippers are found in terms of production volume. The selection of relevant materials and the durability of the parts manufactured by 3D printing will be a continuous research subject. Currently, with the reduction in the lifespan of products and the increased capabilities of the manufacturing process in machinery manufacturing, 3D-printed parts can be considered satisfactory in terms of durability, which applies to the designed gripper as well.

The experimental data indicate similar behavior for the stress-strain curves of the PET and PLA materials. A better result would be in favor of the PET material. The presented tabular values for the experimental data can be used to fine-tune the FEA simulation in order to improve the accurate description of the behavior of a material.

For further research, we propose to test other composite materials and also more printing parameters to determine their influences on the rigidity of the parts.

Additionally, we will look to reduce the dimensions of the gripper body by replacing the current electric motors with ones of a smaller size but with the same or even greater power.

A different research direction would be to apply all of these material properties on a full-scale gripper mechanism, test it, measure it, and try to simulate those behaviors using finite element analysis software.

6. Patents

Păduraru E., Chitariu D. F., Dumitraș C. G., Horodincă M., Munteanu A., Chifan F., Hrib F. V., Patent Application, Modular Prehension Mechanism, 5734/06.06.2022.

Author Contributions: Conceptualization, E.P. and D.-F.C.; methodology, C.-G.D.; software, C.-G.D. and F.C.; validation, E.P. and D.-F.C.; formal analysis, C.-G.D. and F.C.; investigation, E.P.; resources, C.-G.D.; data curation, M.H. and E.P.; writing—original draft preparation, E.P.; writing—review and editing, E.P., M.H. and D.-F.C.; visualization, C.-G.D. and M.H.; supervision, E.P.; project administration, E.P.; funding acquisition, C.-G.D. All authors have read and agreed to the published version of the manuscript.

Funding: This research received no external funding.

Conflicts of Interest: The authors declare no conflict of interest.

References


1. Khoo, S. *Design and Analysis of Robot Gripper for 10 kg Payload*; Universiti Teknikal Malaysia Melaka: Durian Tunggal, Malaysia, 2008.
2. Hernandez, J.; Sunny, M.S.H.; Sanjuan, J.; Rulik, I.; Zarif, M.I.I.; Ahamed, S.I.; Ahmed, H.U.; Rahman, M.H. Current Designs of Robotic Arm Grippers: A Comprehensive Systematic Review. *Robotics* **2023**, *12*, 5. [\[CrossRef\]](#)
3. Lobbezoo, A.; Kwon, H.-J. Simulated and Real Robotic Reach, Grasp, and Pick-and-Place Using Combined Reinforcement Learning and Traditional Controls. *Robotics* **2023**, *12*, 12. [\[CrossRef\]](#)
4. Lu, Z.; Guo, H.; Zhang, W.; Yu, H. GTac-Gripper: A Reconfigurable Under-Actuated Four-Fingered Robotic Gripper with Tactile Sensing. *IEEE Robot. Autom. Lett.* **2022**, *7*, 7232–7239. [\[CrossRef\]](#)
5. Mathew, A.T.; Hussain, I.; Stefanini, C.; Ben Hmida, I.M.; Renda, F. ReSoft Gripper: A reconfigurable soft gripper with monolithic fingers and differential mechanism for versatile and delicate grasping. In Proceedings of the 2021 IEEE 4th International Conference on Soft Robotics (RoboSoft), New Haven, CT, USA, 12–16 April 2021; pp. 372–378. [\[CrossRef\]](#)
6. Păduraru, E.; Munteanu, A. Adaptive gripper for industrial robots. In Proceedings of the XXVth International Scientific Conference “Inventica 2021”, Iasi, Romania, 23–25 June 2021.
7. Samadikhoshkho, Z.; Zareinia, K.; Janabi-Sharifi, F. A Brief Review on Robotic Grippers Classifications. In Proceedings of the 2019 IEEE Canadian Conference of Electrical and Computer Engineering (CCECE), Edmonton, AB, Canada, 5–8 May 2019; pp. 1–4. [\[CrossRef\]](#)
8. Song, H.; Kim, Y.-S.; Yoon, J.; Yun, S.-H.; Seo, J.; Kim, Y.-J. Development of Low-Inertia High-Stiffness Manipulator LIMS2 for High-Speed Manipulation of Foldable Objects. In Proceedings of the 2018 IEEE/RSJ International Conference on Intelligent Robots and Systems (IROS), Madrid, Spain, 1–5 October 2018; pp. 4145–4151. [\[CrossRef\]](#)
9. Zhang, J.; Lumia, R.; Starr, G.; Wood, J. Sharing inertia load between multiple robots with active compliant grippers using trajectory pre-shaping. In Proceedings of the IEEE International Conference on Robotics and Automation, ICRA 2004, New Orleans, LA, USA, 26 April–1 May 2004; Volume 3, pp. 2574–2581. [\[CrossRef\]](#)
10. Righettini, P.; Strada, R.; Cortinovis, F. Modal Kinematic Analysis of a Parallel Kinematic Robot with Low-Stiffness Transmissions. *Robotics* **2021**, *10*, 132. [\[CrossRef\]](#)
11. Feller, D.; Siemers, C. Mechanical Design and Analysis of a Novel Three-Legged, Compact, Lightweight, Omnidirectional, Serial-Parallel Robot with Compliant Agile Legs. *Robotics* **2022**, *11*, 39. [\[CrossRef\]](#)
12. Yong, S.; Aw, K. Multi-Layered Carbon-Black/Elastomer-Composite-Based Shielded Stretchable Capacitive Sensors for the Underactuated Robotic Hand. *Robotics* **2022**, *11*, 58. [\[CrossRef\]](#)
13. Available online: <https://www.hubs.com/knowledge-base/3d-printing/> (accessed on 12 January 2023).
14. Chitariu, D.F. The FDM 3D Printing Application for Orthopedic Splints. *Bul. Inst. Politeh. Iași Secț. Constr. Mas.* **2015**, *LXI*, 45–54.
15. Chitariu, D.F.; Păduraru, E.; Dogan, G.; İlhan, M.; Negoescu, F.; Dumitraș, C.G.; Horodincă, M. Experimental research on behavior of 3d printed gripper soft jaws. *Rev. Mater. Plast.* **2020**, *57*, 366–375. [\[CrossRef\]](#)
16. Keles, O.; Blevins, C.W.; Bowman, K.J. Effect of build orientation on the mechanical reliability of 3D printed ABS. *Rapid Prototyp. J.* **2017**, *23*, 320–328. [\[CrossRef\]](#)
17. Available online: <https://forward-am.com/material-portfolio/ultrafuse-filaments-for-fused-filaments-fabrication-fff/reinforced-filaments/ultrafuse-pet-cf15/> (accessed on 12 January 2023).
18. Russo, A.C.; Andreassi, G.; Di Girolamo, A.; Pappadà, S.; Buccoliero, G.; Barile, G.; Vegliò, F.; Stornelli, V. FDM 3D Printing of high performance composite materials. In Proceedings of the 2019 II Workshop on Metrology for Industry 4.0 and IoT (MetroInd4.0&IoT), Naples, Italy, 4–6 June 2019; pp. 355–359. [\[CrossRef\]](#)
19. Blanco, I. The Use of Composite Materials in 3D Printing. *J. Compos. Sci.* **2020**, *4*, 42. [\[CrossRef\]](#)
20. Tee, Y.L.; Peng, C.; Pille, P.; Leary, M.; Tran, P. PolyJet 3D Printing of Composite Materials: Experimental and Modelling Approach. *JOM* **2020**, *72*, 1105–1117. [\[CrossRef\]](#)
21. Park, S.; Shou, W.; Makatura, L.; Matusik, W.; Fu, K. 3D printing of polymer composites: Materials, processes, and applications. *Matter* **2022**, *5*, 43–76. [\[CrossRef\]](#)

22. Available online: https://ro.wikipedia.org/wiki/Material_compozit (accessed on 13 January 2023).
23. Priyanka, P.; Dixit, A.; Mali, H. High-Strength Hybrid Textile Composites with Carbon, Kevlar, and E-Glass Fibers for Impact-Resistant Structures. A Review. *Mech. Compos. Mater.* **2017**, *53*, 685–704. [[CrossRef](#)]
24. ASTM D638-14; Standard Test Method for Tensile Properties of Plastics. ASTM International: West Conshohocken, PA, USA, 2014.
25. Decuir, F.; Phelan, K.; Hollins, B.C. Mechanical Strength of 3-D Printed Filaments. In Proceedings of the 2016 32nd Southern Biomedical Engineering Conference (SBEC), Shreveport, LA, USA, 11–13 March 2016; pp. 47–48. [[CrossRef](#)]
26. Shubham, P.; Singh, A.; Kumar, S.; Pandey, S. Thermal effect on Layers of 3D Printed Components & its impact on Material's Property. In Proceedings of the 2022 International Mobile and Embedded Technology Conference (MECON), Noida, India, 10–11 March 2022; pp. 699–703. [[CrossRef](#)]
27. Kung, C.; Kuan, H.-C.; Kuan, C.-F. Evaluation of tensile strength of 3D printed objects with FDM process on RepRap platform. In Proceedings of the 2018 1st IEEE International Conference on Knowledge Innovation and Invention (ICKII), Jeju, Republic of Korea, 23–27 July 2018; pp. 369–372. [[CrossRef](#)]
28. Bürge, G.; Aytac, E.; Evcil, A.; Savaş, M.A. An Investigation on Mechanical Properties of PLA Produced by 3D Printing as an Implant Material. In Proceedings of the 2020 4th International Symposium on Multidisciplinary Studies and Innovative Technologies (ISMSIT), Istanbul, Turkey, 22–24 October 2020; pp. 1–6. [[CrossRef](#)]
29. Ali, M.H.; Yerbolat, G.; Amangeldi, S. Material Optimization Method in 3D Printing. In Proceedings of the 2018 IEEE International Conference on Advanced Manufacturing (ICAM), Yunlin, Taiwan, 16–18 November 2018; pp. 365–368. [[CrossRef](#)]
30. Available online: <https://support.minitab.com> (accessed on 2 March 2023).

Disclaimer/Publisher's Note: The statements, opinions and data contained in all publications are solely those of the individual author(s) and contributor(s) and not of MDPI and/or the editor(s). MDPI and/or the editor(s) disclaim responsibility for any injury to people or property resulting from any ideas, methods, instructions or products referred to in the content.

Article

Condition Monitoring of a Three-Phase AC Asynchronous Motor Based on the Analysis of the Instantaneous Active Electrical Power in No-Load Tests

Dragos-Florin Chitariu, Mihaita Horodincu *, Constantin-Gheorghe Mihai, Neculai-Eduard Bumbu, Catalin Gabriel Dumitras , Neculai-Eugen Seghedin and Florin-Daniel Edutanu

Digital Manufacturing Systems Department, Gheorghe Asachi Technical University of Iasi, 700050 Iasi, Romania; dragos-florin.chitariu@academic.tuiasi.ro (D.-F.C.); constantin-gheorghe.mihai@student.tuiasi.ro (C.-G.M.); neculai-eduard.bumbu@student.tuiasi.ro (N.-E.B.); catalin-gabriel.dumitras@academic.tuiasi.ro (C.G.D.); neculai-eugen.seghedin@academic.tuiasi.ro (N.-E.S.); florin-daniel.edutanu@staff.tuiasi.ro (F.-D.E.)

* Correspondence: mihaita.horodincu@academic.tuiasi.ro

Featured Application: This paper proposes a method of monitoring the condition of three-phase asynchronous induction motors running with no load based on computer analysis of the instantaneous active electrical power.

Abstract: This paper experimentally reveals some of the resources offered by the instantaneous active electric power in describing the state of three-phase AC induction asynchronous electric motors (with a squirrel-cage rotor) operating under no-load conditions. A mechanical power is required to rotate the rotor with no load, and this mechanical power is satisfactorily reflected in the constant and variable part of instantaneous active electric power. The variable part of this electrical power should necessarily have a periodic component with the same period as the period of rotation of the rotor. This paper proposes a procedure for extracting this periodic component description (as a pattern by means of a selective averaging of instantaneous active electrical power) and analysis. The time origin of this pattern is defined by the time of a selected first passage through the origin of an angular marker placed on the rotor, detectable by a proximity sensor (e.g., a laser sensor). The usefulness of the pattern in describing the state of the motor rotor has been demonstrated by several simple experiments, which show that a slight change in the no-load running conditions of the motor (e.g., by placing a dynamically unbalanced mass on the rotor) has clear effects in changing the shape of the pattern.

Keywords: AC induction motor rotor; condition monitoring; instantaneous active electrical power; signal processing; pattern recognition



Citation: Chitariu, D.-F.; Horodincu, M.; Mihai, C.-G.; Bumbu, N.-E.; Dumitras, C.G.; Seghedin, N.-E.; Edutanu, F.-D. Condition Monitoring of a Three-Phase AC Asynchronous Motor Based on the Analysis of the Instantaneous Active Electrical Power in No-Load Tests. *Appl. Sci.* **2024**, *14*, 6124. <https://doi.org/10.3390/app14146124>

Academic Editor: Filipe Soares

Received: 9 June 2024

Revised: 9 July 2024

Accepted: 11 July 2024

Published: 14 July 2024



Copyright: © 2024 by the authors. Licensee MDPI, Basel, Switzerland. This article is an open access article distributed under the terms and conditions of the Creative Commons Attribution (CC BY) license (<https://creativecommons.org/licenses/by/4.0/>).

1. Introduction

The three-phase AC induction asynchronous induction motors (with a squirrel-cage rotor) are currently widely used for driving mechanical systems, mainly due to their simplicity and reliability. Firstly, monitoring the condition of these motors with no load (idling) and detecting possible failure situations that could lead to a catastrophe is a major topic of scientific research. Secondly, understanding the behaviour of these motors allows their design and operation to be optimised.

The signals taken into account when monitoring the condition of motors are among the most diverse. The valuable motor output signals provided by the motor and suitable for condition monitoring are acquired by means of appropriate sensors placed on the motor or on its rotor (most frequently vibration sensors [1–12], temperature sensors [2–6,10,13–18], instantaneous rotation speed sensors [6,9,14,16,18–21], acoustic sensors [5,8,11,12,14] and rarely magnetic field and flux sensors [20,22,23] or stray-flux sensors [6,24]).

The valuable motor input signals are often acquired from the electrical supply system using appropriate instantaneous voltage and current sensors. The most commonly used input signal in motor condition monitoring is the description of the absorbed current (e.g., by Motor Current Signature Analysis, MCSA [8,9,13,14]), which has been widely used in scientific research [2,4,6–9,11,12,14,15,17,18,20,24–35]. The use of voltage sensors is indirect and rarely used on its own, e.g., in unbalancing detection of an AC power supply and overvoltage detection [26], detection of broken bars in stator [13], to prevent phase loss [36] or to describe voltage waveform anomalies [2]). Otherwise, voltage sensors are almost always combined with the use of current sensors to provide other useful information and signals for monitoring, such as the description of the absorbed instantaneous electrical power or active electrical power [13,19,25,34], as the subject of our previous research [21], the detection of the phase or phase shift of the instantaneous current [30,33,37], or the description of the power factor variation over time [6,13,17].

It is important to note that there is a strong correlation between the input signals (related to the absorbed electrical power and its components) and the output signals (generally describing mechanical phenomena), especially in the case of periodic phenomena, conditioned, of course, by the dynamics of the rotor rotating through the rotating magnetic field generated by the stator. The motor acts as an energy (power) transformer from electrical to mechanical form. Many normal and abnormal variable mechanical phenomena (e.g., related to bearing condition [1,2,10,11], rotor mechanical imbalance/eccentricity [10,28]) during motor operation (especially with no load) should be reflected (with an amplitude and the phase at the origin of time depending on the frequency) in the evolution of the current, the power factor and especially the instantaneous (and/or active) electrical power. The motor acts as a mechanical load sensor. The use of signals describing the variation over time of the electrical inputs in the motor offers a major advantage: simplicity of installation and use of the sensors (simple current and voltage transformers), sometimes with the possibility to use wireless data transmission [10,17,26].

There are many processing techniques available for condition monitoring of AC induction motors, most of which are used to extract useful information from variable (mainly periodic) signals. For continuous periodic signals (vibrations, variable part of instantaneous angular speed, currents and, rarely, instantaneous electrical power [34]), the conversion from the time domain to the frequency domain using the Fast Fourier Transform spectrum is widely used [2,6,8,9,17,21,34] to describe the sinusoidal components within (average amplitudes and frequencies). More commonly, the wavelet transform is used to detect and describe short (transient) sequences (based on local spectral information) of components within these signals [2,8,9,13,14,17,18,20,26–28,37–39]. Actually, the use of artificial intelligence techniques (e.g., based on neural networks [2,5,11,13,18,26,38,40], support vector machines [2,13], machine learning algorithms [3,5,8,10,14,29,36], deep learning algorithms [11]) or the use of IoT [16,38] for early detection [1,4,10,14,15,41], possibly online [8,9,17], of motors states that may develop abnormally has become increasingly attractive.

Table 1 briefly summarises the previously discussed topic of bibliographic references from the current state of scientific research in motor condition monitoring.

There is a general opinion in the scientific literature that analysing the variation over time of the instantaneous current absorbed by a phase of an asynchronous three-phase induction motor (particularly with a squirrel-cage rotor) is one of the best ways of monitoring its condition. For incomprehensible reasons (with a few exceptions, e.g., [25,34]), many scientists ignore the fact that there is an electrical input parameter that helps to describe the behaviour of this electric motor running with no load better, more accurately and more completely than the instantaneous current: the instantaneous electrical power (IEP). This IEP is defined as the product of the instantaneous voltage (IV) and the instantaneous current (IC); both (in the case of this motor running with no load) are periodic evolutions whose fundamentals are sinusoidal, time-shifted or phase-shifted. The IEP defines the instantaneous active electrical power (IAEP) absorbed by the motor (partially

converted into mechanical power required to turn the rotor), and the IAEP defines the active electrical energy absorbed by the motor (partially converted into mechanical energy). All the variable electrical and (especially) mechanical phenomena involved in the no-load operation of a three-phase AC induction motor should be mandatory and reflected in the variation over time of the IAEP. If the mechanical load on the rotor increases (e.g., due to a fault of its condition), the amplitude of the fundamental of the IC increases and—very importantly—the phase shift decreases; consequently (by cumulative effect), the IAEP also increases and vice versa. This cumulative effect explains why IEP (and also IAEP) is more suitable than IC for motor condition monitoring. Furthermore, IC alone cannot describe, for example, an operating situation with a negative IAEP flow. This situation occurs when the rotor of this motor is externally mechanically forced to rotate at a speed higher than the synchronous speed or during electrical braking periods. The motor acts as a generator, providing IAEP and active electrical energy.

Table 1. A brief summary of the subject of bibliographical references on the condition monitoring of motors.

Sensors	Output sensors	Vibration	[1–12]
		Temperature	[2–6,10,13–18]
		Instantaneous rotation speed	[6,9,14,16,18–21]
		Acoustic	[5,8,11,12,14]
		Magnetic field	[20,22,23]
	Input sensors	Stray flux	[6,24]
		Instantaneous current	[2,4,6–9,11,12,14,15,17,18,20,24–35]
		Instantaneous voltage	[2,13,26,36]
		Instantaneous (active) electrical power	[13,19,21,25,34]
		Phase shift (power factor)	[6,13,17,30,33,37]
Processing techniques and methods for monitoring		Fast Fourier Transform	[2,6,8,9,17,21,34]
		Wavelet transform	[2,8,9,13,14,17,18,20,26–28,37–39]
		Neural networks	[2,5,11,13,18,26,38,40]
		Machine learning	[3,5,8,10,14,29,36]
		Support vector machine	[2,13]
		Deep learning	[11]
		Vienna monitoring method	[41]
		Early detection	[1,4,10,14,15,41]
		Online	[8,9,17]
		IoT	[16,38]
Detectable failures		Bearing condition	[1–5,7–14,17,22,25,26,32,34,38,39]
		Rotor mechanical imbalance/eccentricity	[4,6,9,10,13–15,17,20,22,28,37,39]
		Broken bars in squirrel-cage rotor	[2,4,7–9,12,14,15,17,22–24,26,30,32,37,39,40]
		Stator winding faults	[5,8,13,14,17,22,27,32,37,39,40]
		Magnetic asymmetries in stator/rotor	[2,22,23]
		Current imbalance	[3,8,9,14,22,28,37]
		Phase loss	[9,36]

When we talk about describing variable mechanical phenomena through the evolution of IEP or IAEP, we must take into account the dynamic aspects (mainly damping and phase-shifting effects) due to the fact that the rotor (with mechanical inertia [19] and developing

dry and viscous friction) is driven in rotation by a rotating magnetic field (with torsional elasticity) generated (electromagnetically) by the stator.

The purpose of this paper is to present some experimental results on IAEP analysis, which are useful in condition monitoring of three-phase AC asynchronous induction motors (with a squirrel-cage rotor) running with no load. It is shown experimentally that in the variation of the variable part of the IAEP over time (numerically described with a high sampling rate), there is a periodic pattern (with the same period as the period of rotation of the rotor) that can be used to describe the state of the rotor (or motor as well). Some results related to the recognition and the analyses of this pattern (the repeatability, the synthetic and analytical description, the influence of different factors on the shape of the pattern, etc.) are presented.

This paper is organised as follows: Section 2 presents the materials and methods, Section 3 presents the experimental results, and Section 4 is reserved for discussions.

2. Materials and Methods

2.1. Experimental Setup

There is a very simple way to obtain the information needed to find the IEP absorbed by a three-phase AC induction asynchronous motor with squirrel-cage rotor, which is based on the considerations shown in Figure 1 (describing a setup partially used previously in [42] and similar to [25,34]).

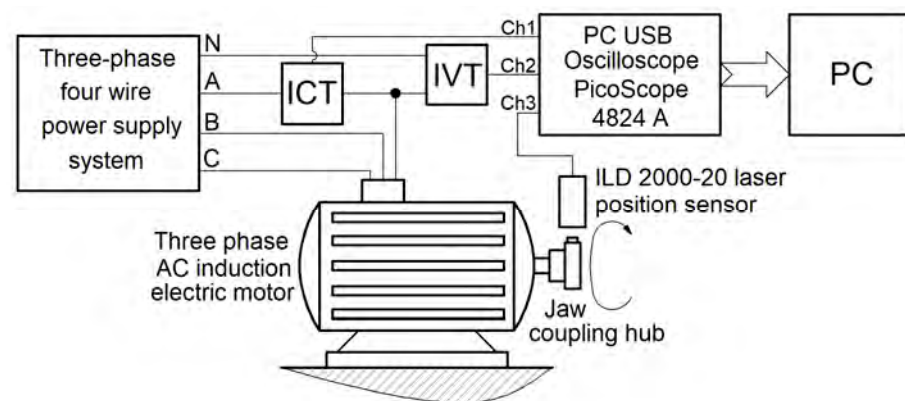


Figure 1. A conceptual description of the experimental setup.

It is reasonable to assume that the three-phase network (with theoretically pure sinusoidal voltages, 50 Hz frequency) is electrically balanced and that the IEP passing through the motor on each phase (A, B and C) is the same (one-third of the total IEP). The total IEP absorbed by the motor can be determined as three times the instantaneous power on a single phase (A, in Figure 1).

The primary winding of an instantaneous current transformer (ICT, labelled with 1 in Figure 2, which shows a partial photo of the setup) is supplied by phase A. It is reasonable to suppose that this transformer (acting as a current sensor) provides an IC description of the current ($i(t)$) that passes through phase A) on the secondary winding (as a proportional voltage $u_{CT}(t)$), which is delivered through the channel 1 (Ch1) of a PCB USB oscilloscope PicoScope 4824A (2 in Figure 2 [43]) to a personal computer (PC, 3 in Figure 2). The primary winding of an instantaneous voltage transformer (IVT, 4 in Figure 2) is placed between phase A and the null wire (neutral line) N. This transformer (acting as a voltage sensor) provides the IV description of the voltage ($u(t)$, between phase A and neutral wire) on the secondary winding (as a proportional voltage $u_{VT}(t)$), which is delivered through the channel 2 (Ch2) of the oscilloscope to PC. The PC also receives a signal $u_{SL}(t)$ from a laser position sensor ILD 2000-20 (1 in Figure 3) through the third channel (Ch3) of the oscilloscope. This signal is used to accurately describe the moment in time when an angular marker (2 in Figure 3) passes through the angular rotation origin (line 3 of the incident laser

beam, Figure 3) during its rotation. This angular marker is placed on a jaw coupling hub 4. In Figure 3, a permanent magnet (5) is also placed on this jaw coupling hub. In some experiments, it is used to create a temporary mechanical dynamic imbalance of the rotor.



Figure 2. A view on transformers ICT (1) and IVT (4) on digital oscilloscope (2) and personal computer (3).



Figure 3. A view of the jaw coupling hub placed on the motor rotor.

Two different theoretical synchronous speeds (750 or 1500 rpm obtained with 2 or 4 pairs of poles at 50 Hz frequency) are available for this motor, with nominal active electrical powers of 2.2 KW or 1.1 KW.

Figure 4 shows a view with the three signals acquired simultaneously during no-load operation at the theoretical synchronous speed of 1500 rpm: 1—a description $u_{VT}(t)$ involved in IV ($u(t)$) description as $u(t) = k_{VT} \cdot u_{VT}(t)$; 2—a description $u_{CT}(t)$ involved in IC ($i(t)$) description as $i(t) = k_{CT} \cdot u_{CT}(t)$; and 3—the voltage $u_{SL}(t)$ delivered by laser sensor.

As expected, the IC description is delayed compared to the IV description; there is a negative phase shift between the fundamentals of IV and IC (the stator winding acts as an inductive consumer). It is obvious that IV and especially IC are not pure sine waves, partly because of the power supply network but mainly because of the behaviour (condition) of the motor running. Each passing of the angular mark placed on the rotor through the angular origin produces a strong negative peak on $u_{SL}(t)$ signal (e.g., A or B); the time interval between two successive peaks corresponds to the period of a full rotation of the rotor.

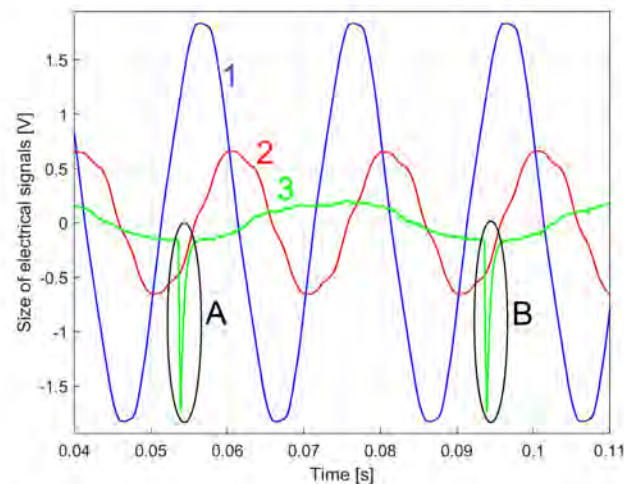


Figure 4. A partial variation of some signals over time: 1— $u_{VT}(t)$; 2— $u_{CT}(t)$; 3— $u_{SL}(t)$. A, B—two successive passes of the angular marker 2 through the angular rotation origin 3.

In this work, the processing of the data and the signals was carried out using MATLAB.

2.2. The Description of the Instantaneous Electrical Power

The IEP absorbed by the motor on phase A (p_A) is defined as $p_A(t) = u(t) \cdot i(t) = k_{VT} \cdot u_{VT}(t) \cdot k_{CT} \cdot u_{CT}(t)$, while the entire absorbed IEP (p) is three times bigger: $p(t) = 3p_A(t) = 3 \cdot k_{VT} \cdot k_{CT} \cdot u_{VT}(t) \cdot u_{CT}(t)$. In this setup, the constant part is $3 \cdot k_{VT} \cdot k_{CT} = 2573.76 \text{ W/V}^2$.

The use of IEP analysis to describe the state of the electric motor faces a serious obstacle: it contains a high-amplitude (dominant) sinusoidal component with a frequency of 100 Hz and many harmonics (as shown in [34]). Since the IV is not perfectly sinusoidal, the IEP also contains a sinusoidal component with a frequency of 50 Hz and some harmonics. This can be seen in Figure 5, which shows part of the FFT spectrum (in purple) of the IEP during 20 s of no-load motor operation at a theoretical synchronous speed of 1500 rpm (with $\Delta t = 10 \mu\text{s}$ as sampling time).

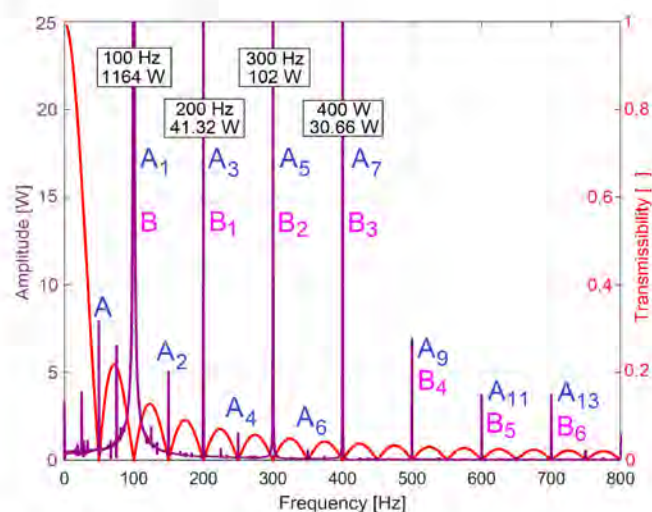


Figure 5. A part of the FFT spectrum of IEP (in purple), a part of the transmission curve of an appropriate backwards-moving average filter used to extract the IAEP from IEP (in red).

Here, A depicts the fundamental sinusoidal component at 50 Hz frequency, with some relevant harmonics (A_i , at $i \cdot 50 \text{ Hz}$ frequency), and B is that (huge) fundamental sinusoidal component at 100 Hz (previously mentioned), with some harmonics (B_i , at $i \cdot 100 \text{ Hz}$ frequency).

2.3. A Description of the Instantaneous Active Electrical Power

These sinusoidal components that were mentioned earlier (also partially revealed in [34]) are not involved in the description of motor condition and (for the purpose of motor monitoring) should be eliminated from IEP (e.g., ideally by using a notch filter with multiple narrow stop bands centred on the frequency of these components). Removing these sinusoidal components from the IEP gives the instantaneous active electrical power (IAEP). The IAEP is mainly related to the active mechanical power used to rotate the motor rotor (here in no-load operation).

The following is a proposal for a method to obtain a description of the IAEP (as IAEPf) through the filtering of the IEP. If we consider (as is undertaken in PC calculus) that the total IEP $p(t)$ is approximated by numerical samples, with the s th sample written as $p[s \cdot \Delta t] = 3 \cdot k_{VT} \cdot k_{CT} \cdot u_{VT}[s \cdot \Delta t] \cdot u_{CT}[s \cdot \Delta t]$, with sampling time Δt (with $s = \lfloor t / \Delta t \rfloor$), a simple way to eliminate all these unwanted components is to use a numerical backwards-moving average filter (BMAF) with a suitable number h of samples in the average. An output sample $P_f[s \cdot \Delta t]$ from BMAF (as an IAEPf sample as well) is defined as

$$P_f[s \cdot \Delta t] = \frac{1}{h} \sum_{j=0}^{h-1} p_s[(s-j) \cdot \Delta t] \text{ with } s \geq h \quad (1)$$

The number h should be determined in relation to the period ($T_{IV} = 50^{-1} \text{ s} = 0.02 \text{ s}$) of fundamental component A (T_{IV} being the period of IV), as $h = \lfloor T_{IV} / \Delta t \rfloor$. The IEP with the FFT spectrum partially described in Figure 5 has the sampling time $\Delta t = 10 \text{ } \mu\text{s}$, so $h = 2000$. In Figure 5, the transmissibility curve of a BMAF under these conditions is shown in red. Since it is superimposed on the FFT spectrum of IEP, it is clear that the transmissibility ($Tr(f)$) is zero exactly at the frequencies of the unwanted sinusoidal components, which are certainly removed by this averaging (with BMAF acting as multiple narrow stop band filter). Unfortunately, for many other frequencies (mainly related to the state of the motor), BMAF also acts as a strong attenuator. However, by multiplying the local (peak) FFT amplitude by the inverse of the transmissibility ($1/Tr(f)$, at the frequency of attenuated component), their real amplitude can be found. An important advantage of this IAEPf definition is that it maintains the same sampling time Δt as the IEP.

In classical acceptance [44], the instantaneous active electrical power (IAEPc) is calculated as the average value of the IEP over a period of IV. The g th sample $P_c[g \cdot T_{IV}]$ of IAEPc is calculated as the average of the h IEP samples during the time span of the g th period of IV as

$$P_c[g \cdot T_{IV}] = P_c[g \cdot h \cdot \Delta t] = \frac{1}{h} \sum_{s=(g-1) \cdot h+1}^{g \cdot h} p_s[s \cdot \Delta t] \quad (2)$$

The sampling time of IAEPc is T_{IV} , which is h times higher than IAEPf (as $T_{IV} = h \cdot \Delta t$). In other words, the sampling rate ($1/T_{IV}$) of the IAEPc is h times smaller than the sampling time ($1/\Delta t$) of the IAEPf, which is a big disadvantage.

In Figure 6, curve 1 represents a short sequence of IAEPf (as a result of IEP filtering using Equation (1)), curve 2 represents a short sequence of IAEPc (as a result of IEP averaging using Equation (2)), while a short sequence of IEP is represented by curve 3.

Because the amplitude of the dominant component A_1 in IEP is large (1164 W, Figure 5), IEP appears here as a series of parallel lines. The graphical representations of the powers are made by a series of successive line segments bounded at the ends by two points, with each point corresponding to a sample. A high description rate (as for IAEPf) means segments of small length and vice versa (as for IAEPc). It is obvious that IAEPf is much more suitable for motor condition monitoring than IAEPc due to its higher sampling rate.

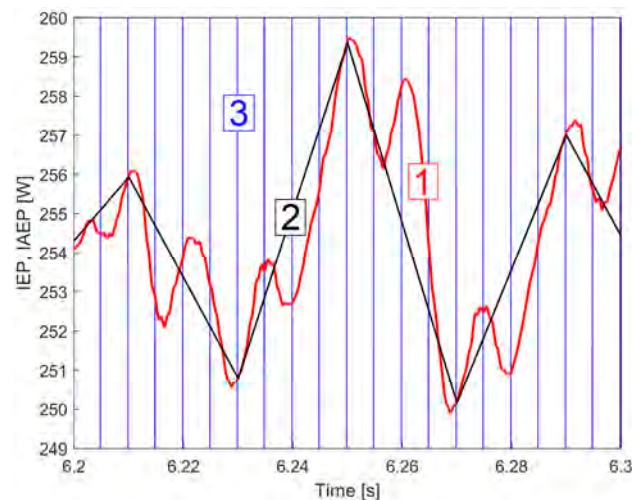


Figure 6. A short sequence showing the variation over time: 1—IAEPf; 2—IAEPc; 3—IEP.

2.4. A Method of Determining a Pattern in IAEpf Variation over Time Useful in Motor Condition Characterisation

There are two very simple ways of using IAEpf to monitor the condition of a three-phase AC induction asynchronous motor: 1, based on the variation of IAEpf over time at the start (more precisely, calculation of the active electrical energy absorbed during the start phase, ESP), and 2, based on the determination of the average IAEpf value running with no load (as constant part of IAEpf, or CAEPf).

There is also a third, more interesting approach. The mechanical power required to rotate the rotor of the motor with no load has a constant part (firmly reflected in CAEPf) and a variable part (also reflected in IAEpf), VIAEPf. The constant and variable parts of the IAEpf (CAEPf and VIAEPf) associated with the rotation of the rotor are absorbed by the motor from the electrical supply and converted partially into mechanical power, which is used to rotate the rotor with no load. Obviously, this VIAEPf is a sum of variable components, some of which are periodic. One of these components is expected to have a period equal to the period of rotation of the motor rotor. The time evolution of this periodic component reflects all the electrical and mechanical phenomena associated with the rotation of the rotor. One period of this component can be considered a pattern (PCRRf, periodic component on rotor rotation), useful (by its shape and size) for monitoring and diagnosing the state of the motor.

Assuming that there are no electrical phenomena associated with the rotation of the rotor, the peak-to-peak amplitude of this PCRRf should be zero if the rotor is in perfect mechanical condition (in terms of bearings, dynamic mechanical balance, vibration, etc.). Otherwise, this amplitude of the PCRRf is not zero, and the pattern shape and size can be an important indicator of the mechanical condition of the motor (from the point of view of its rotor rotation). A method for determining and synthetically describing the PCRRf (as pattern recognition) is proposed below.

The synthetic description of the pattern of a periodic phenomenon (in particular the PCRRf) within a periodic signal (in particular the IAEpf), with the period of this phenomenon T_p and n samples per period (where n is defined as $n = \lfloor T_p / \Delta t \rfloor$), is obtained by a special type of filtering by averaging of several selected samples (as FASS) of the variable part of the IAEpf (as VIAEPf, obtained by removing CAEPf from IAEpf, with samples represented as $P_{fv}[s \cdot \Delta t]$). A sample $P_{pT_p}[k \cdot \Delta t]$ (with $k = 1 \div n$) of PCRRf is obtained by arithmetic averaging of m uniformly selected samples of VIAEPf or as the average of these VIAEPf samples: $P_{fv}[k \cdot \Delta t]$, $P_{fv}[(n + k) \cdot \Delta t]$, $P_{fv}[(2 \cdot n + k) \cdot \Delta t]$, $P_{fv}[(3 \cdot n + k) \cdot \Delta t]$, ..., $P_{fv}[(m - 1) \cdot n + k] \cdot \Delta t$. There are n unselected VIAEPf samples between each of the two

successive samples selected for FASS. In other words, if VIAEPf has at least $m \cdot n$ samples, a sample $P_{pTp}[k \cdot \Delta t]$ of PCRRf is mathematically calculated by FASS as

$$P_{pTp}[k \cdot \Delta t] = \frac{1}{m} \sum_{i=1}^m P_{fv}\{[(i-1) \cdot n + k] \cdot \Delta t\} \text{ with } k = 1 \div n \quad (3)$$

The samples $P_{pTp}[k \cdot \Delta t]$ of any pattern of a periodic phenomenon within the IAEPf (in particular, the PCRRf) depend rigorously on the values of the period T_p and the sampling time Δt and are calculated on the basis of the number n (with $n = \lfloor T_p / \Delta t \rfloor$) and the optional value of m (in a first approach, the bigger, the better), according to Equation (3). The proposed FASS acts as a frequency-selective pass filter since it eliminates all the variable components of the VIAEPf that are not harmonically correlated with the fundamental frequency ($1/T_p$) of the periodic phenomenon being analysed. Obviously, the pattern of a variable periodic phenomenon within the VIAEPf can only be correctly extracted if (at least) its fundamental frequency is constant. For practical reasons, it is appropriate to calculate the samples of PCRRf using FASS according to Equation (3), where $k = 1$ corresponds to the moment when an angular marker on the rotor (e.g., the marker 2 from Figure 3) is passed through the origin (line 3 of the incident laser beam, the same Figure 3). Thus, by graphically superimposing the PCRRf patterns at different times or under different conditions of motor running with no load, similarities and possible differences can be seen. Also, in this way, a PCRRf can be described and studied not in terms of time but in terms of the angular position of the rotor (the pattern is described graphically with IAEPf on the y -axis and the angular position $\varphi_{pTp}[k \cdot \Delta t]$ of the rotor related by the angular origin on the x -axis, with $\varphi_{pTp}[k \cdot \Delta t] = 2\pi \cdot k \cdot \Delta t / T_p$).

The effectiveness of this FASS procedure can be demonstrated experimentally using a simulated VIAEPf signal. Let us suppose, for example, that this simulated signal can be described as the sum of 2000 sinusoidal components, having frequencies uniformly distributed between 0 and 1000 Hz, with the same amplitude (1W) and uniformly distributed phases at the origin of time. A sample of this simulated signal is generically described as follows:

$$P_{fv}[s \cdot \Delta t] = \sum_{j=0}^{2000} \sin(2 \cdot \pi \cdot \frac{j}{2} \cdot s \cdot \Delta t + \frac{j}{2}) \quad (4)$$

The variation of this simulated VIAEPf signal over time (with $\Delta t = 10 \mu s$ and $s = 1 \div 2,000,000$) is shown in Figure 7. A detail from area A is shown in the top right of figure.

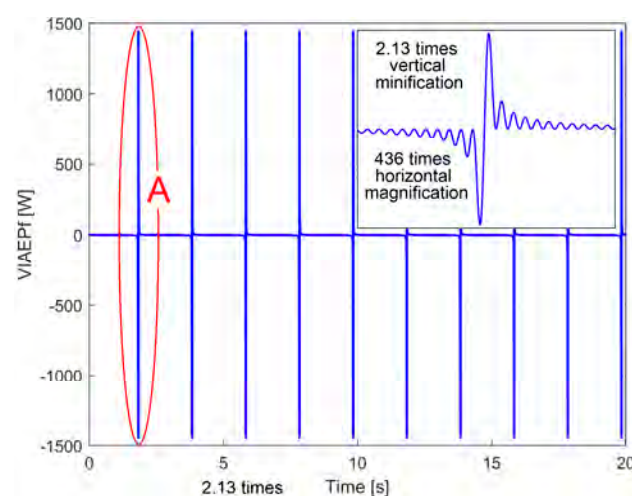


Figure 7. The variation of a simulated VIAEPf signal over time (described mathematically by Equation (4)) with $\Delta t = 10 \mu s$ and $s = 1 \div 2,000,000$.

The samples of a pattern of a periodic component (from simulated VIAEPf) with the fundamental frequency of 33.5 Hz (and harmonics at $2 \cdot 33.5$ Hz, $3 \cdot 33.5$ Hz, \dots $29 \cdot 33.5$ Hz) can be found using the FASS method shown in Equation (3), with $T_p = 1/33.5$ s, $n = 2985$ and $m = 600$ (an optional value). Figure 8 shows this pattern (in blue). Overlaid is the simulated pattern (in red), with a generic sample described with

$$P_{fvs}p[s \cdot \Delta t] = \sum_{l=0}^{29} \sin[33.5 \cdot l \cdot (2 \cdot \pi \cdot s \cdot \Delta t + 1)] \text{ with } s = 1 \div n \quad (5)$$

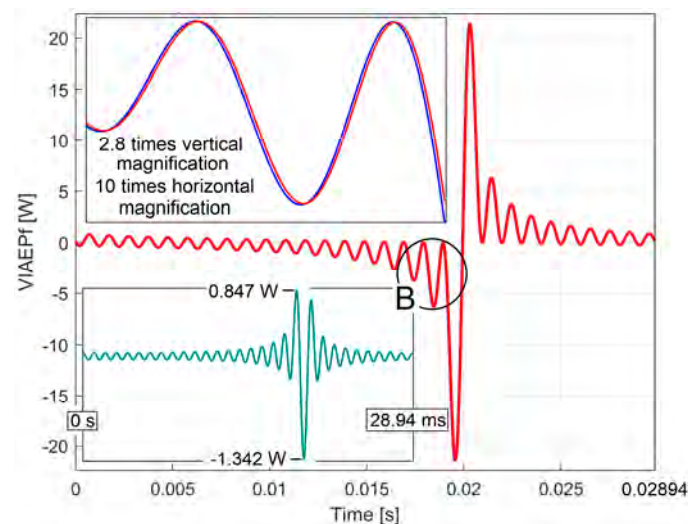


Figure 8. The pattern of a periodic component (with 33.5 Hz as the fundamental frequency) within the simulated VIAEPf signal found by FASS (in blue) superimposed on the simulated pattern (in red, Equation (5)).

As a result of substitution, $j/2 = 33.5 \cdot l$ in Equation (4). There appears to be a very good fit between the two patterns (simulated in Equation (5) and found by FASS of the signal generated with Equation (4)). As expected, due to the numerical description of VIAEPf, the overlap is not perfect (as shown in detail B, zoomed in at the top left of Figure 8). The bottom left area of this figure shows the variation over time of the difference between the simulated pattern (Equation (5)) and the pattern found by FASS (Equation (3)) of simulated VIAEPf (Equation (4)). This difference is not zero (at any moment in time), mainly because of the phase shift between the two patterns.

This convincing result leads to the conclusion that the FASS method can also be successfully used to determine the shape of any available periodic pattern within a variable signal (in particular, the PCRRf) within a real VIAEPf absorbed by a motor running with no load.

In order to apply the FASS (from Equation (3)), it is necessary to solve two essential requirements:

- The exact determination of the value of T_p , and n , with $n = \lfloor T_p / \Delta t \rfloor$. Of course, T_p is the period of a complete rotation of the rotor;
- The exact determination of a moment of time when the angular mark placed on the rotating rotor (2 in Figure 3) passes through the angular origin (when $k = 1$). This moment of time should preferably be chosen at the very beginning of the VIAEPf signal.

Both requirements can be met using the periodic signal $u_{SL}(t)$ generated by the laser sensor (1 in Figure 3) as the rotor rotates, described numerically as $u_{SL}[s \cdot \Delta t]$. Figure 9 shows a short sequence of this signal, suitably filtered with a BMAF.

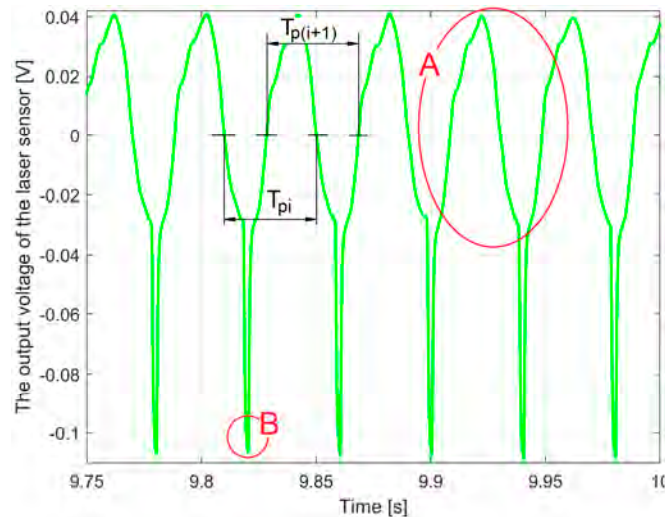


Figure 9. A sequence of $u_{SL}[s \cdot \Delta t]$ signal involved in the determination of the IAS value and the angular origin of the rotor.

There are two repeating parts: one in area A, caused by the run-out of the jaw coupling hub and the relative vibrations between the rotor and the laser sensor, and one in area B, which is related to the passage of the angular mark (2 in Figure 3) through the angular origin.

In area A, the time interval between any two successive zero crossings in the same direction of the signal $u_{SL}[s \cdot \Delta t]$ defines a value of the period of rotation of the motor rotor. Two examples, T_{pi} and $T_{p(i+1)}$, of such successive intervals are shown in the figure. The average value of all the time intervals that can be defined in this way on the entire signal $u_{SL}[s \cdot \Delta t]$ is the period value T_p .

A procedure for determining the exact time moments of the zero crossing of a signal has already been presented in [21]. The generic interval T_{pi} can be used to define the generic value of the average angular velocity ω_{pi} of the rotor (on one revolution) as $\omega_{pi} = 2\pi/T_{pi}$.

With respect to area B, in one of the first periods of the signal $u_{SL}[s \cdot \Delta t]$, we determine the time when this signal is minimum. At that time, k from Equation (3) can be set to 1 in order to obtain the description of PCRRf.

Of course, based on the values of T_p and Δt and an appropriate moment of time chosen for $k = 1$, it is possible to find a synthetic definition of a pattern within the $u_{SL}[s \cdot \Delta t]$ signal (as PCSL), which extends the usefulness of Equation (3), as we will see later.

3. Results

3.1. Some Resources Related to IAEPf, ESP and CAEPf in Motor Condition Monitoring Experimentally Revealed

Figure 10 shows the variation of IAEPf over time during a no-load run test with the motor idling at the first speed (750 rpm theoretical synchronous speed).

At start-up (by direct connection to the electrical network), zone A (shown in detail in the centre left of the figure) indicates a severe transient regime in which the absorbed IAEPf is very high (peaking at 9506 W) due to the acceleration of the rotor (start-up takes 71.5 ms). The energy absorbed during this transient process ($ESP = 334.5 \text{ W} \cdot \text{s}$) is calculated as the area (here coloured in cyan) bounded above by the IAEPf curve and below by a line representing the CAEPf value (437 W) and is converted mainly into mechanical energy, stored as rotor kinetic energy. The starting time, the ESP and CAEPf values (eventually the start-up time) can be considered indicators of the quality of the rotor (motor) condition. The CAEPf value is calculated as the average IAEPf during a stationary operation regime. This CAEPf supplies electrical dissipative phenomena (e.g., heating in the stator winding and rotor cage) and mechanical dissipative phenomena (e.g., dry and viscous friction during rotor movement).

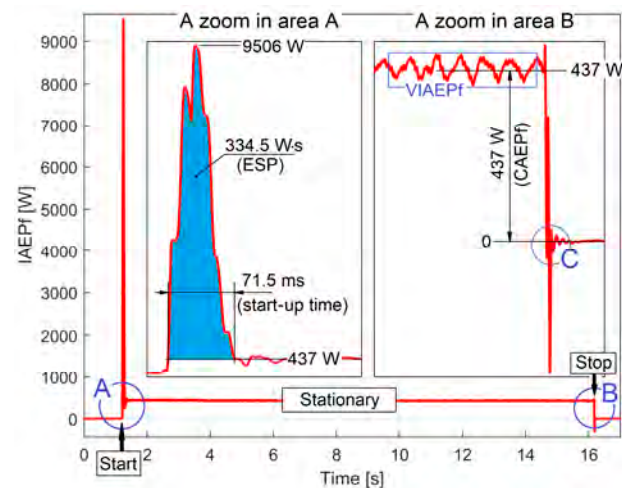


Figure 10. The variation of the IAEpf over time during a no-load test at 750 rpm theoretical synchronous speed.

A magnified view of B area (when the motor is electrically disconnected) is shown in the centre right of Figure 10. This shows the variable part of the IAEpf (as VIAEPf). Here, area C describes a phenomenon due to the electrical cut-off device (it does not characterise the motor behaviour).

By comparison with Figure 10, Figure 11 shows the same starting, stationary and stopping regime with the motor in no-load operation at 1500 rpm theoretical synchronous speed. Details A, B and C have meanings already discussed in Figure 10, detail D is represented and discussed in Figure 12. This time, as expected, the ESP value (888.48 W·s) and the starting time (93.6 ms) are higher. Unexpectedly, the CAEPf value (213.5 W) is lower than before despite the increase in mechanical energy dissipation. This means that the proportion of electrical dissipation in the CAEPf is much higher than that of mechanical dissipation.

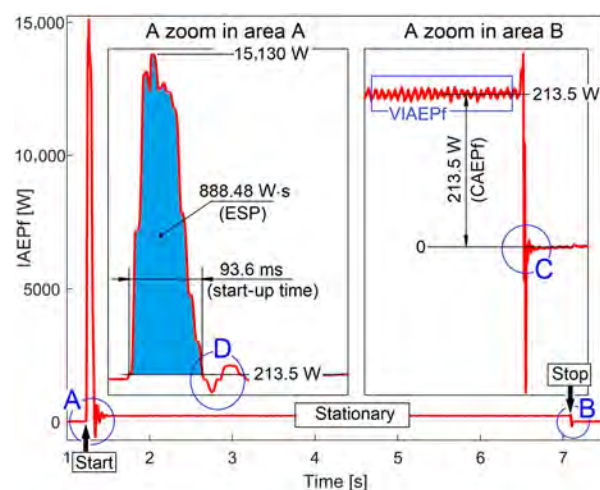


Figure 11. The variation of the IAEpf over time during a no-load test at 1500 rpm theoretical synchronous speed.

Each of these two IAEpf graphs (taken at the beginning of the motor's service life and used as a reference) can be compared later with graphs taken at regular (reasonably long) intervals. By highlighting any differences between them, changes in motor condition (rotor behaviour) can be identified.

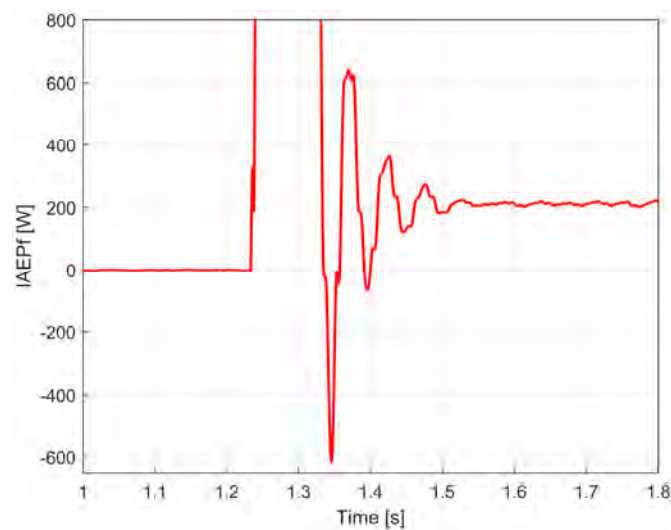


Figure 12. A zoomed-in detail in region D of Figure 11.

There are many other experimental resources available in the IAEpf signal. For example, Figure 12 shows a zoomed-in detail in region D of Figure 11 at the end of the transient (start) regime.

Here, the damped periodic viscous free response of the rotor dynamic system (with angular vibration) has been illustrated via IAEpf evolution. This system was excited when the transient regime suddenly ceased. This is also an element of motor condition monitoring (via frequency and damping ratio). This subject has already been studied before in [45].

This result provides additional evidence as to why IEP (via IAEpf) is more suitable than IC for engine condition monitoring. The IC alone cannot correctly describe the free response from Figure 12, nor the two short periods when the absorbed IAEpf is temporarily negative.

3.2. The Detection of PCRRf Patterns

The $u_{SL}[s \cdot \Delta t]$ signal was used to find the variation of first rotor rotation frequency in time [21] (with a generic sample f_{p1i} , defined with the rotation period T_{p1i} as $f_{p1i} = 1/T_{p1i}$) during a first experiment with no load test in stationary regime (with a duration of 20 s and sampling time $\Delta t = 10 \mu s$) at the theoretical synchronous speed of 750 rpm, as shown in Figure 13.

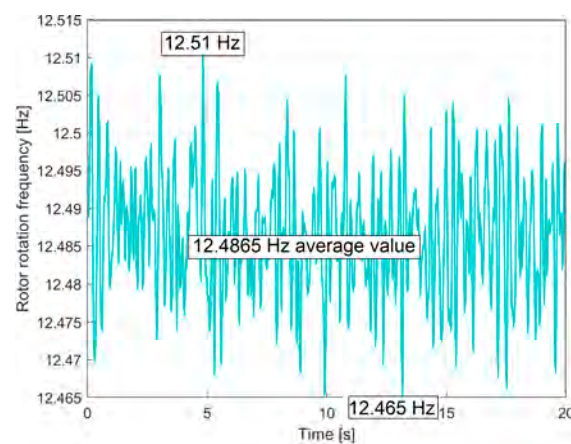


Figure 13. The variation of the rotor rotation frequency over time (low-pass filtered with a BMAF, four samples in the average) during a no-load stationary regime at the theoretical synchronous speed of 750 rpm.

There is a small peak-to-peak variation of 0.045 Hz around an average of $f_{p1} = 12.486463437276486$ Hz) for an average period of $T_{p1} = 1/f_{p1} = 0.080086727921266$ s (useful to find by FASS the PCRRf1 pattern of the first rotation speed of the rotor). The frequency variation from Figure 13 is caused by the relative vibrations between the laser sensor and the rotor and the torsional vibrations of the rotor. The average first rotor's rotation speed is $n_{p1} = 60 \cdot f_{p1} = 749.187$ rpm.

It is interesting to note that a similar study can be carried out in relation to the frequency f_{IV1} of the IV (based on a similar approach of the signal $u_{VT}[s \cdot \Delta t]$). Figure 14 shows the variation of this frequency over time during the same experiment.

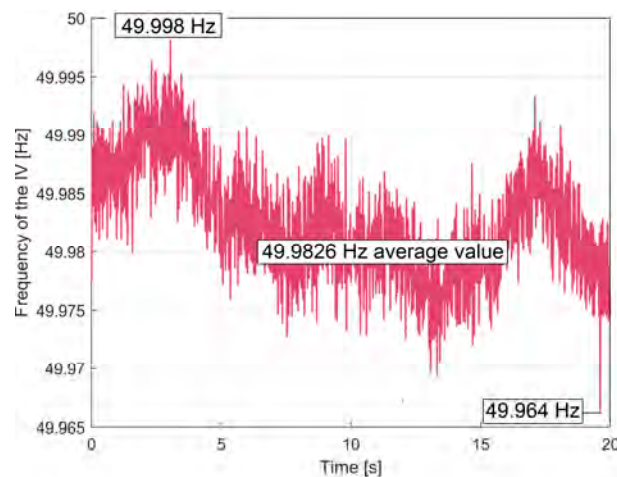


Figure 14. The variation of the IV frequency over time during the same stationary regime at the theoretical synchronous speed of 750 rpm.

There is a very small peak-to-peak variation of 0.034 Hz (due entirely to the behaviour of the electrical network supply) around an average value of $f_{IV1} = 49.9826$ Hz. This average frequency defines the exact value of the first synchronous motor's speed n_{s1} , as $n_{s1} = 60 \cdot f_{IV1} / p_1$ (with $p_1 = 4$ the number of pole pairs), so $n_{s1} = 749.739$ rpm. This average frequency f_{IV1} should be considered related to the average period $T_{IV1} = 1/f_{IV1}$. This average period is used to define the number of samples $h = 2001$ (from $h = \lfloor T_{IV1} / \Delta t \rfloor$) in the BMAF used in Equation (1) to define the IAEPf.

With these values of n_{p1} (also known as the first mechanical speed of the rotor) and n_{s1} (also known as the first electrical speed of the stator), it is possible to define an important motor characteristic, the no-load slip, as $s_1 = 100 \cdot (n_{s1} - n_{p1}) / n_{s1} = 0.07362\%$. This slip value (normally less than 5%) describes the torque provided by the motor (it increases as the torque increases).

A similar approach was performed for a second no-load test at a stationary regime for the second theoretical synchronous speed (1500 rpm, $p_2 = 2$). This time, these values were obtained: $f_{p2} = 24.979842608525143$ Hz, $T_{p2} = 0.040032277851852$ s (useful to find the PCRRf2 pattern of the second rotation speed of the rotor), $f_{IV2} = 49.9955$ Hz, $n_{p2} = 1498.790$ rpm, $n_{s2} = 1499.865$ rpm, $h = 2000$ and $s_2 = 0.07167\%$.

3.2.1. The Extraction of the PCRRf1 Patterns

The variation of the VIAEPf1 over time during the first experiment at 750 rpm is shown in Figure 15 (2,000,000-h samples, with $\Delta t = 10 \mu s$). A zoomed-in region, A, suggests that there is a dominant component within the VIAEPf1 that is expected to have the period of T_{p1} , which is expected to be reflected in the PCRRf1a pattern.

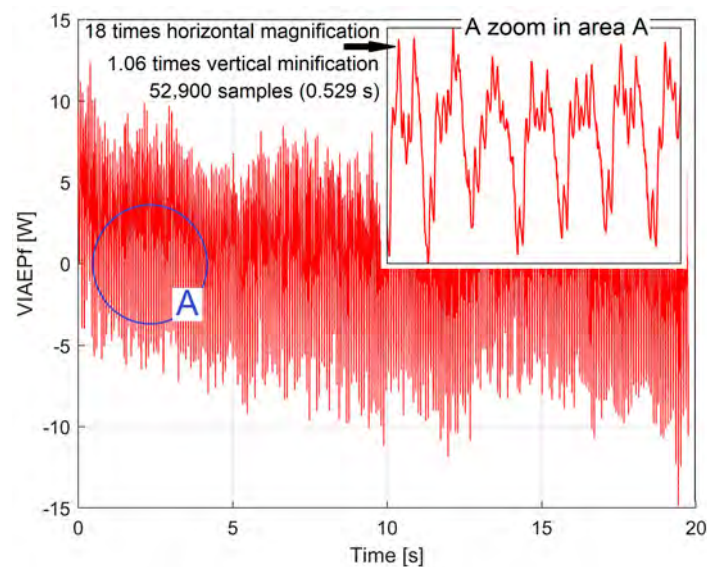


Figure 15. The variation of VIAEPf1 over time during a first experiment with the motor running with no load (at 750 rpm theoretical synchronous speed), which was used to extract the PCRRf1a pattern by FASS.

This PCRRf1a pattern is extracted by FASS, based on Equation (3), with T_p , m and n particularized as $T_{p1a} = 0.080086727921266$ s, $m_{1a} = 245$ and $n_{1a} = \lfloor T_{p1a} / \Delta t \rfloor = 8009$ samples. Figure 16 shows two periods of this PCRRf1a pattern (curve 1, in blue). This PCRRf1a pattern (with a peak-to-peak amplitude of approximately 9 W) is plotted relative to the position of the angular marker placed on the rotor (2, Figure 3); more precisely, it starts ($t = 0$) at the time when this marker passes through the angular origin. This moment is marked by a minimum value on the PCSL1a pattern. This PCSL1a pattern (shown in Geneva green colour, with curve 2 in Figure 16, also with two periods) is obtained by FASS treatment of the variable part of the signal $u_{SL}[s \cdot \Delta t]$ with exactly the same values T_{p1} , m_1 and n_1 used previously to extract the PCRRf1a pattern.

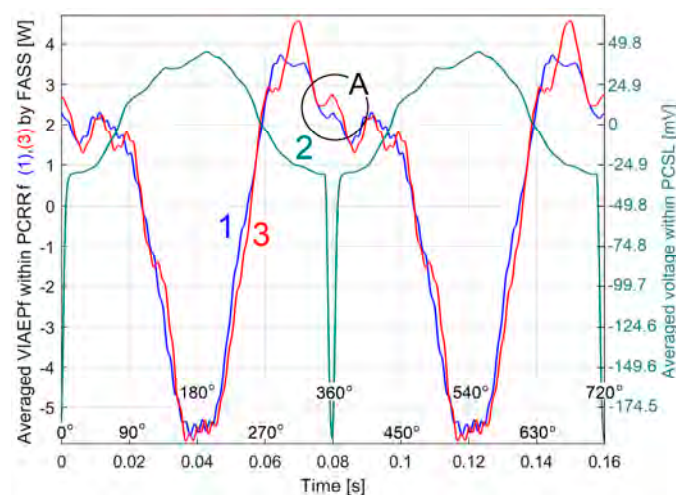


Figure 16. A representation of two periods from PCRRf1a pattern (1), PCSL1a pattern (2) and PCRRf1b pattern (3).

The x-axis of Figure 16 also shows the phase angle of the patterns with respect to the origin. However, this phase angle must be seen in the light of the fact that there is a gap (phase difference) between the variable mechanical phenomena and their reflection in the VIAEPf due to the dynamics of the rotor (its inertia, the rigidity of the rotating magnetic field, dry and viscous friction, rotation frequency, etc.).

The fact that this PCRRf1a pattern can be used to synthetically characterise this motor, running at first speed under no load, is confirmed by its repeatability. A new VIAEPf signal (identical in time and number of samples but acquired the next day) was processed with an identical FASS, resulting in a new pattern as PCRRf1b, represented by the red curve 3 in Figure 16. The PCSL1b pattern is identical to PCSL1a. Despite slightly different conditions ($T_{p1b} = 0.080057415179776$ s, $n_{1b} = 8006$ samples, $f_{IV1b} = 50.0017$ Hz, $s_{1b} = 0.07511\%$), the similarities with the PCRRf1a pattern are quite obvious.

The difference between these two patterns is partly explained by the variation of the instantaneous speed of rotation and consequently of the instantaneous periods T_{pi1} and T_{pi1a} and probably by some minor, normal changes in the condition of the motor. To be very rigorous, we must also point out a fact that proves that the accuracy of the PCRRf1a and PCRRf1b patterns is not perfect because, according to detail A, shown enlarged in Figure 17, there is a very small abnormal step discontinuity between the two periods. Conversely, this discontinuity is not observed in PCSL1a and PCSL1b.

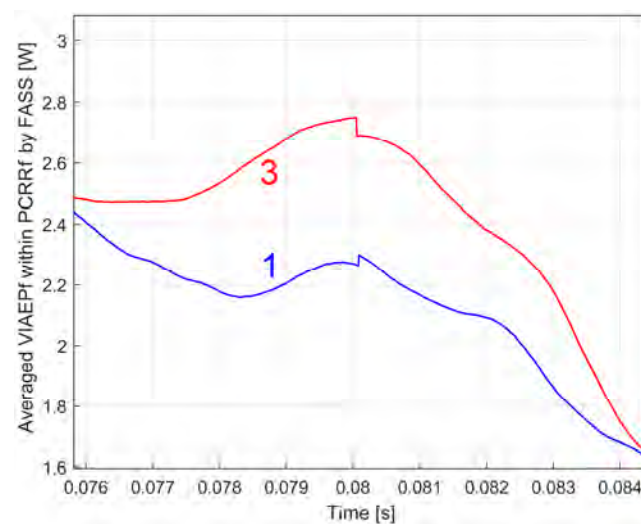


Figure 17. A magnified view of Figure 16 in area A, with PCRRf1a pattern (1) and PCRRf1b pattern (3).

According to Figure 3, a permanent magnet 5 (weighing about 10 g), as a dynamically unbalanced mass (DUM), was placed (at a distance of 35 mm from the axis) on the jaw coupling hub 4 mounted on the rotor in three different angular positions relative to the angular marker 2. For each position, the PCRRf1 pattern was recorded under the experimental conditions already described. In Figure 18 curve 1 shows the PCRRf1a pattern (already described above, without DUM), curve 2 shows the PCRRf1c pattern (the DUM placed at 60 degrees before the marker 2, relative to the direction of rotation), curve 3 shows the PCRRf1d pattern (the DUM placed at 60 degrees after the marker 2), and curve 4 shows the PCRRf1e pattern (the DUM placed at 180 degrees).

It would be expected that the centrifugal force generated by the dynamic imbalance (acting as a rotational force pushing radially against the bearings) would alter the PCRRf1 patterns. As can be clearly seen, there are no major differences between the patterns, indicating that these mechanical imbalances have an insignificant influence (mainly due to the low rotor speed). It should be noted that this rotating centrifugal force has another effect: it excites the motor to vibrate on its support. The mechanical power delivered by the motor to supply this vibration is obviously reflected in the IAEPf. This effect has not been highlighted here (e.g., by phase-shifting of patterns).

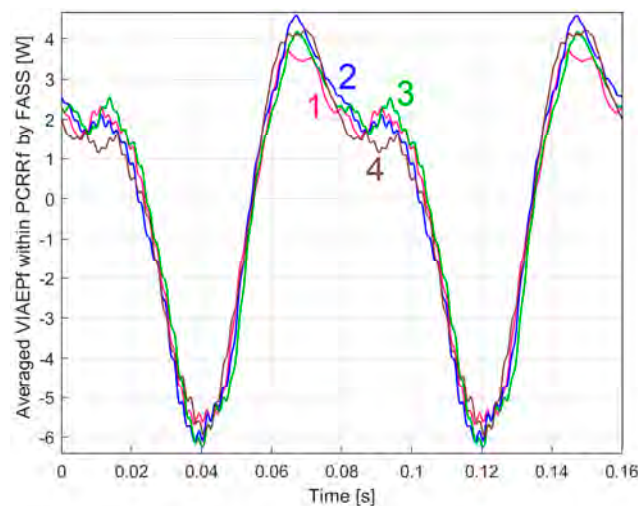


Figure 18. A representation of two periods from PCRR1 patterns obtained without DUM (curve 1) and with three different angular positions of DUM on the jaw coupling hub (curves 2, 3 and 4).

The Analysis of the PCRRf1a Pattern

Some resources provided by the analysis of the PCRRf1a pattern are presented below.

The FASS procedure was used to obtain the synthetic description of the PCRRf1a pattern (by the coordinates of the n points on the curve). An approximate analytical description of this pattern can be carried out as the sum of r sinusoidal components, with a sample formally described as

$$P_{pTp1a}[k \cdot \Delta t] \approx \sum_{i=1}^r A_{fai} \cdot \sin(2 \cdot \pi \cdot B_{fai} \cdot k \cdot \Delta t + C_{fai}) \text{ with } k = 1 \div n \quad (6)$$

A simple procedure (already introduced in [45]) is also available here to find the constants A_{fai} (as amplitudes), B_{fai} (as frequencies) and C_{fai} (as phases at the origin of time). Similarly to Figure 16 (which contains two periods of the PCRRf1s pattern), the synthetic definition of the PCRRf1a pattern is extended to more than one period (e.g., 10 periods). Thus, the description of a generic sample $P_{pTp1a}[k \cdot \Delta t]$ from the synthetic definition of the PCRRf1a pattern is available for $k = 1 \div 10 \cdot n$. Using the *Curve Fitting Tool* from MATLAB (R2019b), applied to the extended PCRRf1a pattern, it is possible to quite accurately find the values of the constants from Equation (6) up to a reasonable upper limit r (here $r = 15$). The extended PCRRf1a pattern (with ten periods) rather than the normal pattern (with one period) is used to increase the accuracy of determining the values of the constants A_{fai} , B_{fai} and C_{fai} . A model with a sum of eight sinusoidal components was used in the curve-fitting procedure. A first curve-fitting procedure produces the values of the first eight sets of constants (for $i = 1 \div 8$). The eight harmonic components defined by these sets are mathematically removed from the extended PCRRf1a pattern. The curve-fitting procedure is then reapplied to the remainder of the pattern, finding another eight sets of constants (for $i = 9 \div 16$). One set is ignored, corresponding to a component with insignificant amplitude. The values of the constants thus determined are given in Table 2 in ascending order of frequencies B_{fai} .

It is quite obvious that, as predicted, FASS has produced two notable results: first, it has removed all signal components that are not harmonically correlated with the T_{p1a} period (and the signal noise, too), and second, it has retained only the pattern sinusoidal components that are harmonically correlated with this period. In other words, there is a harmonic correlation between the B_{fai} frequencies ($B_{fai} \approx i \cdot B_{fa1}$). Some harmonics are missing. For example, the third harmonic (with a frequency of 49.9428 Hz) is missing because it is very close to the 50 Hz frequency and is removed by the BMAF filter used to

define IAEPf1a from IEP. The absence of the other harmonics is due to the peculiarities of the shape of the PCRRf1a pattern.

Table 2. The values of the constants A_{fai} , B_{fai} and C_{fai} involved in the analytical description of the PCRRf1a pattern using Equation (6).

i	A_{fai} [W]	B_{fai} [Hz]		C_{fai} [rad]
1	3.945	$12.4857 = 1/T_{p1a} = B_{fa1}$	Fundamental	1.725
2	1.913	$24.9714 = 2 \cdot B_{fa1}$	1st harmonic	−1.747
3	0.02436	$37.4491 = 2.9993 \cdot B_{fa1}$	2nd harmonic	1.059
4	0.02832	$62.4364 = 5.0006 \cdot B_{fa1}$	4th harmonic	−2.031
5	0.1168	$74.9142 = 6 \cdot B_{fa1}$	5th harmonic	2.07
6	0.09591	$87.4078 = 7 \cdot B_{fa1}$	6th harmonic	−1.45
7	0.1688	$99.8856 = 8 \cdot B_{fa1}$	7th harmonic	0.9121
8	0.06114	$112.3474 = 8.9980 \cdot B_{fa1}$	8th harmonic	1.169
9	0.04019	$124.8570 = 10 \cdot B_{fa1}$	9th harmonic	0.5538
10	0.02553	$137.3507 = 11 \cdot B_{fa1}$	10th harmonic	1.596
11	0.02038	$324.6760 = 26 \cdot B_{fa1}$	25th harmonic	2.634
12	0.02024	$337.0901 = 26.9980 \cdot B_{fa1}$	26th harmonic	1.23
13	0.06175	$424.6253 = 34.0089 \cdot B_{fa1}$	33rd harmonic	−2.366
14	0.05657	$437.0394 = 35.0032 \cdot B_{fa1}$	34th harmonic	1.26
15	0.01367	$536.8296 = 42.9955 \cdot B_{fa1}$	42nd harmonic	−0.5324

The quality of the analytical description of the PCRRf1a pattern, based on the definition from Equation (6) and the values in Table 2, can be illustrated simply by plotting the two patterns, as shown in Figure 19.

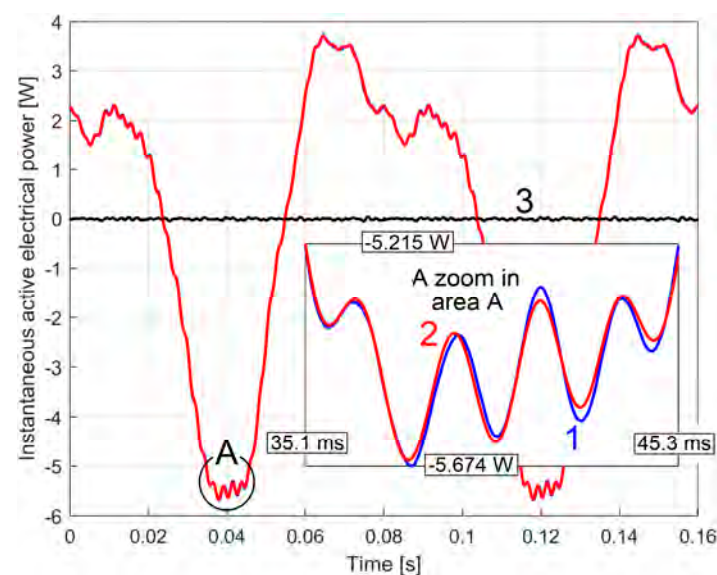


Figure 19. Representation of PCRRf1a patterns (on two periods): 1—with synthetic definition (by FASS); 2—with analytical definition (using Equation (6) with $r = 15$, found by curve fitting); 3—the difference between these patterns (as residual).

This figure shows two periods of the synthetic pattern (in blue, curve 1, visible when zooming into area A, where the overlap is worst) and two periods of the analytical pattern (in red, curve 2). A very good analytical description makes the two patterns overlap very well, and the (insignificant) differences are shown (as an example) in zoom-in area A.

Curve 3 (in black) shows the variation over time of the difference (sample by sample) between the two patterns (as a residual, what remains after the mathematical subtraction of the analytical model from the synthetic one).

Obtaining analytical descriptions of the patterns facilitates the application of more advanced motor condition monitoring strategies (e.g., related to a phenomenon described by the evolution of a particular harmonic).

There is another way to describe the content of the PCRRf1a pattern based on the FFT (Fast Fourier Transform) spectrum. In order to obtain a high resolution of the spectrum (in frequency), it is essential to use the FFT of the extended PCRRf1a pattern (e.g., for 10 periods, as before).

The FFT spectrum of the extended synthetic PCRRf1a pattern is shown in Figure 20, window 1 (in the frequency range of $0 \div 550$ Hz).

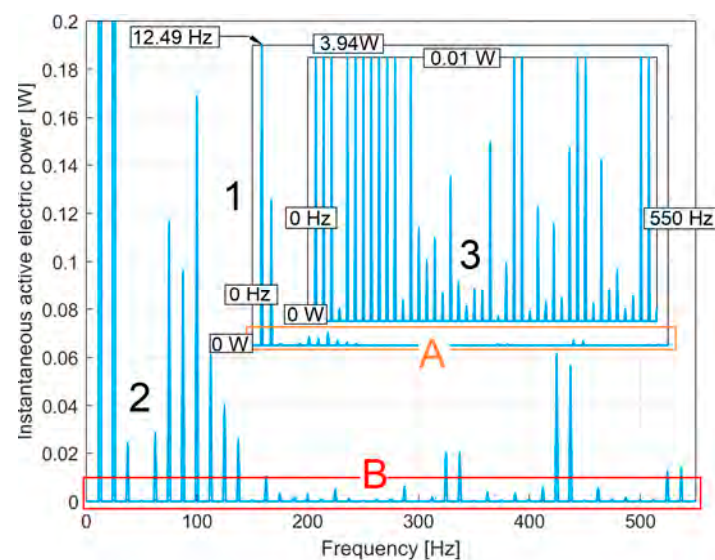


Figure 20. 1—the partial FFT spectrum of the synthetic PCRRf1a extended pattern (10 periods); 2—a zoomed-in area A; 3—a zoomed-in area B.

A zoomed-in portion of this spectrum from region A (the same frequency range, $0 \div 0.2$ W range on the y -axis) is shown in window 2. A zoomed-in portion of this spectrum from region B (the same frequency range, $0 \div 0.01$ W range on the y -axis) is shown in window 3. As can be clearly seen in window 1, all harmonics of the fundamental component (with period T_{p1a}) are practically represented, which means that the analytical description of the pattern from Equation (6) can theoretically be raised over $r = 15$. The dominant sinusoidal component (previously identified by curve fitting and described in the first row of Table 2) is also well represented here (with frequency and amplitude by the highest peak in window 1). However, here and for all other sinusoidal components shown in the spectrum, the phase angle at the time origin is missing (not provided by FFT).

Similarly to window 1 in Figure 20, curve 1 in Figure 21 shows a zoomed-in portion of the FFT spectrum of the extended analytical PCRRf1a (in the frequency range $0 \div 550$ Hz). As expected, there are only 15 peaks in this spectrum, corresponding to the 15 components identified before by curve fitting (and described in Table 2).

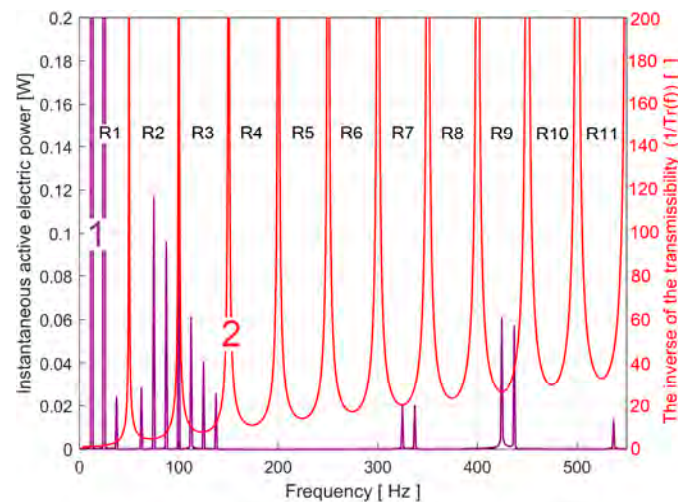


Figure 21. 1—the partial FFT spectrum of the analytical PCRRf1a extended pattern (10 periods); 2—the lower part of the curve of the inverse transmissibility of the BMAF filter ($1/Tr(f)$) used to obtain IAEPf from IEP.

It is important to note that both PCRRf1a patterns (synthetic and analytical) are affected by the action of BMAF (which previously allowed the definition of IAEPf from IEP) in the sense that practically the amplitudes of all sinusoidal components of these patterns are attenuated (and some of them are eliminated) on the one hand (i.e., depending on their frequency, their real amplitudes are found at the output of the filter multiplied by the transmissibility $Tr(f)$ of the filter, with $Tr(f) < 1$), and on the other hand, their phases at the time origin are modified (a phase angle is introduced by filtering). The frequencies of the sinusoidal components remain unchanged. The variation of this transmissibility $Tr(f)$, depending on frequency, has already been shown (as an example) in Figure 5 (BMAF with $h = 2000$) for PCRRf1a; in particular, $h = 2001$.

This question now arises: is it possible to obtain the real pattern unaffected by these two deficiencies (as the PCRR1a pattern)? Since the description of the main components of the analytical PCRRf1a is fully known (Table 2), there is a simple way to find the real amplitudes (as A_{ai}) of the sinusoidal components: amplify the amplitudes (A_{fai}) with the inverse of the BMAF transmissibility ($1/Tr(f)$) at frequencies $f = B_{fai}$, so $A_{ai} = A_{fai}/Tr(B_{fai})$. As a consequence, because $Tr(f) < 1$, all the amplitudes A_{ai} increase ($A_{ai} > A_{fai}$). The variation of the inverse of the transmissibility with the frequency (within $0 \div 550$ Hz range) was shown before in Figure 21 (the red curve, 2). On the $1/Tr(f)$ curve (with an upper limit at 200), there are some peaks (with infinite amplitudes) corresponding to $Tr(f) = 0$ and the regions labelled R1, R2, ..., R11 in between.

It is easy to prove that only in the even regions (R2, R4, ..., R10) is a phase shift of π radians introduced by BMAF so that the real phase angles at the origin of time (as C_{fai}) should be rewritten as $C_{ai} = C_{fai} + \pi$. Only the components $i = 4 \div 6$ fulfil this condition, such as when placed in R2.

Using these amplitude and phase correction approaches, the description of the sinusoidal components of the real analytical pattern PCRR1a is given in Table 3.

Unexpectedly, the amplitude A_{a7} is huge. A simple reason explains this fact: within the IEP, there is a huge dominant component of 100 Hz (1164 W, as shown in Figure 5). Because of the sampling, new sinusoidal components are artificially created (due to a phenomenon known as spectral leakage) and are very close (in frequency) to this dominant component. This component is not completely removed by the BMAF. It is obvious that this component must be compulsorily neglected in the analytical patterns PCRRf1a and PCRR1a. Based on Equation (6)—where A_{fai} , B_{fai} and C_{fai} have been replaced by A_{ai} , B_{ai} and C_{ai} from Table 3, the analytical pattern PCRR1a was built (with two periods) as shown in Figure 22 (curve 1), superimposed on the analytical pattern PCRRf1a (curve 2, also with two periods). It is

obvious that the PCRR1a pattern filtering using the BMAF (with $h = 2001$) produces the PCRRf1a pattern.

Table 3. The values of the constants A_{ai} , B_{ai} and C_{ai} involved in the analytical description of the PCRR1a pattern using Equation (6).

i	A_{fai} [W]	$1/\text{Tr}(B_{fai})$	$A_{ai} = A_{fai} \cdot 1/\text{Tr}(B_{fai})$ [W]	B_{ai} [Hz]		C_{ai} [rad]
1	3.945	1.103	4.351	12.4857	Fundamental	1.725
2	1.913	1.568	2.999	24.9714	1st harmonic	-1.747
3	0.02436	3.311	0.0807	37.4491	2nd harmonic	1.059
4	0.02832	5.578	0.1580	62.4364	4th harmonic	$-2.031 + \pi = 1.105$
5	0.1168	4.704	0.5494	74.9142	5th harmonic	$2.07 + \pi = 5.2115$
6	0.09591	7.697	0.7382	87.4078	6th harmonic	$-1.45 + \pi = 1.6915$
7	0.1688	608	102.6304	99.8856	7th harmonic	0.9121
8	0.06114	10.111	0.6182	112.3474	8th harmonic	1.169
9	0.04019	7.841	0.3151	124.8570	9th harmonic	0.5538
10	0.02553	12.035	0.3073	137.3507	10th harmonic	1.596
11	0.02038	20.398	0.4157	324.6760	25th harmonic	2.634
12	0.02024	28.90	0.5849	337.0901	26th harmonic	1.23
13	0.06175	26.684	1.6477	424.6253	33rd harmonic	-2.366
14	0.05657	37.25	2.1072	437.0394	34th harmonic	1.26
15	0.01367	45.09	0.6164	536.8296	42nd harmonic	-0.5324

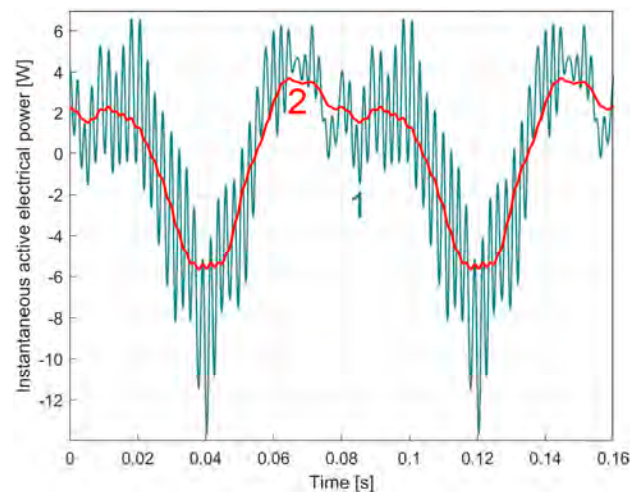


Figure 22. Graphical descriptions of two periods from 1, the analytical PCRR1a pattern, and 2, the analytical PCRRf1a pattern.

Of course, a more complete description of the analytical PCRR1a pattern can be obtained if the component identification on synthetic extended PCRRf1a is performed by curve fitting for $r > 15$. As can be seen from the FFT spectrum in Figure 20, there are many other small amplitude sinusoidal components that can be considered in this description.

It is obvious that the analytical PCRR1a pattern can only be deduced by knowing the analytical approximation of the PCRRf1a pattern (from Equation (6), here, based on the data in Table 2). In other words, it is not possible to directly use the synthetically defined PCRRf1a pattern for this purpose.

It is interesting to look at the similarities between the PCRR1a and PCRR1b patterns (PCRR1b being similarly obtained from PCRRf1b). Figure 23 shows these two patterns superimposed (curve 1 as PCRR1a and curve 2 as PCRR1b, both with two periods).

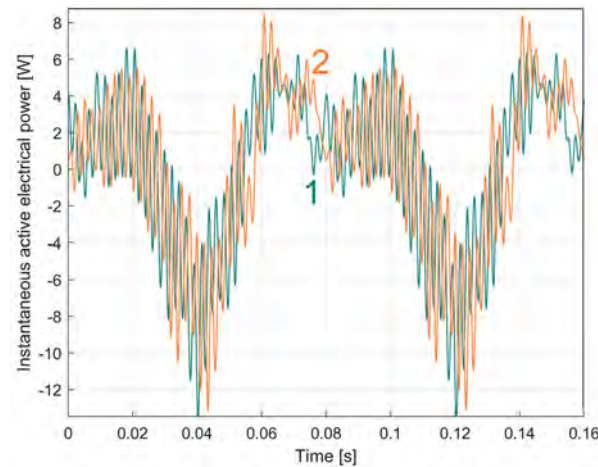


Figure 23. Graphical descriptions of two periods: 1—the analytical PCRR1a pattern; 2—the analytical PCRR1b pattern.

As can be clearly seen, there are some similarities but also some relatively large differences (the patterns do not fit perfectly). The first plausible reason for these differences is the accuracy of the curve-fitting procedure used to find the mathematical description of the synthetic patterns, as it is less accurate in describing the low-amplitude sinusoidal components (which also have high frequencies) in PCRR1fa and b. An approach to a more accurate curve-fitting procedure is needed as a future challenge.

We believe that, for the time being, the use of analytical PCRRf1a and b patterns or their FFT spectra is more reliable for motor condition monitoring.

3.2.2. The Extraction and the Analysis of the PCRRf2 Patterns

Similar to Figure 15, the variation of the VIAEPf (as VIAEPf2a) over time during a first experiment (without DUM) at 1500 rpm (theoretical synchronous speed) is shown in Figure 24 (also with 2,000,000-*h* samples, and $\Delta t = 10 \mu\text{s}$). Zooming in on region A shows (as an example) the local character of the instantaneous active electrical power variation.

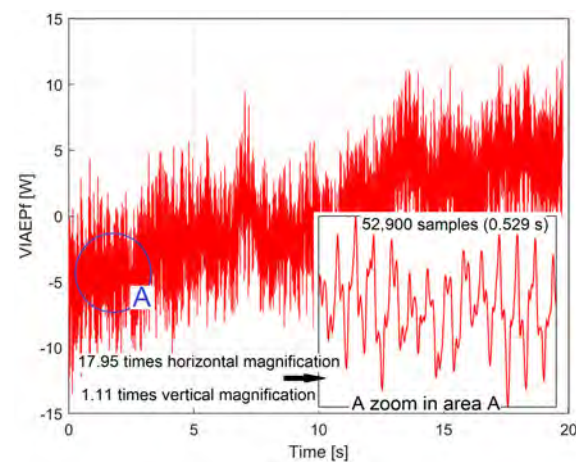


Figure 24. The variation of the VIAEPf2a over time during a first test (without DUM) with the motor running with no load (at 1500 rpm theoretical synchronous speed) used to extract the PCRRf2a pattern by FASS.

Using the FASS procedure—based on Equation (3)—it was possible to extract a first PCRRf2 pattern (as PCRRf2a, with $T_{p2a} = 0.040018907773371$ s, $n_{2a} = 4002$ and $m_{2a} = 460$) described with two periods, with curve 1 in Figure 25. In the same figure, curve 2 shows a PCRRf2b pattern (from a second identical sequence, VIAEPf2b, sampled after 200 s, with the motor running continuously after the first experiment), and curve 3 shows a PCRRf2c pattern (from a third identical sequence, VIAEPf2c, sampled after 400 s, with the motor running continuously after the first experiment). Curve 4 shows the overlaid patterns of PCSL2a, b, and c, also with two periods.

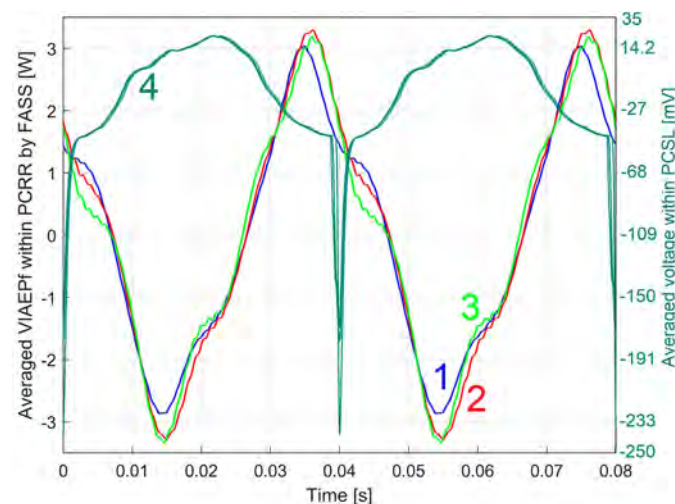


Figure 25. A graphical representation with two periods of the patterns: 1—PCRRf2a; 2—PCRRf2b; 3—PCRRf2c; 4—overlaid PCSL2a, b, c.

There is a logical assumption that PCRRf2a, b and c patterns are strictly correlated with PCSL2a, b and c patterns (PCRRf2a, b and c start and end on a minimum of PCSL2a, b and c). The FASS method of extracting both types of patterns means that they no longer start strictly on the PCSL2a, b and c minima (due to averaging with a high m value and local variation of $T_{p2a,b,c}$ periods). Thus, after the initial selection of the sample position for $k = 1$ (from Equation (3)) on a minimum of the $u_{SL}[s \cdot \Delta t]$ signal and obtaining the patterns, for each pair of patterns (e.g., PCRRf2a and PCSL2a), the value of k is slightly adjusted appropriately until the PCSL2a starts strictly on its minimum (or more simply, until the n th sample of PCSL2a is exactly its minimum). In this way, we are sure that the PCSL2a, b and c patterns overlap as much as possible (as Figure 25 clearly shows), and therefore, we expect to have the correct overlap of the PCRRf2a, b and c patterns (for comparison between).

As Figure 25 clearly shows, the PCRRf2a, b and c patterns (found under similar experimental conditions) overlap quite well, having quite similar shapes and amplitudes, which once again indicates that this type of pattern is an important indicator within the IAEPf, which is useful for describing the state of the motor running with no load.

It is interesting to remark that the average peak-to-peak amplitude of these patterns is smaller than the average peak-to-peak amplitude of the patterns PCRRf1a and b (Figure 16). There is a hypothesis here: probably the dynamic system of the rotor and the rotating magnetic field now acts as an attenuator; the variable mechanical phenomena (at a higher instantaneous speed now than before) are reflected with reduced amplitudes in the IAEPf.

The practical usefulness of this PCRRf2 pattern can be illustrated experimentally by showing how it changes with the introduction of different no-load running conditions for the motor rotor, e.g., by adding the DUM to the rotor [10], at different angular positions (a topic already discussed before). According to Figure 3, the DUM was placed on the jaw coupling hub mounted on the rotor (at a distance of 35 cm from the axis) at 60 degrees before the angular marker 2, relative to the direction of rotation.

Three consecutive identical tests were carried out with the motor continuously running with no load with 1500 rpm (theoretical synchronous speed) with the same time delay between as before (at 0 s, 200 s and 400 s), with VIAEPf2 registration (2,000,000-h samples, with $\Delta t = 10 \mu s$) and extraction of three new PCRRf2 patterns (as PCRRf2a1, b1 and c1), graphically represented (with two periods each one) in Figure 26 (as curves 1, 2 and 3). Curve 4 shows the PCSL2a1 pattern (as a formal representation, without indication of vertical magnification). For comparison, curve 4 shows the PCRRf2a pattern from Figure 25 (now with colour changing from blue to black).

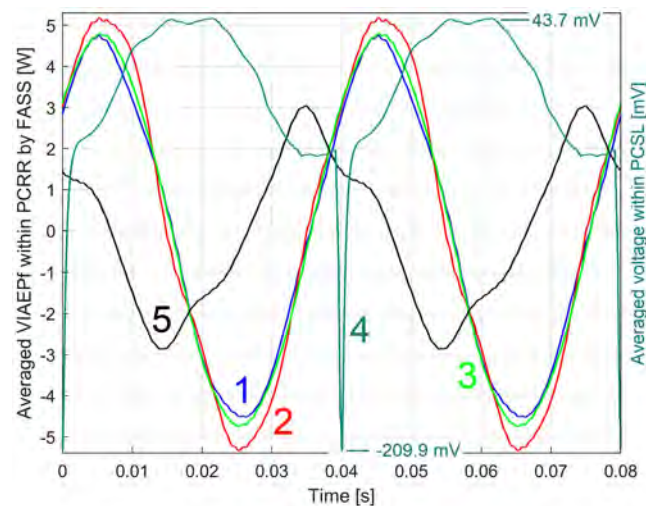


Figure 26. The effect of the DUM placed on the jaw coupling hub at 60 degrees before the angular marker. A graphical representation with two periods of the patterns: 1—PCRRf2a1; 2—PCRRf2b1; 3—PCRRf2c1; 4—PCSL2a1; 5—PCRRf2a.

As expected, there are significant similarities between the three patterns PCRRf2a1, b1 and c1 (as describing similar experiments), and, interestingly, there are significant differences compared to the PCRRf2a pattern (in peak-to-peak amplitude, shape and time lag to the angular marker 2 on the rotor shown in Figure 3), which are certainly as an effect of the DUM (through the rotary centrifugal force of 8.63 N thus created), which is better highlighted now due to the higher rotor speed. Of course, it is possible to investigate the content of harmonically correlated sinusoidal components of these patterns (e.g., PCRRf2a1) using the curve-fitting method or to describe these contents using the FFT transform, as shown above.

Three further similar identical tests were carried out under the same conditions, this time with the DUM placed 60 degrees behind the angular reference 2 from Figure 3 (relative to the direction of rotor rotation). The patterns PCRRf2a2, b2 and c2 were extracted and plotted in Figure 27 (represented by curves 1, 2 and 3). Here, curve 4 shows the pattern PCSL2a2 (without indication of vertical magnification), curve 5 shows the pattern PCRRf2a identical to Figure 25 (for comparison), and curve 6 shows the pattern PCRRf2a1 from Figure 26 (now with colour changing from blue to magenta).

As expected, there are again significant similarities between the three patterns, PCRRf2a2, b2 and c2 (as describing similar experiments), which are better than before (Figure 26).

It is now clear that the amplitude of the PCRRf2a2, b2 and c2 patterns is even greater this time, suggesting that the rotor itself (without DUM) is dynamically unbalanced. In these new experiments, the additional mass increases the total dynamic imbalance. The change of the phase shift from the origin (the minimum on the PCSL2a2 signal) is also evident.

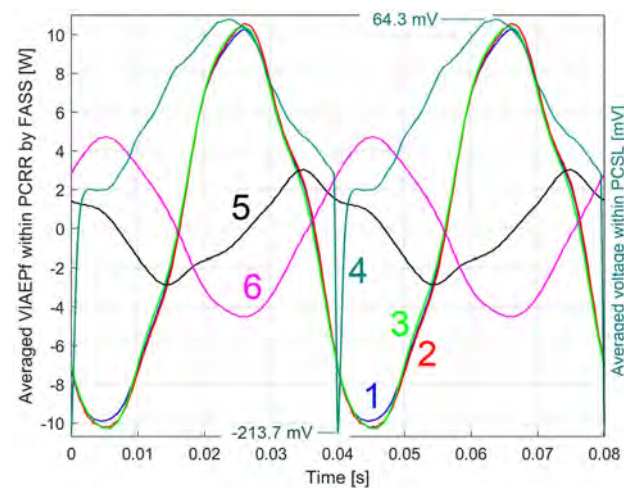


Figure 27. The effect of the DUM placed on the jaw coupling hub at 60 degrees behind the angular marker. A graphical representation with two periods of the patterns: 1—PCRRf2a2; 2—PCRRf2b2; 3—PCRRf2c2; 4—PCSL2a2; 5—PCRRf2a (from Figure 25); 6—PCRRf2a1 (from Figure 26).

Finally, three more similar identical tests were carried out under the same conditions, except this time the DUM, which now is positioned at 180 degrees from the angular mark 2. The patterns PCRRf2a3, b3 and c3 were extracted and plotted in Figure 28 (represented by curves 1, 2 and 3). Here, curve 4 shows the pattern PCSL2a3 (without indication of vertical magnification), curve 5 shows the pattern PCRRf2a, also shown in Figures 26 and 27 (for comparison), curve 6 shows the pattern PCRRf2a1 also shown in Figure 27 (for comparison), and curve 7 shows the pattern PCRRf2a2 from Figure 27 (with colour change from blue to purple). For the new patterns (PCRRf2a3, b3 and c3), there is a small increase in amplitude but a significant change in phase shifting (revealed here as a time lag) compared to the origin.

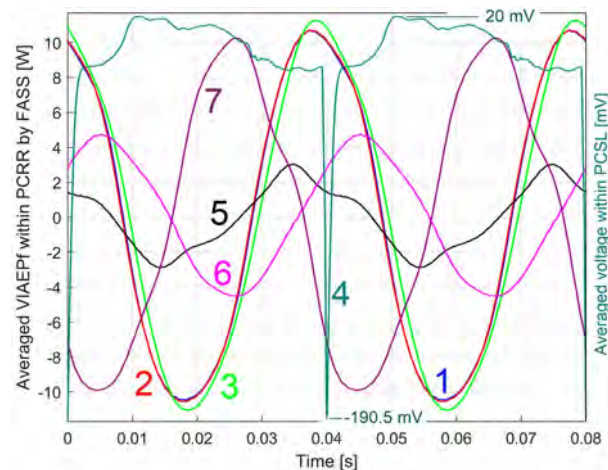


Figure 28. A graphical representation with two periods of the patterns: 1—PCRRf2a3; 2—PCRRf2b3; 3—PCRRf2c3; 4—PCSL2a3; 5—PCRRf2a (from Figure 25); 6—PCRRf2a1 (from Figure 26); 7—PCRRf2a2 (from Figure 27).

In order to have a clearer idea of the influence of the angular position of the DUM placed on the jaw coupling hub (and also on the rotor), Figure 29 shows a synthesis of the experimental results: only the PCRRf2a, a1, a2 and a3 patterns and the PCSL2a3 pattern (used to mark the origin of the patterns) are shown. Here, PCRRf2a is the pattern obtained when the rotor rotates at 1500 rpm (theoretical rotation speed) without the DUM (also curve 1 in Figure 25), PCRRf2a1 is obtained when the rotor rotates with the DUM placed

at 60 degrees before the angular marker (also curve 1 in Figure 26), PCRRf2a2 is obtained when the rotor rotates with the DUM placed at 60 degrees after the angular marker (also curve 1 in Figure 27), and PCRRf2a3 is obtained when the rotor rotates with the DUM placed at 180 degrees against the angular marker (also curve 1 in Figure 27).

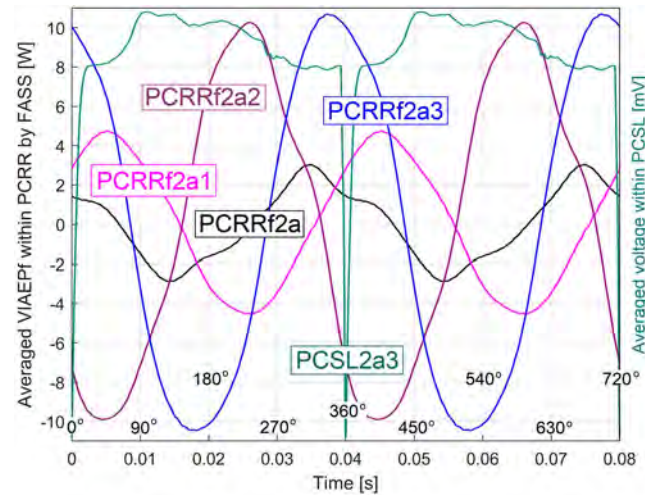


Figure 29. A graphical representation with two periods of the patterns.

On the x -axis of Figure 29, the values of time and the angle to the origin of the rotor (2 in Figure 3) are marked.

These angular values on the x -axis help to relate the position of the patterns to the angular origin on the rotor (placed here at 0 degrees). In the event of a rotor malfunction (usually of a mechanical nature), this helps to identify the cause.

As a general remark, the PCSL patterns (in all the experiments) are only used to find the angular origin on the rotor (described by the position of their minima). The change in the shape of these patterns (e.g., between Figures 27 and 28) is generally related to the change in relative vibration between the rotor (motor) and the laser sensor.

4. Discussion

This study presents some of the possibilities available for monitoring the state of a three-phase AC asynchronous induction motor (particularly with a squirrel-cage rotor) running with no load, based mainly on some appropriate methods of computer-aided sampling, definition and analysis of the absorbed IAEPf (and especially VIAEPf). Apart from some interesting but secondary results on the no-load testing of a three-phase AC asynchronous motor (e.g., ESP and CAEPf values, rotation frequency, slip value and start-up time), the essence of this work is focused on the method of extracting the PCRRf patterns from the VIAEPf under different rotor rotation conditions. These patterns are periodic, with a period strictly equal to the period of rotation of the rotor, and can be related to an angular origin on the rotor. It has been demonstrated through various experiments (two different rotational speeds, no DUM and with a DUM placed at different angular positions on the rotor) that the PCRRf patterns found within the IAEPf absorbed by the motor can be considered reliable elements for the synthetic and analytical characterisation of the state of the motor, detected during the no-load tests.

The extraction (recognition) of these patterns is possible because, firstly, a high sampling frequency definition of the IAEPf was proposed based on the removal from the IEP of the fundamental components of 50 Hz (induced by the IV) and 100 Hz components (generated by the IEP definition) and their harmonics. This removal was performed using a BMAF (with h samples on average), where h is the number of samples per IV period. This requires finding the exact mean value of the IV period (and frequency), a problem solved in a similar way in a previous work ([21], available for any periodic signals) and applied

here. There is a second mandatory condition that must be fulfilled for the correct extraction of the PCRRf patterns: the exact determination of the mean value of the rotation period T_p value of the motor rotor with no load. This was carried out using the same method from [21], similar to that used to measure the mean value of the IV period but applied to the u_{SL} signal (generated by a laser sensor and an angular mark placed on the rotor). The PCRRf patterns are extracted from the VIAEPf using the FASS procedure (Equation (3)). This procedure was also used to extract the periodic PCSL patterns within the u_{SL} signal. A PCSL pattern defines (with its minima) the angular reference on the rotor where the PCRRf patterns begin.

Each PCRRf pattern can be described synthetically by the coordinates of its n samples (with time or phase angle on the x -axis and IAEPf on the y -axis) or analytically as a sum of harmonic correlated sinusoidal components. This analytical description was found by curve-fitting procedures applied to the extended synthetic patterns (here over 10 periods) using the Curve Fitting application from MATLAB. An alternative description of the extended patterns (synthetic and analytical) was made in the frequency domain using the FFT spectra (with real amplitudes on the y -axis and frequency on the x -axis).

It should be noted that the shape of the PCRRf patterns must be accepted as conventionally described since a number of their harmonic components are completely removed or severely diminished in amplitude and phase-shifted by the BMAF filter used to extract the IAEPf from the IEP. The filter transmissibility curve (the red one in Figure 5) completely eliminates a number of sinusoidal components from the IEP that are not found in the PCRRf patterns. Those components whose T_c period is described by z samples and whose h/z ratio is strictly an integer are completely eliminated (the transmissibility for these components having $1/T_c$ frequencies and satisfying this condition is zero), e.g., the 3rd harmonic within the pattern PCRRf1a, as shown in Table 2. All other components whose T_c period is described by z samples and which do not satisfy the above condition (with respect to the h/z ratio) have a reduced amplitude at the filter output (greatly reduced when $z < h$). Additionally, some components are affected with a shift of phase of 180 degrees at the time origin.

At the present stage of research, it is practically impossible to determine the description of the sinusoidal components completely removed by BMAF. For sinusoidal components whose amplitudes have been artificially diminished, an attempt has been made to restore the correct amplitude values (by multiplying with the inverse of the transmissibility, $1/Tr(f)$, as a function of frequency). For the components whose phases at the time origin have been changed, their correct phases have been restored by adding 180 degrees. Although the approach is correct in principle, the results of this restoration of correct amplitude and phase values at the time origin are relatively good, as shown in Figure 23 (which shows the results of restoring two different PCRRf1 patterns but determined under the same experimental conditions). If this approach had been correct, the two reworked patterns should have matched better. There is a very simple reason for this partial mismatch: the identification and description of the sinusoidal components (amplitudes, frequencies and phases at the origin of time) of the extended patterns were not performed very accurately. We hope that the use of a better identification method (as a future challenge) will overcome this shortcoming. Despite this relative inconvenience, it is clear that PCRRf patterns are valuable in experimental research, especially for early fault detection.

As a summary of this work, a brief description of the signal processing is given using the flowchart shown in Figure 30. The flowchart also contains some other information (e.g., the equations used, the numerical results and some examples in figures).

It is reasonable to assume that some further studies will confirm the capability and possibly the limitations of these proposed solutions for monitoring the condition of the motor with deliberately introduced mechanical and electrical faults or with different characteristics (e.g., rotor cage shape and structure, number of pole pairs, magnetic field distribution, etc.). It is important to note that some motor faults can be characterised by different variations of the IAEPf over time on each of the three phases of the electrical supply (due to the

asymmetry of their currents). The test bench shown in Figure 2 can be extended with two more ICT transformers and two more IVT transformers (placed on phases B and C), whose output signals can be accessed via four other available oscilloscope input channels. In this way [3,17], it is possible to extract the PCRRf patterns corresponding to the power carried on each of the three phases. These faults can be highlighted by the different appearance of the three PCRRf patterns.

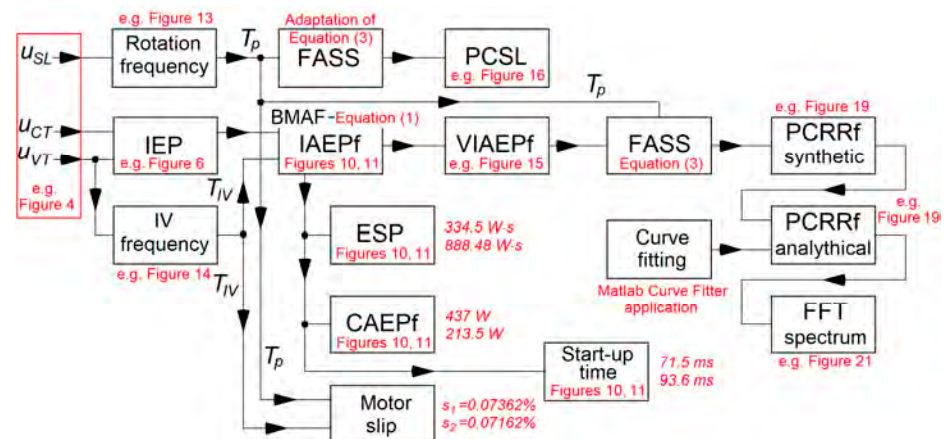


Figure 30. The signals processing flow chart with some additional information.

A future approach will be specifically dedicated to the extraction of PCRRf patterns by FASS within the IAEPf supplied by three-phase AC-AC converters used to motorise the spindle of CNC machines, including those using voltages and currents that are not sinusoidal. Obviously, the subject of motor condition monitoring and diagnostics topic should be reconsidered as being linked to that of the electrical power system [46,47].

This study can be further applied to the identification of patterns within many other experimental signals in stationary regimes (e.g., vibration, surface roughness [48], voltage, current, run out, etc.), the use of these patterns in experimental characterisation of systems state can be an interesting topic.

Author Contributions: Conceptualization, D.-F.C., M.H. and C.-G.M.; methodology, M.H., C.G.D. and N.-E.B.; software, M.H., C.G.D. and F.-D.E.; validation, D.-F.C., N.-E.S. and M.H.; investigation, D.-F.C., M.H., F.-D.E., C.-G.M. and N.-E.B.; resources, C.G.D., D.-F.C. and N.-E.S.; data curation, M.H., C.G.D., C.-G.M. and D.-F.C.; writing—original draft preparation, D.-F.C., M.H., N.-E.B., C.-G.M. and N.-E.S.; writing—review and editing, M.H., D.-F.C., N.-E.B., C.G.D., C.-G.M. and N.-E.S.; supervision and project administration, M.H. and D.-F.C.; funding acquisition, C.G.D. and N.-E.S. All authors have read and agreed to the published version of the manuscript.

Funding: This work was funded by the “National Research Grants—ARUT” programme of the Technical University “Gheorghe Asachi” of Iasi, Romania, project number GnaC2023_269.

Institutional Review Board Statement: Not applicable.

Informed Consent Statement: Not applicable.

Data Availability Statement: The data presented in this paper are available upon request from the corresponding author.

Conflicts of Interest: The authors declare no conflicts of interest.

References

- Wang, Z.; Shi, D.; Xu, Y.; Zhen, D.; Gu, F.; Ball, A.D. Early Rolling Bearing Fault Diagnosis in Induction Motors Based on On-Rotor Sensing Vibrations. *Measurement* **2023**, *222*, 113614. [CrossRef]
- Usman, A.; Rajpurohit, B.S. Condition Monitoring of Permanent Magnet AC Machines for All-Electric Transportation Systems: State of the Art. *IET Energy Syst. Integr.* **2023**, *in press*. [CrossRef]

3. Chang, H.-C.; Jheng, Y.-M.; Kuo, C.-C.; Hsueh, Y.-M. Induction Motors Condition Monitoring System with Fault Diagnosis Using a Hybrid Approach. *Energies* **2019**, *12*, 1471. [\[CrossRef\]](#)
4. Zhang, J.; Wang, P.; Gao, R.S.; Sun, C.; Yan, R. Induction Motor Condition Monitoring for Sustainable Manufacturing. *Procedia Manuf.* **2019**, *33*, 802–809. [\[CrossRef\]](#)
5. Kibrete, F.; Woldemichael, D.E.; Gebremedhen, H.S. Multi-Sensor Data Fusion in Intelligent Fault Diagnosis of Rotating Machines: A Comprehensive Review. *Measurement* **2024**, *232*, 114658. [\[CrossRef\]](#)
6. Kuhn, H.C.; Righi, R.R.; Crovato, C.D.P. On Proposing a Non-Intrusive Device and Methodology to Monitor Motor Degradation. *J. King Saud Univ. Eng. Sci.* **2023**, *35*, 215–223. [\[CrossRef\]](#)
7. Xie, F.; Sun, E.; Zhou, S.; Shang, J.; Wang, Y.; Fan, Q. Research on Three-Phase Asynchronous Motor Fault Diagnosis Based on Multiscale Weibull Dispersion Entropy. *Entropy* **2023**, *25*, 1446. [\[CrossRef\]](#) [\[PubMed\]](#)
8. Gangsar, P.; Tiwari, R. Signal Based Condition Monitoring Techniques for Fault Detection and Diagnosis of Induction Motors: A State-Of-The-Art Review. *Mech. Syst. Signal Process.* **2020**, *144*, 106908. [\[CrossRef\]](#)
9. Yakhni, M.F.; Cauet, S.; Sakout, A.; Assoum, H.; Etien, E.; Rambault, L.; El-Gohary, M. Variable Speed Induction Motors' Fault Detection Based on Transient Motor Current Signatures Analysis: A Review. *Mech. Syst. Signal Process.* **2023**, *184*, 109737. [\[CrossRef\]](#)
10. Esfahani, E.T.; Wang, S.; Sundararajan, V. Multisensor Wireless System for Eccentricity and Bearing Fault Detection in Induction Motors. *IEEE/ASME Trans. Mechatron.* **2014**, *19*, 818–826. [\[CrossRef\]](#)
11. Wang, X.; Li, A.; Han, G.A. Deep-Learning-Based Fault Diagnosis Method of Industrial Bearings Using Multi-Source Information. *Appl. Sci.* **2023**, *13*, 933. [\[CrossRef\]](#)
12. Li, W.; Mechefske, C.K. Detection of Induction Motor Faults: A Comparison of Stator Current, Vibration and Acoustic Methods. *J. Vib. Control* **2006**, *12*, 165–188. [\[CrossRef\]](#)
13. Seera, M.; Lim, C.P.; Nahavandi, S.; Loo, C.K. Condition Monitoring of Induction Motors: A Review and an Application of an Ensemble of Hybrid Intelligent Models. *Expert. Syst. Appl.* **2014**, *41*, 4891–4903. [\[CrossRef\]](#)
14. Garcia-Calva, T.; Morinigo-Sotelo, D.; Fernandez-Cavero, V.; Romero-Troncoso, R. Early Detection of Faults in Induction Motors-A Review. *Energies* **2022**, *15*, 7855. [\[CrossRef\]](#)
15. Juez-Gil, M.; Saucedo-Dorantes, J.S.; Arnaiz-González, A.; López-Nozal, C.; García-Osorio, C.; Lowe, D. Early and Extremely Early Multi-Label Fault Diagnosis in Induction Motors. *ISA Trans.* **2020**, *106*, 367–381. [\[CrossRef\]](#) [\[PubMed\]](#)
16. Kalel, D.; Singh, R.R. Iot Integrated Adaptive Fault Tolerant Control for Induction Motor Based Critical Load Applications. *Eng. Sci. Technol. Int. J.* **2024**, *51*, 101585. [\[CrossRef\]](#)
17. Chang, H.-C.; Jheng, Y.-M.; Kuo, C.-C.; Huang, L.-B. On-Line Motor Condition Monitoring System for Abnormality Detection. *Comput. Electr. Eng.* **2016**, *51*, 255–269. [\[CrossRef\]](#)
18. Gultekin, M.A.; Bazzi, A. Review of Fault Detection and Diagnosis Techniques for AC Motor Drives. *Energies* **2023**, *16*, 5602. [\[CrossRef\]](#)
19. Zeng, H.; Xu, J.; Yu, C.; Li, Z.; Zhang, Q.; Li, W. Analysis of Equivalent Inertia of Induction Motors and Its Influencing Factors. *Electr. Pow. Syst. Res.* **2023**, *225*, 109820. [\[CrossRef\]](#)
20. Ebrahimi, B.M.; Etemadrezai, M.; Faiz, J. Dynamic Eccentricity Fault Diagnosis in Round Rotor Synchronous Motors. *Energy Convers. Manag.* **2011**, *52*, 2092–2097. [\[CrossRef\]](#)
21. Horodincu, M.; Ciurdea, I.; Chitariu, D.; Munteanu, A.; Boca, M. Some Approaches on Instantaneous Angular Speed Measurement Using a Two-phase n Poles AC Generator as Sensor. *Measurement* **2020**, *157*, 107636. [\[CrossRef\]](#)
22. AlShorman, O.; Irfan, M.; Abdelrahman, R.B.; Masadeh, M.; Alshorman, A.; Shekh, M.A.; Saad, N.; Rahman, S. Advancements in Condition Monitoring and Fault Diagnosis of Rotating Machinery: A Comprehensive Review of Image-Based Intelligent Techniques for Induction Motors. *Eng. Appl. Artif. Intell.* **2024**, *130*, 107724. [\[CrossRef\]](#)
23. Bieler, G.; Werneck, M.M. A Magnetostrictive-Fiber Bragg Grating Sensor for Induction Motor Health Monitoring. *Measurement* **2018**, *122*, 117–127. [\[CrossRef\]](#)
24. Zamudio-Ramirez, I.; Osornio-Rios, R.; Antonino-Daviu, J.A. Smart Sensor for Fault Detection in Induction Motors Based on the Combined Analysis of Stray-Flux and Current Signals: A Flexible, Robust Approach. *IEEE Ind. Appl. Mag.* **2022**, *28*, 56–66. [\[CrossRef\]](#)
25. Irfan, M.; Saad, N.; Ibrahim, R.; Asirvadam, V.S. An On-line Condition Monitoring System for Induction Motors via Instantaneous Power Analysis. *J. Mech. Sci. Technol.* **2015**, *29*, 1483–1492. [\[CrossRef\]](#)
26. Choudhary, A.; Goyal, D.; Shimi, S.L.; Akula, A. Condition Monitoring and Fault Diagnosis of Induction Motors: A Review. *Arch. Comput. Methods Eng.* **2019**, *26*, 1221–1238. [\[CrossRef\]](#)
27. Almounajjed, A.; Sahoo, A.K.; Kumar, M.K. Diagnosis of Stator Fault Severity in Induction Motor Based on Discrete Wavelet Analysis. *Measurement* **2021**, *182*, 109780. [\[CrossRef\]](#)
28. Benamira, N.; Dekhane, A.; Kerfali, S.; Bouras, A.; Reffas, O. Experimental Investigation of The Combined Fault: Mechanical and Electrical Unbalances in Induction Motors Based on Stator Currents Monitoring. *Instrum. Mes. Metrol.* **2022**, *21*, 207–215. [\[CrossRef\]](#)
29. Zhang, T.; Chen, J.; Li, F.; Zhang, K.; Lv, H.; He, S.; Xu, E. Intelligent Fault Diagnosis of Machines with Small & Imbalanced Data: A State-Of-The-Art Review and Possible Extensions. *ISA Trans.* **2022**, *119*, 152–171. [\[CrossRef\]](#) [\[PubMed\]](#)

30. Trujillo Guajardo, L.A.; Platas Garza, M.A.; Rodríguez Maldonado, J.; González Vázquez, M.A.; Rodríguez Alfaro, L.H.; Salinas Salinas, F. Prony Method Estimation for Motor Current Signal Analysis Diagnostics in Rotor Cage Induction Motors. *Energies* **2022**, *15*, 3513. [CrossRef]
31. Triyono, B.; Prasetyo, Y.; Winarno, B.; Wicaksono, H.H. Electrical Motor Interference Monitoring Based on Current Characteristics. *J. Phys. Conf. Ser.* **2021**, *1845*, 012044. [CrossRef]
32. Zamudio-Ramírez, I.; Osornio-Ríos, R.A.; Antonino-Daviu, J.A. Triaxial Smart Sensor Based on the Advanced Analysis of Stray Flux and Currents for the Reliable Fault Detection in Induction Motors. In Proceedings of the 12th Annual IEEE Energy Conversion Congress and Exposition (IEEE ECCE), Detroit, MI, USA, 23 September–15 October 2020.
33. Matsushita, M.; Kameyama, H.; Ikeboh, Y.; Morimoto, S. Sine-Wave Drive for PM Motor Controlling Phase Difference Between Voltage and Current by Detecting Inverter Bus Current. *IEEE Trans. Ind. Appl.* **2009**, *45*, 1294–1300. [CrossRef]
34. Irfan, M.; Saad, N.; Ibrahim, R.; Asirvadam, V.S. Condition monitoring of induction motors via instantaneous power analysis. *J. Intell. Manuf.* **2017**, *28*, 1259–1267. [CrossRef]
35. Azzoug, Y.; Sahraoui, M.; Pusca, R.; Ameid, T.; Romary, R.; Cardoso, A.J.M. Current Sensors Fault Detection and Tolerant Control Strategy for Three-phase Induction Motor Drives. *Electr. Eng.* **2021**, *103*, 881–898. [CrossRef]
36. Dianov, A.; Anuchin, A. Phase Loss Detection Using Voltage Signals and Motor Models: A Review. *IEEE Sens. J.* **2021**, *21*, 26488–26502. [CrossRef]
37. Konar, P.; Chattopadhyay, P. Multi-class fault diagnosis of induction motor using Hilbert and Wavelet Transform. *Appl. Soft. Comput.* **2015**, *30*, 341–352. [CrossRef]
38. Irgat, E.; Çinar, E.; Ünsal, A.; Açensal, A.; Yazici, A. An IoT-Based Monitoring System for Induction Motor Faults Utilizing Deep Learning Models. *J. Vib. Eng. Technol.* **2023**, *11*, 3579–3589. [CrossRef]
39. Liu, Y.; Bazzi, A.M. A Review and Comparison of Fault Detection and Diagnosis Methods for Squirrel-Cage Induction Motors: State of the Art. *ISA Trans.* **2017**, *70*, 400–409. [CrossRef] [PubMed]
40. Liang, B.; Iwnicki, S.D.; Zhao, Y. Application of Power Spectrum, Cepstrum, Higher Order Spectrum and Neural Network Analyses for Induction Motor Fault Diagnosis. *Mech. Syst. Signal Process.* **2013**, *39*, 342–360. [CrossRef]
41. Wieser, R.S.; Kral, C.; Pirker, F.; Schagginger, M. The Vienna induction machine Monitoring Method; On the impact of the Field Oriented Control structure on real operational behaviour of a faulty machine. In Proceedings of the 24th Annual Conference of the IEEE Industrial-Electronics-Society, Aachen, Germany, 31 August–4 September 1998.
42. Horodincă, M.; Bumbu, N.-E.; Chitariu, D.-F.; Munteanu, A.; Dumitras, C.-G.; Negoescu, F.; Mihai, C.-G. On the Behaviour of an AC Induction Motor as Sensor for Condition Monitoring of Driven Rotary Machines. *Sensors* **2023**, *23*, 488. [CrossRef] [PubMed]
43. PicoScope® 4000A Series. High-Resolution Deep-Memory Oscilloscopes (Pico Technology, UK). Available online: <https://www.picotech.com/oscilloscope/4000/picoscope-4000-specifications> (accessed on 29 June 2024).
44. Sowidan, H. ECE 330 Power Circuits and Electromechanics. Lecture 2: Active, Reactive, and Complex Power. Available online: <https://courses.engr.illinois.edu/ece330/fa2017/lectures/Lecture%202.pdf> (accessed on 29 June 2024).
45. Bumbu, N.E.; Horodincă, M. A Study on the Dynamics of an AC Induction Motor Rotor Based on the Analysis of Free Response at Impulse Excitation. *Bull. Polytech. Inst. Iași Mach. Constr. Sect.* **2022**, *68*, 57–74. [CrossRef]
46. Yao, B.; Zhang, Y.; Correia, P.; Wu, R.; Song, S.; Trintis, I.; Wang, H.; Wang, H. Accelerated Degradation Testing and Failure Mechanism Analysis of Metallized Film Capacitors for AC Filtering. *IEEE Trans. Power Electron.* **2024**, *39*, 6256–6270. [CrossRef]
47. Lin, H.; Lin, C.; Xie, D.; Acuna, P.; Liu, W. A Counter-Based Open-Circuit Switch Fault Diagnostic Method for a Single-Phase Cascaded H-Bridge Multilevel Converter. *IEEE Trans. Power Electron.* **2024**, *39*, 814–825. [CrossRef]
48. Horodincă, M.; Chifan, F.; Paduraru, E.; Dumitras, C.G.; Munteanu, A.; Chitariu, D.-F. A Study of 2D Roughness Periodical Profiles on a Flat Surface Generated by Milling with a Ball Nose End Mill. *Materials* **2024**, *17*, 1425. [CrossRef] [PubMed]

Disclaimer/Publisher’s Note: The statements, opinions and data contained in all publications are solely those of the individual author(s) and contributor(s) and not of MDPI and/or the editor(s). MDPI and/or the editor(s) disclaim responsibility for any injury to people or property resulting from any ideas, methods, instructions or products referred to in the content.

Article

An Assessment of the Mechanical Deformation Behavior of Three Different Clear Aligner Materials: A Digital Image Correlation Analysis

Nicolae Daniel Olteanu ¹, Camelia Szuhaneck ^{2,*}, Sorana Nicoleta Rosu ^{1,*}, Dragos Florin Chitariu ³, Nicolae Seghedin ³, Tinela Panaite ¹, Amalia Casalean ² and Irina Nicoleta Zetu ¹

- ¹ Department of Oral and Maxillofacial Surgery, Faculty of Dental Medicine, “Grigore T. Popa” University of Medicine and Pharmacy from Iasi, 16 Universitatii Str., 700115 Iasi, Romania; daniel.olteanu@umfiasi.ro (N.D.O.); tinela-panaite@umfiasi.ro (T.P.); irina.zetu@umfiasi.ro (I.N.Z.)
- ² Ortho-Center Research Center, Department of Orthodontics, Faculty of Dental Medicine, “Victor Babes” University of Medicine and Pharmacy Timisoara, 9 No., Revolutiei Bv., 300041 Timisoara, Romania; amalia.casalean@yahoo.com
- ³ Faculty of Machine Manufacturing and Industrial Management, “Gheorghe Asachi” Technical University of Iasi, 700050 Iasi, Romania; dragos-florin.chitariu@academic.tuiasi.ro (D.F.C.); nsegshed2003@yahoo.com (N.S.)
- * Correspondence: cameliaszuhaneck@umft.ro (C.S.); soranarosu@gmail.com (S.N.R.); Tel.: +40-757070891 (S.N.R.)

Abstract: **Introduction:** The present study aimed to investigate the deformation behavior of three different clear aligner systems, CA[®] Pro+ Clear Aligner (Scheu Dental, Iserlohn, Germany), Taglus Premium (Taglus Company, Mumbai, India), and Spark Trugen (Ormco Corp., Orange, CA, USA), under compression testing, using the digital image correlation (DIC) technique. **Materials and Methods:** A total of 15 patients were treated with each of the three aligner systems, resulting in 45 sets of aligners. Each aligner set was fixed on the 3D-printed dental arches and then in an articulator. Then, the samples were subjected to occlusal forces using a purpose-built test stand to allow for controlled force application and precise displacement determination. The DIC technique was used for capturing the deformation behavior, providing detailed strain and displacement fields. Statistical analysis was performed using one-way ANOVA and Bonferroni post hoc tests with a significance of 0.05. **Results:** The results indicate that the Spark system exhibited the most substantial rigid displacement. Furthermore, the elastic deformation values of the Spark and Taglus systems were significantly higher than those of the CA Pro+ system ($p > 0.05$). **Conclusions:** The Spark Trugen clear aligner system demonstrated a lower stability to rigid displacement and elastic deformation under compression testing compared to the Scheu CA[®] Pro+ Clear Aligner and Taglus Premium. All three tested clear aligner systems showed an increased resistance to elastic displacement and rigid deformation in the mandibular arch.

Keywords: clear aligner; elastic deformation; rigid displacement; digital image correlation



Citation: Olteanu, N.D.; Szuhaneck, C.; Rosu, S.N.; Chitariu, D.F.; Seghedin, N.; Panaite, T.; Casalean, A.; Zetu, I.N. An Assessment of the Mechanical Deformation Behavior of Three Different Clear Aligner Materials: A Digital Image Correlation Analysis. *Appl. Sci.* **2024**, *14*, 7496. <https://doi.org/10.3390/app14177496>

Academic Editors: Simone Parrini, Gabriele Rossini and Andrea Deregibus

Received: 31 July 2024

Revised: 21 August 2024

Accepted: 22 August 2024

Published: 24 August 2024



Copyright: © 2024 by the authors. Licensee MDPI, Basel, Switzerland. This article is an open access article distributed under the terms and conditions of the Creative Commons Attribution (CC BY) license (<https://creativecommons.org/licenses/by/4.0/>).

1. Introduction

In recent years, clear aligners have revolutionized the field of orthodontics, providing an aesthetically pleasing and comfortable alternative to traditional braces. However, understanding the mechanical deformation behavior of aligners is crucial for optimizing their design and performance [1].

Clear aligners, typically made from thermoplastic polymers, work by applying controlled forces to teeth, gradually moving them into the desired position [2]. Unlike braces, aligners are removable and nearly invisible, which has contributed to their growing popularity. Despite their advantages, the success of aligners hinges on their mechanical behavior, particularly their ability to withstand deformation while delivering consistent forces over the treatment period [1,2].

Clear aligner treatment requires periodic refinements which are undesirable, costly, and unrecyclable. One of the reasons for refinements is the material from which the aligner is made. Polyethylene terephthalate glycol (PET-G) is currently the most widely used clear aligner material [3]. Polymers with shape memory properties for direct 3D printing, such as TC-85, a photocurable resin, have been proposed as new clear aligner materials [4]. New aligner materials seek to apply a constant force over a considerable period of time, with increased elasticity, strength, and transparency, and a more precise fit [1]. However, the force exerted by clear aligners decreases in 1–3 days due to the stress relaxation of the viscoelastic aligner materials. Clear aligners deform and wear in spots where attachments are fixed [3,5]. Temperature, oral functional and parafunctional forces induced by chewing, talking, drinking, swallowing, bruxism, and unilateral mastication may also modify the mechanical behavior of aligner materials [6]. Aligners made of the same material but printed on different 3D printers show significantly different mechanical properties [7].

The most suitable mechanical properties of aligner materials are characterized by stiffness, high yield strength, and a flat relaxation curve with low-stress relaxation levels [8]. Aligners with high stiffness are difficult to insert and remove, whereas aligners with decreased elasticity may not provide the force necessary to move teeth [9]. The initial removal of clear aligners is believed to make the material return to its initial shape and become wider transversally and shorter longitudinally [10].

The following finite element analysis and experimental methods were used for studying the mechanical behavior and the forces exerted by clear aligner materials [11], expressed as measurements of elasticity, strength, stiffness, and shape memory: the three-point bending test [3], compression tests such as tensile yield stress, stress relaxation, creep recovery, elastic modulus, and Young's modulus tests [4,8,9], Martens hardness test, instrumented indentation testing [12], the U-shape bending test and the shape recovery ratio [4], von Mises stress distribution in Finite Element Analysis (FEA)/Finite Element Modeling (FEM) [10,11,13], the RSA3 Dynamic Mechanical Analyzer (Texas Instruments, Dallas), and the INSTRON Universal Testing System (Instron Corp, Wilmington/Norwood) [8,9]. Clear aligner wear expressed as microcracks, abrasion, and changes in clear aligner thickness were assessed by scanning electron microscopy, energy dispersive X-ray microanalysis, 3D models of clear aligners at different reference occlusal points, and the software Geomagic Qualify 2013 (3D Systems, Rock Hill, SC, USA). The behavior of the materials used in dentistry can also be assessed by the DIC (Digital Image Correlation) technique, which consists of a contact-free optical method for measuring deformations, motions, and changes in the shape of object surfaces [6].

The aim of the present study was to assess the deformation behavior of three different aligner systems—CA[®] Pro+ Clear Aligner (Scheu Dental, Iserlohn, Germany), Taglus Premium (Taglus Company, Mumbai, India), and Spark Trugen (Ormco Corp., Orange, CA, USA)—through a compression method by the digital image correlation (DIC) technique. The null hypothesis states that no differences in deformation behavior are recorded between the three aligner systems.

2. Materials and Methods

The study was conducted in accordance with the requirements of the Declaration of Helsinki and the rules imposed by the Research Ethics Committee of “Grigore T. Popa” University of Medicine and Pharmacy of Iasi, Romania (approval no. 56/12.03.2021). In addition, the patients were informed and consented to participate in the study by signing an informed consent.

2.1. Sample Preparation

The sample size was calculated using G*Power software version 3.1 (Heinrich-Heine University, Dusseldorf, Germany) with an alpha error of 0.05, an effect size of 0.5, and a power of the study of 0.8. The recommended minimum number of samples to be used in the study was 42.

The present study was conducted on a total of 15 patients, aged between 20 and 30 years, who came to the Pediatric Dentistry clinic, Orthodontics Department of “Grigore T. Popa” University of Medicine and Pharmacy, with an orthodontic diagnosis of dento-maxillary disharmony of Angle class I with crowding. After the clinical examination, diagnosis, and indication for orthodontic treatment with aligners, each of the 15 patients was fitted with a pair of aligners (upper and lower jaws) from each of the three tested systems. Therefore, the resulting total number of 45 pairs of study samples were divided into 3 groups corresponding to the used aligner system. The distribution of the samples and the material compositions are presented in Table 1.

Table 1. Distribution of the samples and the material compositions.

Group	Aligner System	Manufacturer	Composition and Material Thickness
CA (n = 15)	CA [®] Pro+ Clear Aligner	Scheu Dental, Iserlohn, Germany	Three layers (0.75 mm): 1. Copolyester layer (0.25 mm) 2. Thermoplastic elastomer (TPE) (0.25 mm) 3. Copolyester layer (0.25 mm)
TG (n = 15)	Taglus Premium	Taglus Company, Mumbai, India	Polyethylene terephthalate glycol (PET-G) (0.75 mm)
SP (n = 15)	Spark Trugen	Ormco Corp., Orange, CA, USA	TruGEN Technology (0.75 mm)

The design of a clear aligner started with a digital dental record performed with a dedicated intraoral scan (MEDIT- I 500 scanner, Medit Corp., Seoul, Republic of Korea). The scan was then processed by the 3Shape OrthoAnalyzer[®] software (TRIOS-3Shape, Copenhagen, Denmark) or Approver (Spark ORMCO, Ormco Corp., Orange, CA, USA), which provided an accurate 3D reconstruction of the teeth and allowed for the 3D Setup to be performed. During this step, the orthodontist and the dental technician planned the dental movement and the final result. The virtual 3D reconstruction allowed them to print a resin cast and then thermoform and process the aligner materials accordingly.

2.2. Deformation Behavior Testing

To investigate the deformation behavior, the clear aligners were subjected to occlusal forces using a purpose-made test stand developed in order to allow for controlled force application and to precisely determine the displacements of the aligners. The present study evaluated the following three different aligner materials and systems: CA[®] Pro+ Clear Aligner (Scheu Dental, Iserlohn, Germany), Taglus Premium (Taglus Company, Mumbai, India), and Spark Trugen (Ormco Corp., Orange, CA, USA).

The clear aligners were placed on 3D-printed dental arches, which in turn were fixed on hard resin dental casts that were fixed in a dental articulator. Thus, the mechanical hinged fixture could simulate the bite closure movement.

The lower part of the articulator (the lower jaw) was rigidly fixed on the base plate of the stand. In order to use the digital image correlation (DIC) method, markers were placed on the gingival and incisal part of the aligner for the upper and lower incisors as well as for lower incisors and canines on the frontal plane of the aligners (Figure 1).

The loading force of up to 500 N was applied, equivalent to the human biting force, the maximum molar occlusal force. Muscle activity during chewing was assessed to be normal during clear aligner use. The average magnitude of the biting force of a human is nearly 500 N [13]. The forces were measured directly using a S9 force transducer (produced by Hottinger Baldwin Messtechnik, HBM GmbH, Darmstadt, Germany) placed directly on the upper hard resin dental cast model. Force data acquisition was performed by Spider 8 PC measurement electronics (produced by Hottinger Baldwin Messtechnik, HBM GmbH, Darmstadt, Germany) linked to a PC running a Catman Easy/AP software version 2.2.

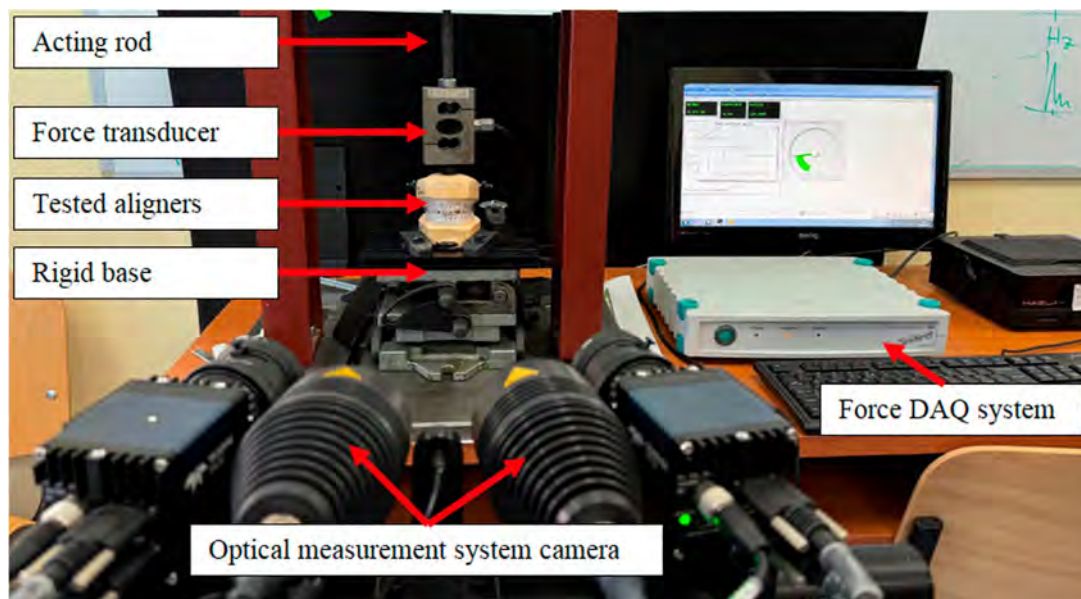


Figure 1. Overview of the experimental setup used for the assessment of the deformation behavior of clear aligners.

The deformation behavior of the materials was assessed using a digital image correlation (DIC) system. This is a contactless and non-destructive measurement technique that can compute 2D or 3D coordinates from an image series recorded with a stereo camera. By interpreting local displacements between the 2D or 3D coordinates, strain values and strain rates can be calculated. The DIC method uses reference images captured by the left and the right camera to determine the 3D coordinates of various points that will be analyzed, by subtracting the 3D coordinates from all recorded stages over time from the 3D coordinates of the reference stage which led to 3D displacement values. Before carrying out the measurements, the calibration procedure was performed in order for the possible measurement errors to remain low.

The measurement of the displacements and deformations was performed through the DIC system ARAMIS 3D 12M Camera (Carl Zeiss, Jena, Germany) running the PONTOS software version v6.3.1-1 (PONTOS Software GmbH, Jena, Germany). PONTOS Live is based on the triangulation principle and analyses components of different sizes—from a few millimeters to a few meters—point by point, regardless of the material. The DIC hardware system parameters are presented in Table 2.

Considering the field of view, calibration was performed, resulting in a measuring area of $420 \times 330 \times 300$ mm. The software was able to provide the average value of the 3D coordinates (X, Y and Z) of each tracker placed, and further 3D displacements could then be calculated.

The deformation of each of the three aligner materials was measured using trackers placed in the same points. In our research, each of the three aligner materials was tested on the same test stand and using the same load value. The 3D displacements were measured during loading, and the rigid displacements and elastic deformation on each axis were determined.

Table 2. DIC hardware parameters.

Camera Sensor	CMOS
Camera Resolution	4096 × 3000 pixels
Frame Rate	25 fps @ full resolution 43 fps @ 2496 × 2096 pixels (5M mode)
Illumination	Light Projector Tracking Spots
Measuring Area [mm]	Frame 150: 35 70 120 180 Frame 300: 110 170 260 400 550 Frame 600: 750 1500 Frame 1200: 1500 3000 Frame 1600: 5000
Control Device	ARAMIS Controller
Sensor Size [mm]	Frame 150: approx. 260 × 330 × 300 Frame 300: approx. 420 × 330 × 300 Frame 600: approx. 730 × 230 × 130 Frame 1200: approx. 1300 × 230 × 130 Frame 1600: approx. 1700 × 230 × 130
Strain Measuring Range	0.005% up to >2000%
Strain Measuring Resolution	up to 0.005%

2.3. Statistical Analysis

For statistical analysis, the IBM SPSS Software (SPSS Inc., Chicago, IL, USA) version 29.0.0 was used. The normality of data distribution was assessed using the Shapiro–Wilk test and the homogeneity of variances was evaluated by Levene’s test. Statistical analysis of data was performed by one-way ANOVA and Bonferroni post hoc tests. The significance level was set at 0.05.

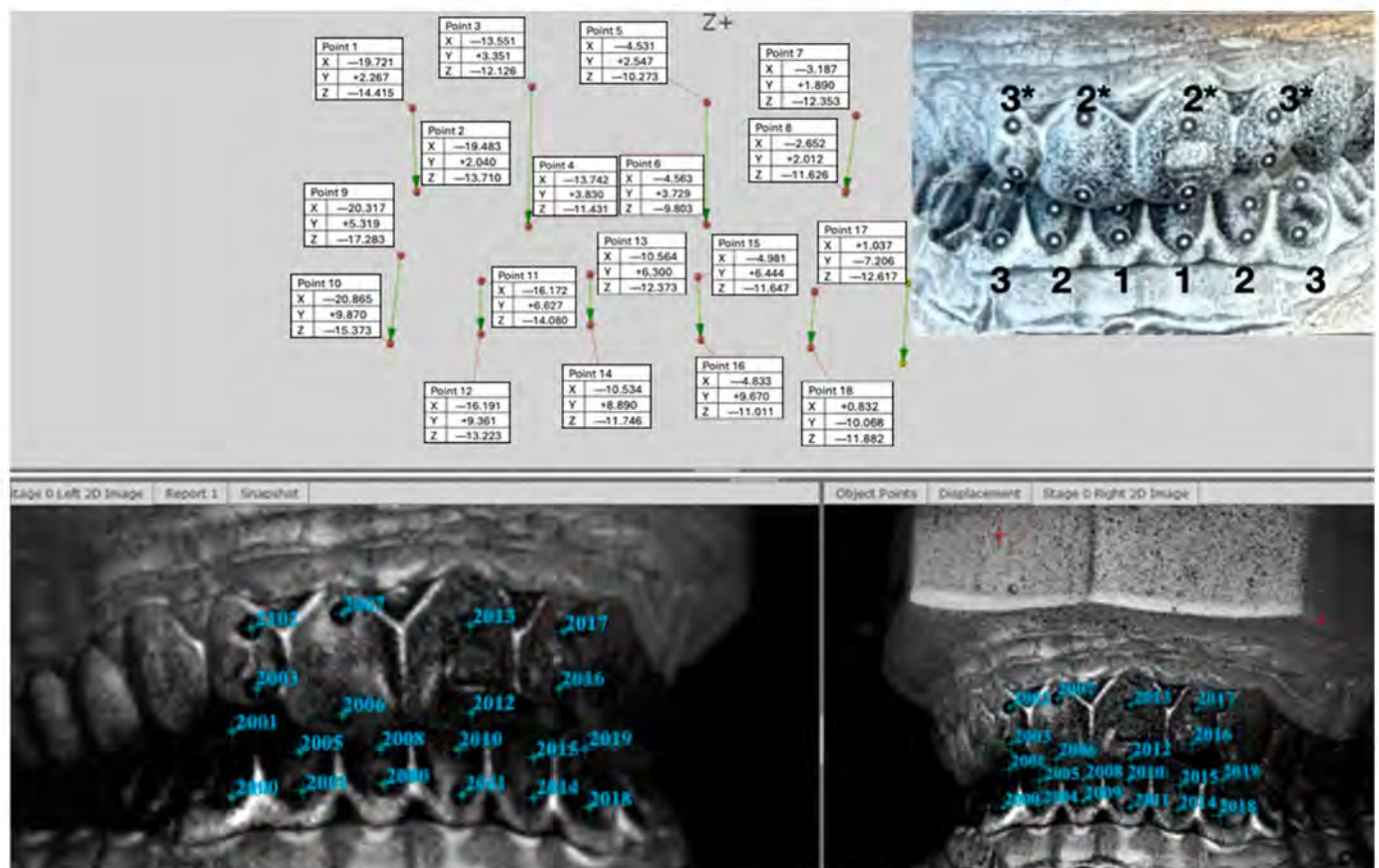
3. Results

In Figure 2, there is a captured image that illustrates the 3D coordinates of each tracker placed on aligners, on the upper and lower arches.

The mean displacement values of the upper and lower arches for each of the tested aligners are presented in Table 2. The mean values were obtained considering the values of the coordinates of each axis from the reference stage and final loading stage, for each tooth and each arch.

In Figure 3, it can be observed that the highest mean values for each axis were recorded by the samples in group SP. For axis X, the highest mean value was 0.264 ± 0.068 mm; for axis Y, it was 0.840 ± 0.106 mm; and for axis Z, it was 0.239 ± 0.068 mm.

When analyzing the differences between the study groups for axis X, we recorded statistically significant differences between groups CA vs. SP ($p = 0.00$); TG vs. SP ($p = 0.00$) and CA vs. TG ($p = 0.031$). For axis Y, significant differences were observed between groups CA vs. SP ($p = 0.00$); TG vs. SP ($p = 0.00$). For axis Z, statistical significance was recorded between groups CA vs. SP ($p = 0.00$); CA vs. TG ($p = 0.00$) and TG vs. SP ($p = 0.00$).



* indicates the maxillary points

Figure 2. Captured image of the 3D coordinates of each tracker placed on aligners.

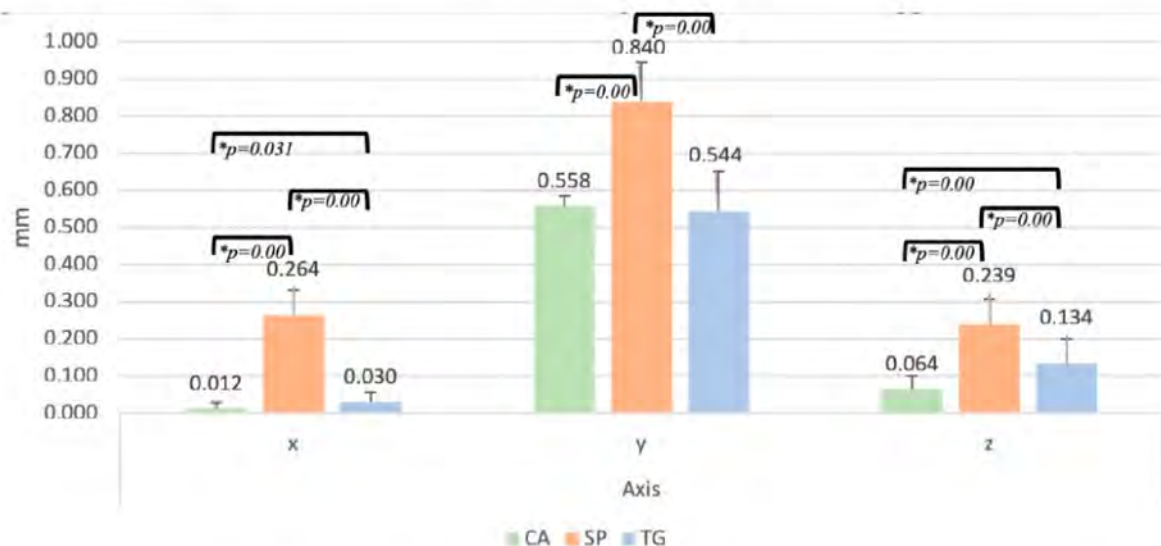


Figure 3. Mean values and standard deviations of rigid displacement for upper arch. * Statistically significant differences between groups are indicated by black line.

In Figure 4, it can be observed that the highest mean values for each axis was recorded by the samples in group SP. For axis X, the highest mean value was 0.252 ± 0.077 mm; for axis Y, it was 0.371 ± 0.047 mm; and for axis Z, it was 0.134 ± 0.097 mm.

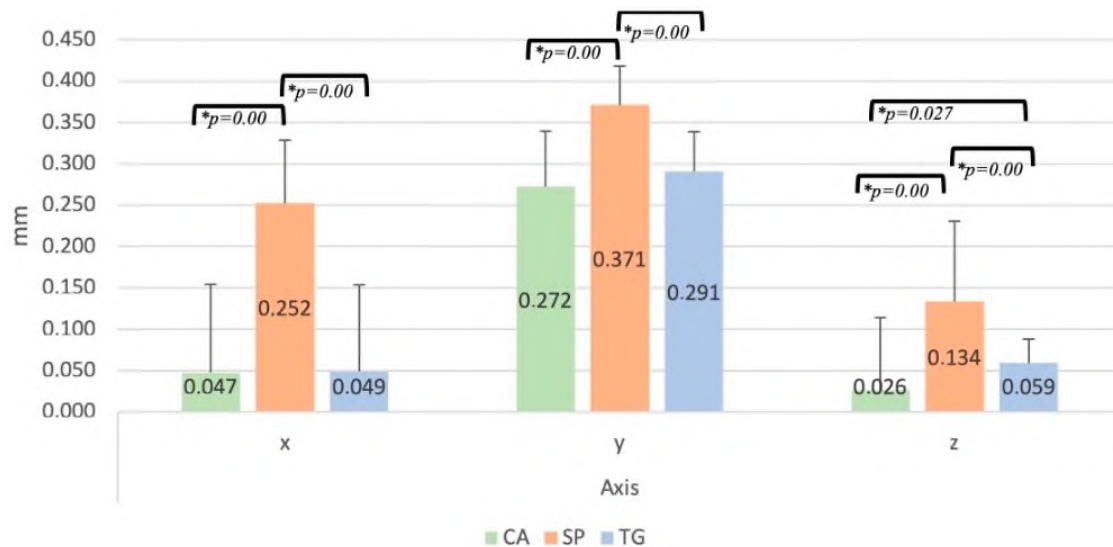


Figure 4. Mean values and standard deviations of rigid displacement for lower arch. * Statistically significant differences between groups are indicated by the black line.

The statistical analysis of the mean values of the rigid displacement for the lower arch showed significant differences within axis X between groups CA vs. SP ($p = 0.00$) and SP vs. TG ($p = 0.00$). For axis Y, differences were recorded between groups CA vs. SP ($p = 0.00$) and SP vs. TG ($p = 0.00$). Within the mean values recorded for axis Z, statistically significant differences were observed for CA vs. SP ($p = 0.00$); TG vs. SP ($p = 0.00$) and CA vs. TG ($p = 0.027$).

Tables 3–5 represent the mean values of the elastic deformation for each of the three tested materials, determined as the difference between the position of the gingival and the incisal tracker on the same tooth. Tables 3–5 show the mean values recorded by each material on each axis, for each of the two arches, at each marked point. Comparative statistical analysis of the obtained values for the elastic deformation showed that, for the maxillary arch, significant differences were observed between the values recorded for the X-axis by the CA vs. SP group ($p = 0.00$) and the CA vs. TG group with a $p = 0.00$ value. There were no significant differences between the SP and TG groups ($p > 0.05$). For the Z-axis, the CA group showed significantly higher values compared to the SP group.

Table 3. Elastic deformation determined as the difference between the position of the gingival and the incisal tracker on the same tooth for SCHEU CA® Pro+ material.

Aligner	No. Point	3 *	2 *	1	2 *	3 *	
Scheu Upper	Axis	[mm]	[mm]	[mm]	[mm]	[mm]	
	X	0.023	0.011		0.016	0.023	
	Y	0.002	0.005		0.006	0.001	
	Z	0.009	0.054		0.033	0.001	
Scheu Lower		3	2	1	1	2	3
	X	0.007	0.007	0.002	0.003	0.006	0.013
	Y	0.003	0.003	0.003	0.002	0.001	0.002
	Z	0.017	0.017	0.01	0.017	0.014	0.003

* indicates the maxillary points.

Table 4. Elastic deformation determined as the difference between the position of the gingival and the incisal tracker on the same tooth for Spark Trugen Material.

Aligner	No. Point	3 *	2 *	1	2 *	3 *	
Spark Upper	Axis	[mm]	[mm]	[mm]	[mm]	[mm]	
	X	0.007	0.008	-	0.033	0.034	
	Y	0.007	0.003	-	0.01	0.02	
	Z	0.005	0.05	-	0.024	0.027	
Spark Lower		3	2	1	1	2	3
	X	0.01	0.002	0.0015	0.014	0.014	0.002
	Y	0.001	0	0.006	0.008	0.006	0.007
	Z	0.011	0.009	0.0015	0.021	0.027	0.03

* indicates the maxillary points.

Table 5. Elastic deformation determined as the difference between the position of the gingival and the incisal tracker on the same tooth for Taglus Premium material.

Aligner	No. Point	3 *	2 *	1	2 *	3 *	
Taglus Upper	Axis	[mm]	[mm]	[mm]	[mm]	[mm]	
	X	0.002	0.008		0.019	0.044	
	Y	0.005	0.016		0.01	0.009	
	Z	0.024	0.053		0.026	0.026	
Taglus Lower		3	2	1	1	2	3
	X	0.002	0.008	0.002	0.004	0.009	0.002
	Y	0.001	0.01	0.005	0.006	0.003	0.007
	Z	0.01	0.048	0.017	0.02	0.018	0.03

* indicates the maxillary points.

For the mandibular arch, the SP and TG groups showed significantly higher Z-axis values compared to the CA group.

4. Discussion

The deformation behavior of clear aligner systems is a critical aspect of orthodontic treatment, impacting the efficacy and comfort of aligners. The present study aimed to investigate the deformation behavior of three different aligner systems—CA[®] Pro+ Clear Aligner (Scheu Dental, Iserlohn, Germany), Taglus Premium (Taglus Company, Mumbai, India), and Spark Trugen (Ormco Corp., Orange, CA, USA)—under compression, using the digital image correlation (DIC) technique. The null hypothesis posited that no significant differences in deformation behavior would be recorded among these systems.

A study conducted by Casavola et al. investigated the mechanical behavior of PET-G-based aligners using DIC under compression testing [14]. The study found that the DIC technique efficiently captured the deformation phases of the material, providing detailed information on the response of the aligners to mechanical loads. This study supported the use of DIC in evaluating the mechanical behavior of aligners thus motivating our approach. Another research explored the use of DIC to measure the displacement and deformation of aligners during orthodontic treatment [15]. The study confirmed that the DIC technique has demonstrated its effectiveness in capturing the mechanical behavior of aligners, highlighting the distribution of displacement and deformation. A study conducted by Kibitkin also used the two-dimensional DIC technique to characterize the deformation behavior of aligners materials [16]. This study highlighted the ability of

DIC to clearly delineate the phases of compressive behavior. The findings of this study are in full agreement with our results on the significant elastic deformation observed in the Spark and Taglus systems.

Images obtained with a high-speed camera have the advantage of a precise measurement of the elastic volume changes [11]. The thickness of the aligner material impacts the force that it generates. The different thickness of the studied aligners was taken into account. ASTM D882-18 and the ISO standard 527 recommend rectangular shapes for tensile testing in thermoplastic materials with a thickness of less than 1 mm [11,17], which also applies to Duran, with a thickness of 0.75 mm. The thickness of clear aligners varies in different teeth, such as the incisors, molars, and in the edentulous areas. 3D printing aligner manufacturing decreases the variation in thickness, leading to more predictable clear aligner treatment outcomes [4,18].

In PET-G materials, such as Taglus Premium, the residual static force and strain recovery rate remain relatively constant even after repeated cyclic loads [4,19], but there is a loss in the ability to exert constant force over a week of use. By applying a cyclic compression of up to 13,000 load cycles from 0 to 50 N, the estimated load to which an aligner is subjected for one week, wear, tear, high depressions, and cracks leading to a loss of force were recorded by digital image correlation and optical microscope analysis in 0.75 mm thick PET-G aligners, at higher levels than in the 0.88 mm thick sample [14,20].

Thermoformed aligners made of the thermo-plastic material Duran showed excessive irreversible deformation during plastic deformation with load application. The displacements were between 1.5 and 2.5 mm for the Duran thermoformed aligners, and the maximum load resistance was found to be almost 200 N [13]. Duran was shown to have a low stress value of 0.5 MPa and a low percentage of normalized stress of 4.6% on a three-point bending test after 14 days of constant deflection. A great decay was also found, with the initial values of 20 MPa being followed by values ranging between 12 MPa and 4 MPa in the 24 h stress relaxation tests [3]. In the Duran materials undergoing ISO527-1 tensile testing, thermoforming caused an increase in yield stress and elastic modulus, a measurement of stiffness, whereas the storage in artificial saliva with its fluid absorption caused a decrease in these parameters due to the plasticizing effect of water [19].

In a study comparing the mechanical properties of four clear aligner materials (Taglus, Essix, Zendura, and Zendura FLX), Taglus displayed a higher elastic modulus and ultimate strength than Essix, which is also a PET-G polymer, just like Taglus. Taglus was the stiffest of the four materials, being even stiffer (8%) than Essix [21]. An *in vitro* study using an orthodontic simulator and measuring the buccolingual force and moments of a 0.75 mm thick thermoformed Taglus aligner for three maxillary teeth (central incisor, canine, and second premolar) showed a significantly higher mean buccal force and mean moment with a tendency to tip a tooth crown buccally in canine teeth [22]. In comparison, the elastic strain values of the Taglus system were significantly higher than those of the CA Pro+ system. Previous research has also indicated that the materials used in the Taglus aligners' composition have notable elastic properties [23]. Another study that followed the characterization by DIC confirmed that materials with higher elastic deformation respond better to compression, consistent with our results obtained for the Taglus system [17].

The PONTOS ARAMIS system is a powerful tool that significantly enhances our understanding of aligner deformation behavior. By providing precise, real-time data, it enables the development of better materials, optimized aligner designs, and personalized treatment plans. The integration of PONTOS ARAMIS with advanced computational methods like FEA further amplifies its impact, paving the way for continuous innovation in orthodontic treatment [14,24].

As research and technology continue to evolve, the insights gained from PONTOS ARAMIS analyses will undoubtedly lead to even more effective, durable, and comfortable aligners. This progress will ensure that clear aligners remain at the forefront of orthodontic treatment, offering patients a superior alternative to traditional methods [14,24].

The largest displacement on the Y axis is caused by the function of the articulator and the shape of the aligners. A first indication of the rigidity of the aligners can be seen as a difference between the three types of aligners, thus Spark has the largest displacement, followed by Taglus and Scheu.

The use of the DIC technique in this study provides a solid framework for analyzing the deformation behavior of aligner systems [17,25]. The ability of the technique to capture highly detailed strain and displacement fields provides significant insight into the mechanical properties of the alignment materials. However, it is essential to consider that different investigations may use different methodologies which may influence the results [14].

In our study, the highest values of rigid displacement in both the maxillary and mandibular arches for each of the three axes was recorded by the SP group, in which the specimens were fabricated using the Spark Trugen system. Within each studied axis, the Spark Trugen system showed significantly higher values compared to the other two tested aligner systems. Within axis Z, both maxillary and mandibular, the Taglus Premium system showed significantly higher values compared to the Scheu CA[®] Pro+ Clear Aligner system.

In terms of elastic deformation, in the maxillary arch, the Scheu system showed lower values in the X-coordinate compared to the other two systems tested. In the mandibular arch, both the Taglus and Spark systems showed higher values at the Z-coordinate compared to the Scheu system. The results of these experiments reproduce the actual operating conditions of the aligners that have a direct clinical significance in the biomedical field. The current study found that the Spark system exhibited the most considerable rigid displacement. This observation is consistent with previous findings that reported significant deformation of PET-G-based aligners under mechanical stress. For instance, a study performed by Casavola revealed a full-field mechanical deformation behavior of PET-G-based aligners including the Spark system [17]. The study demonstrated that PET-G aligners undergo significant deformation when subjected to mechanical loads, which supports our findings. The CA Pro+ Clear Aligner system demonstrated lower values of elastic deformation compared to the Spark and Taglus systems. This finding is supported by studies that have shown that certain alignment materials are designed to provide more stability and less deformation under stress [26,27]. A study that highlighted the image correlation to measure shape and deformation emphasized that different materials used in the composition of aligners react different to mechanical loads, which is consistent with our findings for the CA Pro+ system [26].

According to the literature, the polymer composition and the manufacturing process are responsible for the deformation and relaxation behavior of materials used for aligners [18,22]. For example, a previous study showed that polymers with a higher modulus of elasticity exhibit a lower elastic deformation, which confirms the findings of this study in which the aligner system made of copolyester and thermoplastic elastomer showed the lowest elastic deformation values [9,24]. In addition, the increased deformation resistance in the mandibular area of all the three systems is consistent with previous research highlighting the variability of deformation behavior depending on the dental arch thus suggesting the need for customized approaches in orthodontic treatments [27].

Based on the study findings, the clear aligner system based on copolyester and thermoplastic elastomer emerged as the most suitable and user-friendly option, particularly due to its superior resistance to elastic deformation and rigid displacement in compression tests. This is in line with other consistent findings in the literature, in which aligners with higher stability and lower deformation are often preferred for consistent orthodontic results [24,28]. Given its demonstrated stability, the clear aligner system based on copolyester and thermoplastic elastomer should be further recommended to patients seeking reliable and durable aligner solutions that guarantee effective and predictable treatment outcomes.

Given these results, it is admitted that the null hypothesis of the study has been rejected. However, future studies are needed to replicate, as closely as possible, the oral environment through the presence of saliva, masticatory movements, or changes in temperature or pH [29,30]. The research activity should also focus on standardizing the test protocols for

the DIC analysis of alignment materials to ensure comparability of results across different studies. In addition, exploring the long-term effects of repeated mechanical loading on the deformation behavior of aligners may provide additional insights into their durability and performance in clinical contexts [31,32].

In conclusion, the findings of the present study, which indicate significant differences in the deformation behavior among the three alignment systems, are consistent with those reported by other researchers using the DIC technique as an evaluation method. The substantial rigid displacement of the Spark system as well as the higher elastic deformation values of the Spark and Taglus systems align with the findings of previous studies. These results emphasize the importance of considering the material properties and mechanical behavior in the design and selection of transparent alignment systems for orthodontic treatment.

5. Conclusions

- In conclusion, the Spark Trugen clear aligner system demonstrated a lower stability to rigid displacement and elastic deformation under compression testing compared to the Scheu CA[®] Pro+ Clear Aligner and Taglus Premium systems.
- All three tested clear aligner systems showed an increased resistance to elastic displacement and rigid deformation in the mandibular arch.
- The Scheu CA[®] Pro+ Clear Aligner system showed the lowest elastic deformation values after compression testing.

Author Contributions: Conceptualization, N.D.O., D.F.C. and N.S.; methodology, T.P.; software, A.C. and D.F.C.; validation, D.F.C., N.D.O. and I.N.Z.; formal analysis, S.N.R.; investigation, N.D.O. and D.F.C.; resources, N.D.O. and I.N.Z.; data curation, D.F.C.; writing—original draft preparation, N.D.O. and D.F.C.; writing—review and editing, I.N.Z. and C.S.; visualization, S.N.R.; supervision, I.N.Z. and N.S.; project administration, N.D.O.; funding acquisition, N.D.O. All authors have read and agreed to the published version of the manuscript.

Funding: This research received no external funding.

Institutional Review Board Statement: The study was conducted in accordance with the Declaration of Helsinki and approved by the Ethics Committee of “Grigore T. Popa” University of Medicine and Pharmacy of Iași (approval no. 56, approval date 12 March 2021).

Informed Consent Statement: Informed consent was obtained from all subjects involved in the study.

Data Availability Statement: The original contributions presented in the study are included in the article, further inquiries can be directed to the corresponding authors.

Conflicts of Interest: The authors declare no conflicts of interest.

References

1. Bichu, Y.M.; Alwafi, A.; Liu, X.; Andrews, J.; Ludwig, B.; Bichu, A.Y.; Zou, B. Advances in orthodontic clear aligner materials. *Bioact. Mater.* **2023**, *22*, 384–403. [\[CrossRef\]](#) [\[PubMed\]](#)
2. Hennessy, J.; Al-Awadhi, E.A. Clear aligners generations and orthodontic tooth movement. *J. Orthod.* **2016**, *43*, 68–76. [\[CrossRef\]](#) [\[PubMed\]](#)
3. Albertini, P.; Mazzanti, V.; Mollica, F.; Pellitteri, F.; Palone, M.; Lombardo, L. Stress Relaxation Properties of Five Orthodontic Aligner Materials: A 14-Day In-Vitro Study. *Bioengineering* **2022**, *9*, 349. [\[CrossRef\]](#) [\[PubMed\]](#)
4. Lee, S.Y.; Kim, H.; Kim, H.J.; Chung, C.J.; Choi, Y.J.; Kim, S.J.; Cha, J.Y. Thermo-mechanical properties of 3D printed photocurable shape memory resin for clear aligners. *Sci. Rep.* **2022**, *12*, 6246. [\[CrossRef\]](#)
5. Voudouris, J.C.; Voudouris, J.D.; Nicolay, O.; Glaser, B.; Nicozisis, J.; Theodoridis, G.; Carrillo, R.; Moshiri, M.; Masoud, M. Clear aligners, dentofacial orthopedics, physics and supercorrection prescription biomechanics. A meeting of the minds. *Semin. Orthod.* **2022**, *27*, 202–258. [\[CrossRef\]](#)
6. Bucci, R.; Rongo, R.; Levatè, C.; Michelotti, A.; Barone, S.; Razionale, A.V.; D’Antò, V. Thickness of orthodontic clear aligners after thermoforming and after 10 days of intraoral exposure: A prospective clinical study. *Prog. Orthod.* **2019**, *20*, 36. [\[CrossRef\]](#)
7. Zinelis, S.; Panayi, N.; Polychronis, G.; Papageorgiou, S.N.; Eliades, T. Comparative analysis of mechanical properties of orthodontic aligners produced by different contemporary 3D printers. *Orthod. Craniofac Res.* **2022**, *25*, 336–341. [\[CrossRef\]](#)

8. Jindal, P.; Juneja, M.; Siena, F.L.; Bajaj, D.; Breedon, P. Mechanical and geometric properties of thermoformed and 3D printed clear dental aligners. *Am. J. Orthod. Dentofacial Orthop.* **2019**, *156*, 694–701. [\[CrossRef\]](#)
9. Shirey, N.; Mendonca, G.; Groth, C.; Kim-Berman, H. Comparison of mechanical properties of 3-dimensional printed and thermoformed orthodontic aligners. *Am. J. Orthod. Dentofacial Orthop.* **2023**, *163*, 720–728. [\[CrossRef\]](#)
10. Mao, B.; Tian, Y.; Li, J.; Zhou, Y. Expansion rebound deformation of clear aligners and its biomechanical influence: A three-dimensional morphologic analysis and finite element analysis study. *Angle Orthod.* **2023**, *93*, 572–579. [\[CrossRef\]](#)
11. Zhang, Y.; Jin, X.; Savoldi, F.; Han, J.; Su, R.K.L.; Fok, A.; Chen, J.; Tsoi, J.K. Validation of a double-semicircular notched configuration for mechanical testing of orthodontic thermoplastic aligner materials. *J. Mech. Behav. Biomed. Mater.* **2024**, *155*, 106543. [\[CrossRef\]](#) [\[PubMed\]](#)
12. Can, E.; Panayi, N.; Polychronis, G.; Papageorgiou, S.N.; Zinelis, S.; Eliades, G.; Eliades, T. In-house 3D-printed aligners: Effect of in vivo ageing on mechanical properties. *Eur. J. Orthod.* **2022**, *44*, 51–55. [\[CrossRef\]](#) [\[PubMed\]](#)
13. Jindal, P.; Worcester, F.; Siena, F.L.; Forbes, C.; Juneja, M.; Breedon, P. Mechanical behaviour of 3D printed vs thermoformed clear dental aligner materials under non-linear compressive loading using FEM. *J. Mech. Behav. Biomed. Mater.* **2020**, *112*, 104045. [\[CrossRef\]](#) [\[PubMed\]](#)
14. Casavola, C.; Pappalettera, G.; Pappalettere, C.; Patronelli, M.; Renna, G.; Laurenziello, M.; Ciavarella, D. A full-field DIC analysis of the mechanical-deformation behavior of polyethylene terephthalate glycol (PET-G) aligners. *J. Mech. Behav. Biomed. Mater.* **2022**, *134*, 105391. [\[CrossRef\]](#)
15. Schreier, H.; Orteu, J.J.; Sutton, M.A.; Michael, A.M.A.; Orteu, J.J.; Schreier, H.W. Single Camera Models and Calibration Procedures in Computer Vision. In *Image Correlation for Shape, Motion and Deformation Measurements*; Michael, A., Sutton, M.A., Orteu, J.J., Schreier, H.W., Eds.; Springer: New York, NY, USA, 2009; pp. 1–37.
16. Kibitkin, V.; Savchenko, N.; Grigoriev, M.; Solodushkin, A.; Burlachenko, A.; Buyakov, A.; Zykova, A.; Rubtsov, V.; Tarasov, S. Digital Image Correlation Characterization of Deformation Behavior and Cracking of Porous Segmented Alumina under Uniaxial Compression. *Ceramics* **2023**, *6*, 102–131. [\[CrossRef\]](#)
17. Casavola, C.; Pappalettera, G.; Pappalettere, C.; Patronelli, M.; Renna, G.; Ciavarella, D.; Laurenziello, M. DIC analysis of mechanical response of tooth aligners under simulated swallowing acts. *IOP Conf. Ser. Mater. Sci. Eng.* **2023**, *1275*, 012023. [\[CrossRef\]](#)
18. Lümkmann, N.; Klimenta, M.; Hoffmann, M.; Meinen, J.; Stawarczyk, B. Dimensional Stability and Reproducibility of Varying FFF Models for Aligners in Comparison to Plaster Models. *Materials* **2023**, *16*, 4835. [\[CrossRef\]](#)
19. Tamburrino, F.; D'Antò, V.; Bucci, R.; Alessandri-Bonetti, G.; Barone, S.; Rationale, A.V. Mechanical properties of thermoplastic polymers for aligner manufacturing: In vitro study. *Dent. J.* **2020**, *8*, 47. [\[CrossRef\]](#)
20. Hertan, E.; McCray, J.; Bankhead, B.; Kim, K.B. Force profile assessment of direct-printed aligners versus thermoformed aligners and the effects of non-engaged surface patterns. *Prog. Orthod.* **2022**, *23*, 49. [\[CrossRef\]](#)
21. Keller, K.J.; Keller, K.J.; Giannini, P.J.; Gregory, M.S.; Oakley, G. Stress Relaxation in Orthodontic Aligner Plastics; An In Vitro Stress Relaxation in Orthodontic Aligner Plastics; An In Vitro Comparison Study Comparison Study Stress Relaxation In Orthodontic Aligner Plastics; An In Vitro Comparison Study [Internet]. 2020. Available online: <https://digitalcommons.unmc.edu/etd> (accessed on 5 June 2024).
22. Kaur, H.; Truong, J.; Heo, G.; Mah, J.K.; Major, P.W.; Romanyk, D.L. An in vitro evaluation of orthodontic aligner biomechanics around the maxillary arch. *Am. J. Orthod. Dentofacial Orthop.* **2021**, *160*, 401–409. [\[CrossRef\]](#)
23. Sawamura, M.; Nakano, H.; Shiogama, M.; Takano, N.; Maki, K. Using digital image correlation to measure displacement and strain during involving distal movement of anterior teeth with clear aligner. *Dent. Mater. J.* **2023**, *42*, 493–500. [\[CrossRef\]](#) [\[PubMed\]](#)
24. Grünheid, T.; Bitner, T.F. Wear and fatigue resistance: An in-vitro comparison of three polyethylene terephthalate glycol and thermoplastic polyurethane materials for vacuum-formed retainers. *Int. Orthod.* **2023**, *21*, 100748. [\[CrossRef\]](#) [\[PubMed\]](#)
25. Milovanović, A.; Sedmak, A.; Golubović, Z.; Mihajlović, K.Z.; Žurkić, A.; Trajković, I.; Milošević, M. The effect of time on mechanical properties of biocompatible photopolymer resins used for fabrication of clear dental aligners. *J. Mech. Behav. Biomed. Mater.* **2021**, *119*, 104494. [\[CrossRef\]](#) [\[PubMed\]](#)
26. Lyu, X.; Cao, X.; Yan, J.; Zeng, R.; Tan, J. Biomechanical effects of clear aligners with different thicknesses and gingival-margin morphology for appliance design optimization. *Am. J. Orthod. Dentofacial Orthop.* **2023**, *164*, 239–252. [\[CrossRef\]](#)
27. Nowak, C.M.; Othman, A.; Ströbele, D.A.; von See, C. Comparative mechanical testing for different orthodontic aligner materials over time—In vitro study. *J. Clin. Exp. Dent.* **2022**, *14*, e457–e463. [\[CrossRef\]](#)
28. Dalaie, K.; Fatemi, S.M.; Ghaffari, S. Dynamic mechanical and thermal properties of clear aligners after thermoforming and aging. *Prog. Orthod.* **2021**, *22*, 15. [\[CrossRef\]](#)
29. Golkhani, B.; Weber, A.; Keilig, L.; Reimann, S.; Bourauel, C. Variation of the modulus of elasticity of aligner foil sheet materials due to thermoforming. *J. Orofac. Orthop.* **2022**, *83*, 233–243. [\[CrossRef\]](#)
30. Morris, R.S.; Hoyer, L.N.; Elnagar, M.H.; Atsawasuwan, P.; Galang-Boquiren, M.T.; Caplin, J.; Viana, G.C.; Obrez, A.; Kusnoto, B. Accuracy of Dental Monitoring 3D digital dental models using photograph and video mode. *Am. J. Orthod. Dentofac. Orthop.* **2019**, *156*, 420–428. [\[CrossRef\]](#)

31. Ryu, J.H.; Kwon, J.S.; Jiang, H.B.; Cha, J.Y.; Kim, K.M. Effects of thermoforming on the physical and mechanical properties of thermoplastic materials for transparent orthodontic aligners. *Korean J. Orthod.* **2018**, *48*, 316–325. [[CrossRef](#)]
32. Dođramacı, E.J.; Chubb, D.W.R.; Rossi-Fedele, G. Orthodontic thermoformed retainers: A two-arm laboratory study into post-fabrication outcomes. *Aust. Dent. J.* **2018**, *63*, 347–355. [[CrossRef](#)]

Disclaimer/Publisher’s Note: The statements, opinions and data contained in all publications are solely those of the individual author(s) and contributor(s) and not of MDPI and/or the editor(s). MDPI and/or the editor(s) disclaim responsibility for any injury to people or property resulting from any ideas, methods, instructions or products referred to in the content.